

# A Study of WW Scattering at the LHC

Farahnaaz Nauyock

March 2004



THE UNIVERSITY  
*of* MANCHESTER

Particle Physics Group  
Department of Physics and Astronomy

A thesis submitted to The University of Manchester for the degree of  
Doctor of Philosophy in the Faculty of Science and Engineering



# Contents

<b>Abstract</b>	<b>11</b>
<b>Declaration</b>	<b>12</b>
<b>The Author</b>	<b>13</b>
<b>Acknowledgements</b>	<b>14</b>
<b>1 Introduction</b>	<b>16</b>
1.1 The Fundamental Particles . . . . .	16
1.1.1 The Fermions . . . . .	17
1.2 Gauge Bosons . . . . .	19
1.3 The Higgs Mechanism . . . . .	21
1.4 Electroweak Symmetry Breaking . . . . .	22
<b>2 The LHC and the ATLAS Detector</b>	<b>24</b>
2.1 Terms Used . . . . .	24
2.2 The Large Hadron Collider . . . . .	24
2.3 Motivation behind the ATLAS Detector . . . . .	29
2.3.1 Higgs searches . . . . .	30
2.3.2 SUSY searches . . . . .	31
2.3.3 Top physics . . . . .	31
2.3.4 B-physics . . . . .	31

2.3.5	Other searches . . . . .	33
2.4	Detector design constraints . . . . .	33
2.5	The ATLAS Detector . . . . .	35
2.5.1	Overall detector concept . . . . .	35
2.5.2	The inner detector . . . . .	38
2.5.3	Calorimetry . . . . .	46
2.5.4	The muon spectrometer . . . . .	50
2.5.5	Trigger, data acquisition and computing . . . . .	57
<b>3</b>	<b>Simulation and Reconstruction</b>	<b>60</b>
3.1	ATLAS Offline Software . . . . .	60
3.1.1	Athena and GAUDI . . . . .	61
3.1.2	ATLAS offline computing . . . . .	63
3.2	Monte Carlo Generators . . . . .	64
3.2.1	Pythia and PythiaModule . . . . .	65
3.3	ATLFAST: A Fast Simulation Package for ATLAS . . . . .	65
3.3.1	Athena-Atlfast overview . . . . .	66
3.3.2	Organisation of Athena-Atlfast package . . . . .	67
3.3.3	Calorimetric clusters . . . . .	69
3.3.4	Isolated particles . . . . .	71
3.3.5	Jet reconstruction . . . . .	72
3.3.6	Missing transverse energy . . . . .	73
3.3.7	Other Athena Algorithms . . . . .	74
3.3.8	$K_T$ algorithm . . . . .	75
3.4	Analysis Parameters . . . . .	76
<b>4</b>	<b>WW Scattering Studies</b>	<b>79</b>
4.1	Framework . . . . .	80
4.2	Lagrangian . . . . .	81
4.3	Unitarisation Procedure . . . . .	82

4.4	Parton-Level Cross-Sections . . . . .	85
4.5	Signal and Background Processes . . . . .	89
4.6	The Signal . . . . .	92
4.6.1	Leptonic W . . . . .	92
4.6.2	Hadronic W . . . . .	94
4.6.3	Other important cuts . . . . .	98
<b>5</b>	<b>Discussion</b>	<b>101</b>
5.1	Reconstructed $WW$ Mass . . . . .	101
5.2	Comparison of Results with Cone Algorithm . . . . .	110
5.3	Effect of Smearing . . . . .	114
5.4	Resolution as compared to the Technical Design Report [6] . . . . .	114
5.5	R-parameter, Cone Radius and Cell Energy Threshold Study . . . . .	120
5.5.1	R-parameter study . . . . .	120
5.5.2	Cone radius study . . . . .	121
5.5.3	Note on $k_T R_{par}$ . . . . .	126
<b>6</b>	<b>Summary and Future Work</b>	<b>130</b>
	<b>Appendix A</b>	<b>132</b>
	<b>Appendix B</b>	<b>133</b>

# List of Figures

2.1	The LHC injector complex. Taken from [16]. . . . .	27
2.2	The layout of the LHC. Taken from [17]. . . . .	29
2.3	The ATLAS detector. Taken from [6]. . . . .	38
2.4	Section through the ATLAS detector. Taken from [16]. . . . .	39
2.5	The inner detector. Taken from [16]. . . . .	40
2.6	View of the ATLAS calorimeter. Taken from [6]. . . . .	47
2.7	Side view of one quadrant of the muon spectrometer. Taken from [16]. . . . .	52
2.8	Transverse view of muon spectrometer. Taken from [16]. . . . .	53
2.9	Trigger and DAQ system. Taken from [24]. . . . .	58
3.1	The Athena-GAUDI framework. Take from [26]. . . . .	63
3.2	The Atlfast Algorithm execution sequence. Taken from [33]. . . . .	69
4.1	Parameter space map as determined from IAM. Taken from [7]. . . . .	85
4.2	Partonic cross-section for scenario A. . . . .	86
4.3	Partonic cross-section for scenario B. . . . .	87
4.4	Partonic cross-section for scenario C. . . . .	87
4.5	Partonic cross-section for scenario D. . . . .	88
4.6	Partonic cross-section for scenario E. . . . .	88
4.7	Feynman diagrams for signal and backgrounds: (a) signal; (b) $W$ +jets; One of the $W$ s (not shown in Figure 4.7(b)) comes from the quark which fakes a $W$ by becoming a jet or jets; (c) $t\bar{t}$ . . . . .	90

4.8	Leptonic variables: (a) transverse momentum of leptons with highest $p_T$ in an event, (b) pseudorapidity of the lepton, (c) missing transverse momentum and (d) $p_T$ of the leptonic $W$ candidate. . . . .	96
4.9	Variables for hadronic $W$ . (a) $p_T$ , (b) pseudorapidity, (c) invariant mass and (d) $p_T\sqrt{y_{cut}}$ . . . . .	97
4.10	(a) Mass distribution of leptonic $W$ and jet other than the hadronic $W$ candidate, (b) pseudorapidity of tag jets, (c) $p_T$ for $WW +$ tag jets system and (d) number of minijets. . . . .	100
5.1	Reconstructed $WW$ mass for signal and background separately. A: 1 TeV scalar, B: 1.4 TeV Vector, C: 1.9 TeV Vector, D: Double Resonance and E: Continuum. . . . .	102
5.2	$ \cos\theta $ for signal and background separately. A: 1 TeV scalar, B: 1.4 TeV Vector, C: 1.9 TeV Vector, D: Double Resonance and E: Continuum. . . .	103
5.3	Reconstructed $WW$ mass using the cone algorithm. A: 1 TeV scalar, B: 1.4 TeV Vector, C: 1.9 TeV Vector, D: Double Resonance and E: Continuum. . .	111
5.4	Effect of smearing using $k_T$ algorithm for the scalar 1 TeV sample (scenario A). (a) shows the unsmeared and smeared $WW$ mass, (b) shows the difference in the number of events between the unsmeared and smeared $WW$ mass. . . . .	116
5.5	Effect of smearing using cone algorithm for the scalar 1 TeV sample (scenario A). (a) shows the unsmeared and smeared $WW$ mass, (b) shows the difference in the number of events between the unsmeared and smeared $WW$ mass. . . . .	117
5.6	Resolution obtained using the $k_T$ algorithm. This is the expected resolution after a year of high luminosity run at the LHC, with pile-up included. (a) shows resolution for smeared hadronic $W$ mass, (b) shows resolution for unsmeared hadronic $W$ mass. . . . .	118

5.7	Resolution on $W$ mass at low luminosity (left) and high luminosity with pile-up included (right) found in the Technical Design Report. The events have undergone detector simulation in both cases. Taken from [6]. . . . .	119
5.8	Reconstructed hadronic $W$ mass for different $R_{par}$ using $k_T$ algorithm and an energy threshold $E_m = 1.0$ GeV. Each continuum sample (scenario E) for the different $R_{par}$ contains 300,000 events. (a) shows $R_{par}$ 0.4 to 0.7 while (b) shows $R_{par}$ 0.7 to 1.0. . . . .	123
5.9	$R_{par}$ with varying $E_m$ using $k_T$ algorithm for continuum sample (scenario E). A sample of 300,000 events are generated for each $(R_{par}, E_m)$ . . .	124
5.10	$W$ mass for a fixed $R_{par}$ of 1.0 and varying energy thresholds $E_m$ using the $k_T$ algorithm. A sample of 300,000 events are generated for each $E_m$ and the continuum sample (scenario E) is used for this plot. . . . .	125
5.11	Reconstructed hadronic $W$ mass for various energy thresholds $E_m$ . Continuum sample (scenario E) containing 150,000 events are used for various $E_m$ and $R_{par}$ or $\Delta R$ . (a) shows the hadronic $W$ mass for a cone radius of 0.4 and 0.7, (b) shows the hadronic $W$ mass for the $k_T$ $R_{par}$ of 0.7 and 1.0. . . . .	126
5.12	Variation of root mean square value of the hadronic $W$ mass peak with cone radius for different energy thresholds. The peak was fitted using a Gaussian. Continuum sample (scenario E) containing 150,000 events are used for each $(E_m, \text{cone radius } \Delta R)$ . . . . .	127
5.13	Ratio of number of events for low mass peak (5-40 GeV) to that of high mass peak taken between 70 and 90 GeV. Continuum sample (scenario E) containing 150,000 events are used for each $(E_m, \text{cone radius } \Delta R)$ . . . .	128
5.14	Number of hadronic $W$ events between 70 and 90 GeV. Each continuum sample (scenario E) with various cone radii contained 150,000 events. . .	129

# List of Tables

1.1	Fundamental leptons in the Standard Model [3]. . . . .	18
1.2	Properties of quarks. Note that the mass of the top quark given is that obtained from direct observation of top events [3]. . . . .	19
1.3	The vector bosons [3]. . . . .	21
2.1	The design parameters at the LHC for p-p collision [14]. . . . .	26
2.2	Parameters of the inner detector [6]. . . . .	42
2.3	The muon chamber instrumentation. “Area covered” refers to chamber modules which are normally made of several detectors. . . . .	56
3.1	Atlfast parameters. . . . .	78
4.1	Parameters for the 5 different scenarios. . . . .	86
4.2	Cross-sections for signal and backgrounds used to generate events in Pythia. For the background, the cross-sections are in the restricted kinematic range given on p.90. . . . .	91
4.3	Number of events generated for signal and backgrounds. . . . .	93
5.1	Effect of leptonic and hadronic cuts on the number of events for the signal and background for an integrated luminosity of $100 \text{ fb}^{-1}$ . A: 1 TeV scalar, B: 1.4 TeV Vector, C: 1.9 TeV Vector, D: Double Resonance and E: Continuum. S/B denotes the signal to background ratio. . . . .	105



5.2	Effect of environment cuts on the number of events for the signal and background for an integrated luminosity of $100 \text{ fb}^{-1}$ . A: 1 TeV scalar, B: 1.4 TeV Vector, C: 1.9 TeV Vector, D: Double Resonance and E: Continuum. S/B denotes the signal to background ratio. . . . .	106
5.3	Number of events produced for an integrated luminosity of $100 \text{ fb}^{-1}$ and the cumulative efficiencies (in %) of various cuts for the five different signal scenarios and for the $t\bar{t}$ and $W$ +jets backgrounds. A: 1 TeV scalar, B: 1.4 TeV Vector, C: 1.9 TeV Vector, D: Double Resonance and E: Continuum.	107
5.4	The effect of leptonic and hadronic cuts on the signal and background samples for an integrated luminosity of $100 \text{ fb}^{-1}$ . A: 1 TeV scalar, B: 1.4 TeV Vector, C: 1.9 TeV Vector, D: Double Resonance and E: Continuum. S/B denotes the signal to background ratio. Taken from Reference [7]. . .	108
5.5	The effect of environment cuts on the signal and background samples for an integrated luminosity of $100 \text{ fb}^{-1}$ . A: 1 TeV scalar, B: 1.4 TeV Vector, C: 1.9 TeV Vector, D: Double Resonance and E: Continuum. S/B denotes the signal to background ratio. Taken from Reference [7]. . . . .	109
5.6	Events generated using the cone algorithm. The background is generated using the restricted kinematic range given on p.90. In order to get the real number of events for an integrated luminosity of $100 \text{ fb}^{-1}$ , a scaling must be done as in Table 5.7. . . . .	110
5.7	Effect of leptonic and hadronic cuts on the number of events for signal and background for the cone algorithm analysis. An integrated luminosity of $100 \text{ fb}^{-1}$ is used. A: 1 TeV scalar, B: 1.4 TeV Vector, C: 1.9 TeV Vector, D: Double Resonance and E: Continuum. S/B denotes the signal to background ratio. . . . .	112

5.8	Effect of environment cuts on the number of events for the signal and background. An integrated luminosity of $100 \text{ fb}^{-1}$ is used for the cone algorithm analysis. A: 1 TeV scalar, B: 1.4 TeV Vector, C: 1.9 TeV Vector, D: Double Resonance and E: Continuum. S/B denotes the signal to background ratio. . . . .	113
B-1	Number of events ( $N$ ) left after passing all cuts. . . . .	135

# Abstract

This thesis presents a study of  $WW$  scattering at the LHC, a proton-proton collider being built at CERN and due to start its first run in 2007. The case where no new particles are discovered before the start of the LHC is analysed. The elastic scattering of  $WW$  is considered and the semileptonic<sup>1</sup> decay channels of the  $W$  bosons are investigated. Signals and backgrounds are simulated using Atlfast, a fast simulation programme for the ATLAS experiment.

This specific channel causes violation of unitarity at 1.2 TeV. Therefore, unitarisation is performed and this leads to different resonance scenarios, five of which are investigated. The final signal to background ratio after applying various kinematic cuts on events is greater than one for all the five scenarios.

A comparison between the  $k_T$  algorithm and cone algorithm is also performed to find out which jet-finding analysis yields a better signal to background ratio. The  $k_T$  algorithm proves very efficient in reducing the background by an approximate factor of 1.5 better than the cone algorithm for various scenarios. A preliminary study is done to find the effects of both the cone radius of the cone algorithm and the R-parameter of the  $k_T$  analysis on the width of the hadronic  $W$  mass spectrum. A value of 0.7 for the cone radius is found to be the optimum, while the corresponding R-parameter of 1.0 is used.

The analysis shows that ATLAS will be able to observe scalar and vector resonances of up to 1.4 TeV after a year of high luminosity run of  $100 \text{ fb}^{-1}$  at the LHC.

---

<sup>1</sup>“Semileptonic” is defined here and throughout as the situation when the two final state  $W$ s decay differently. One of them decays leptonically ( $W \rightarrow l\nu$ ) and the other one decays hadronically ( $W \rightarrow jj$ ).

# Declaration

No portion of the work referred to in this thesis has been submitted in support of an application for another degree or qualification of this or any other university or other institute of learning.

Copyright in text of this thesis rests with the Author. Copies (by any process) either in full, or of extracts, may be made only in accordance with instruction given by the Author and lodged in the John Rylands University Library of Manchester. Details may be obtained from the Librarian. This page must form part of any such copies made. Further copies (by any process) of copies made in accordance with such instructions may not be made without the permission (in writing) of the Author.

The ownership of any intellectual property rights which may be described in this thesis is vested in the University of Manchester, subject to any prior agreement to the contrary, and may not be made available for use by third parties without the written permission of the University, which will prescribe the terms and conditions of any such agreement.

Further information on the conditions under which disclosures and exploitation may take place is available from the Head of the Department of Physics and Astronomy.

## The Author

The author was educated at Loreto Convent Port Louis College, Mauritius, between 1990 and 1996, before obtaining a first class B.Sc. (Hons) degree in Physics at The University of Mauritius in 2000. The work presented in this thesis was undertaken at The University of Manchester.

# Acknowledgements

I would like to start by thanking my supervisor, Fred Loebinger, for all his help, support and encouragement throughout the duration of this Ph.D. I am hugely indebted to him for all his patience and understanding. I would also like to thank Brian Cox with whom I worked very closely at Manchester and without whose guidance, this work would not have been possible.

My thanks also go to Jon Couchman of University College London, with whom I worked and who generated most of the millions of events used in this thesis. Thanks also to Sarah Allwood, Jeff Forshaw and Andres Osario for the interesting physics discussions related to my work.

This work would not have been possible without the support and funding provided by the Manchester HEP group. Thanks for also funding those trips to CERN.

It would not have been possible for me to reach where I am today if my dad had not encouraged my interest in science from an early age. I can still remember all those science books he would buy me whenever he saw one that was interesting. I can never pay him back for all this. I would also like to thank my mum and brother for being very supportive throughout my life. It has been hard being so far away from home for all those years. Thanks for letting me pursue what I wanted.

Finally, I would like to thank Si for all his help in C++ programming and for always being there whenever I needed someone to talk to. Thanks a lot for all those wonderful moments.

**To my father.**

# Chapter 1

## Introduction

The Standard Model (SM) is the most widely tested and accepted theory of an accurate description of fundamental particles and their interactions [1]. In fact high-precision experiments to date have probed distances down to  $10^{-18}$ m to confirm many of the Standard Model predictions. However there are still many questions that remain unanswered.

One of the main objectives of particle physics is to test the Standard Model, by studying how well true data match with theories. Furthermore, physicists are aware that the Standard Model is not the end. There are ways of searching for new physics beyond the Standard Model, that will provide us with a “Theory of Everything”.

In this chapter a brief discussion of the Standard Model is given so as to have an overview of what is being tested.

### 1.1 The Fundamental Particles

The Standard Model is made up of two distinct groups: *fermions* (matter particles) and *gauge bosons* (which mediate interactions between the matter particles). What makes the two groups of particles different from each other is their intrinsic



angular momentum. The fermions, which can be divided into two groups (leptons and quarks), are half-integer spin particles while the bosons are integer spin ones. The Standard Model treats these fundamental particles (leptons, quarks and bosons) as being particles without any internal structure or excited states, i.e., they are assumed to be elementary [2].

### 1.1.1 The Fermions

As mentioned earlier, the fermions can be further divided into two groups, namely the *leptons* and the *quarks*. For reasons still unknown to us, both groups are made up of six particles and six antiparticles which are separated into three generations. The antiparticle has the same spin and mass to its corresponding particle but an opposite charge. This result follows from the combination of special relativity with quantum mechanics.

#### Leptons

The first generation of lepton is the electron ( $e^-$ ) and the electron-neutrino ( $\nu_e$ ). The next generation, called the second generation, is made up of the muon ( $\mu$ ) and the muon-neutrino ( $\nu_\mu$ ). Finally, the third generation consists of the tau ( $\tau$ ) and the tau-neutrino ( $\nu_\tau$ ). The mass of the leptons increases with generation, the electron being the lightest ( $\sim 0.51$  MeV) and tauon being the heaviest ( $\sim 1777$  MeV) as shown in Table 1.1. The electron, muon and tauon all have a charge of  $-1.9 \times 10^{-19}$  C, often denoted in terms of the positron charge,  $e$ . The neutrinos are neutral leptons. The charged leptons interact via both electromagnetic and weak forces whereas the neutrinos are only sensitive to the weak force.

Due to their half-integral spins, fermions can exist as either right-handed or left-handed particles. However, this is not the case for neutrinos. They can only exist in left-handed states while all antineutrinos can only exist in right-handed

Table 1.1: Fundamental leptons in the Standard Model [3].

Flavour	Charge ( $\times e$ )	Mass (MeV)	Mean life (s)
$\nu_e$	0	$<3 \times 10^{-6}$	stable
$\nu_\mu$	0	$<0.19$	stable
$\nu_\tau$	0	$<18.2$	stable
$e^-$	-1	0.511	stable
$\mu^-$	-1	105.7	$2.197 \times 10^{-6}$
$\tau^-$	-1	1777	$2.910 \times 10^{-13}$

states. This arises because neutrinos are thought to be massless in the Standard Model. However the Super-Kamiokande experiment suggests strong evidence that neutrinos may not be massless particles [4] after all. So they must then exist in both right-handed and left-handed states.

### Quarks

Six quarks are presently known to exist. Just like leptons, quarks exist in six distinct types, or *flavours*. They occur in pairs denoted as

$$\begin{pmatrix} u \\ d \end{pmatrix}, \quad \begin{pmatrix} c \\ s \end{pmatrix}, \quad \begin{pmatrix} t \\ b \end{pmatrix}$$

The mass of the quarks increases with generation. Table 1.2 shows the masses and other properties of the quarks. These quarks also have an antiparticle of the same mass and spin. Each generation is made up of a quark with a fractional charge of  $\frac{2}{3}e$  and another one with a charge of  $-\frac{1}{3}e$ . No free quark has ever

Table 1.2: Properties of quarks. Note that the mass of the top quark given is that obtained from direct observation of top events [3].

Flavour	Charge $\times e$	Approximate mass (MeV)	Colour charge
d	-1/3	3	<i>r,g,b</i>
u	+2/3	7	<i>r,g,b</i>
s	-1/3	120	<i>r,g,b</i>
c	+2/3	1,200	<i>r,g,b</i>
b	-1/3	4,200	<i>r,g,b</i>
t	+2/3	174,000	<i>r,g,b</i>

been observed despite many experiments to find them. They are confined within bound states called *hadrons*. Only three types of quark bound states are allowed:

- mesons ( $q\bar{q}$ )
- baryons ( $qqq$ )
- antibaryons ( $\bar{q}\bar{q}\bar{q}$ )

The main reason for the existence of quarks in bound states is a degree of freedom called *colour*. Quarks may take one of the three colour charges, namely *red*, *blue* or *green*. However the bound states are colourless.

## 1.2 Gauge Bosons

Interactions between the fermions occur by the exchange of one or more particles, known as *gauge bosons*. The properties of the gauge bosons are shown in Table 1.3. These fundamental interactions are characterised by their range and relative intensity. There is a gauge boson associated with each force:

- The electromagnetic force has a single boson called the photon ( $\gamma$ ) associated with it. It can only interact with charged particles, although it is chargeless. Because the photon is massless, the electromagnetic force has an infinite range.
- The weak force has three bosons associated with it, the two charged bosons  $W^\pm$  of mass 80.42 GeV and the chargeless  $Z^0$  boson of mass 91.19 GeV. Being massive particles, the resulting interactions are consequently of short range. The weak force can couple to all the fermions. The  $W^\pm$  and  $Z^0$  can couple to each other and the photon as well.
- The strong force has eight mediating bosons given by

$$\begin{array}{ccc}
 \frac{1}{\sqrt{6}}(r\bar{r} + g\bar{g} - 2b\bar{b}) & r\bar{g} & r\bar{b} \\
 & b\bar{r} & b\bar{g} \\
 g\bar{r} & g\bar{b} & \frac{1}{\sqrt{2}}(r\bar{r} - g\bar{g})
 \end{array} \tag{1.1}$$

They are called *gluons* and are exchanged between the quarks. The gluons have zero electric charge and are also massless like photons. They couple to colour charges of particles and have non-zero colour charge. In addition, gluons can couple to other gluons.

The weak and electromagnetic interactions are collectively referred to as the *electroweak interaction*. They were successfully unified by Weinberg and Salam independently. The theory was extended and generalised by Glashow in 1970.

Table 1.3: The vector bosons [3].

Interaction	Vector boson (spin 1)	Mass (GeV)	Electric charge ( $\times e$ )	Range (cm)
Weak	$W^\pm$	$80.423 \pm 0.039$	$\pm 1$	$< 10^{-14}$
	$Z^0$	$91.188 \pm 0.002$	0	
Electromagnetic	$\gamma$	0	0	$\infty$
Strong	$g$	0	0	$\infty$

### 1.3 The Higgs Mechanism

Interactions mediated by spin-1 bosons are described by *gauge theory*. Gauge theory possesses invariance under a set of transformations whose parameters are space-time dependent. Gauge invariance is an important symmetry which is associated with these bosons and it has its origin in the study of electromagnetic interactions. For electromagnetism, the local complex phase transformations of the fields of the charged particles are taken as the gauge transformations [5].

Gauge invariance requires the spin-1 bosons to be massless. This holds for Quantum Electrodynamics (the theory describing electromagnetic interactions) and Quantum Chromodynamics (the theory describing strong interactions) because the bosons do indeed have no mass. The problem arises when considering the electroweak interactions, which is a gauge theory based on  $SU(2) \otimes U(1)$ , because the  $W^\pm$  and  $Z^0$  are quite heavy. Thus, gauge invariance is not preserved. This paradox is overcome by introducing the *Higgs mechanism* [2].

It is possible for a theory to possess the required gauge invariance and yet have physical quantum states that are not invariant under gauge transformations. The invariance is broken as a consequence of quantising the theory. There are two main outcomes arising from the spontaneous symmetry breaking. The first is

that the gauge bosons can acquire a mass without violating the gauge invariance of the interactions. The other consequence is the existence of a scalar (spin-0) particle, that is electrically neutral, called the Higgs boson [5].

## 1.4 Electroweak Symmetry Breaking

Experimentally observing the Higgs boson will prove vital to having a “better understanding of the mechanism of electroweak symmetry breaking” [6]. The process  $W_L W_L \rightarrow W_L W_L$  which denotes the scattering of longitudinally polarised vector bosons is extremely sensitive to the physics of electroweak symmetry breaking. This is because perturbative unitarity is violated in this specific channel at a centre-of-mass energy of 1.2 TeV [7].

Upper and lower bounds on the mass of the Higgs boson can be set due to the requirements of the stability of the electroweak vacuum and the perturbative validity of the Standard Model. These bounds depend on the cut-off value of the energy scale  $\Lambda$  up to which the Standard Model is assumed to be valid. A few scenarios for the Higgs mass arising because of the cut-off value of  $\Lambda$  are [6]:

- the Higgs mass is expected to be in the range between  $130 < M_H < 190$  GeV if the cut-off value is chosen at the Grand Unified Theory (GUT) scale, which will imply that no new physics is seen up to that scale.
- the mass of the Higgs is between 50 GeV and 800 GeV if the cut-off value  $\Lambda$  is taken as 1 TeV.

The limit on the mass of the Higgs boson is very dependent on the physics model used. A model independent treatment of physics well below  $\Lambda$  for the case where there is no light Higgs particle or no new physics below some  $\Lambda$  can be developed. The Electroweak Chiral Lagrangian (EWChL) acts as a foundation for such a model. Chapter 4 provides a more detailed description of the EWChL.

Above 160 GeV, the  $ZZ$  decay modes are the main discovery channel of the Higgs boson, while the  $WW$  channels are important around an energy of 600 GeV [6]. Studies [6] have previously been done on the process  $W_L W_L \rightarrow W_L W_L$  at high energy hadron colliders in order to search for a heavy Higgs. This thesis differs from these studies in that it focuses on the study of the  $WW$  scattering using a model that is **not** the Standard Model and a model that does **not** contain any Higgs.

# Chapter 2

## The LHC and the ATLAS Detector

This chapter contains a brief description of the LHC and the ATLAS experiment, summarising the main concepts in [6] and [8]. A description of the LHC machine and the motivation behind its conception will be given. An overview of the ATLAS detector will follow, together with the reasons for its various subdetectors.

### 2.1 Terms Used

The  $z$ -axis is the direction along which the beam travels, while the  $x$ - $y$  plane is the transverse plane to the direction of the beam. Section 2.2 provides more detail of the coordinate system for the ATLAS detector. The azimuthal angle  $\phi$  is measured around the beam axis and  $\theta$  denotes the angle from the beamline.  $\tan\phi$  is equal to  $p_y/p_x$ , where  $p$  denotes momentum. The term pseudorapidity is often used and it can be defined as  $\eta = -\ln \tan(\frac{\theta}{2})$ . Granularity is defined as  $\Delta\eta \times \Delta\phi$ .

### 2.2 The Large Hadron Collider

In December 1994, delegates from the 19 member states of CERN approved a resolution to allow the construction of the Large Hadron Collider (LHC), a machine



which would provide significant progress in High Energy Physics. The LHC is primarily a proton-proton collider being built at CERN, however it can also be used as a heavy ion (Pb-Pb) collider [9]. This analysis deals with proton-proton collisions at the LHC and therefore there will be no further mention regarding the physics of heavy ion collisions.

The LHC is being installed in the existing 27 km circular tunnel built for the Large Electron-Positron collider (LEP), making use of already existing infrastructure to produce, accelerate and store protons [10]. A proton linac produces these protons which are eventually accelerated to 50 MeV, followed by injection into the 1.4 GeV Proton Synchrotron Booster (PSB). The Proton Synchrotron's functions are to accelerate the protons to 26 GeV and deliver a beam of 135 bunches, containing  $10^{11}$  protons at 25 ns intervals. The Super Proton Synchrotron (SPS) then accelerates the protons to 450 GeV to finally inject them into the LHC. Figure 2.1 shows the injector complex and the LHC main ring. These protons will then be accelerated to 7 TeV. As a p-p collider, the proton collisions are produced at a centre-of-mass energy of 14 TeV with a very high luminosity of  $10^{33}$ - $10^{34}$   $\text{cm}^{-2}\text{s}^{-1}$ . There is also an upgrade plan to operate with a luminosity of  $10^{35}$   $\text{cm}^{-2}\text{s}^{-1}$  [11]. A summary of the main machine parameters is given in Table 2.1.

Due to the fact that the LHC will be colliding two beams of equally charged particles, two separate beamlines are required to allow the beams to circulate in separate and opposite directions. Therefore the magnetic field line for one beamline must be in opposite direction to that of the other beamline. Space restrictions in the LEP tunnel means that there is hardly enough room for two separate magnets. This led to the design of a two-in-one magnet, which combines two guide fields into a single magnet design [12]. The two-in-one magnet is made up of two coils and the magnetic channels will be housed in the same mechanical structure and cryostat, a unique configuration saving not only space but also 25% of the cost as compared to having two separate magnets [13].

To be able to accelerate the protons to the LHC design energy and bend the beam around the LEP tunnel, the 14.2 m magnets will be superconducting with a field strength of around 8.4 T, “over five times those used a few years ago at the SPS proton-antiproton collider, and almost 100,000 times the earth’s magnetic field” [13].

Table 2.1: The design parameters at the LHC for p-p collision [14].

Ring circumference	27 km
Beam energy	7.0 TeV
Centre-of-mass energy	14.0 TeV
Injection energy	450 GeV
Initial luminosity	$10^{33} \text{ cm}^{-2} \text{ s}^{-1}$
Luminosity	$10^{34} \text{ cm}^{-2} \text{ s}^{-1}$
Luminosity lifetime	10 h
Bunch spacing	25 ns
Particles/Bunch	$1 \times 10^{11}$
Number of bunches per ring	2835
R.M.S bunch length	7.5 cm
Dipole field	8.3 T
Coil aperture	56 mm
Aperture separation	194 mm

At the LHC there will be a total of 1,296 dipole magnets. In addition to these dipoles, more than 2,500 other magnets will be used to guide and collide the LHC beams. These range from small, normally conducting bending magnets to large, superconducting focusing quadrupoles [13]. These superconducting quadrupole magnets are 3.1 m long with a field of 6.9 T and they are used to focus the beam.

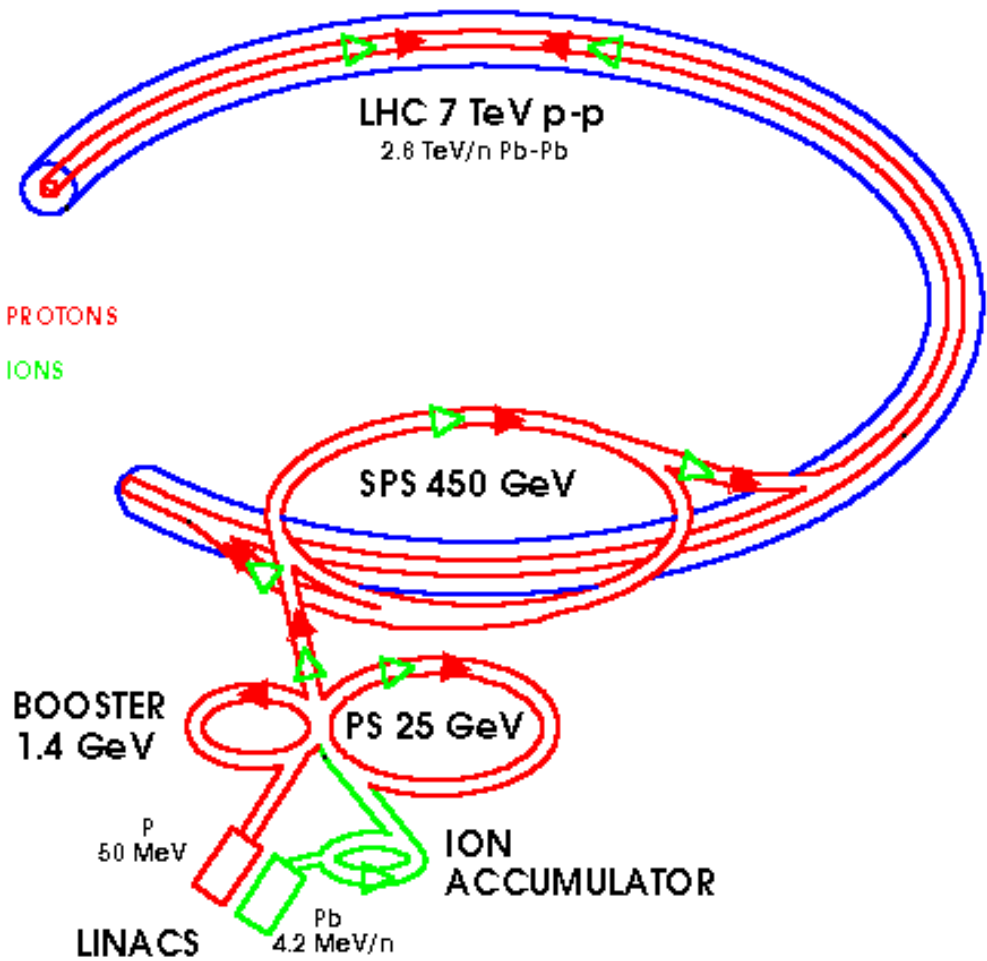


Figure 2.1: The LHC injector complex. Taken from [16].

To maintain an effective physics programme at such a high energy  $E$ , the luminosity of the LHC machine (a quantity proportional to the number of collisions per second) should proportionally increase with  $E^2$ . This arises due to the fact that the De Broglie wavelength associated with a particle decreases as  $\frac{1}{E}$ , causing the cross-section of the particle to decrease as  $\frac{1}{E^2}$ . At the LHC the luminosity is expected to reach  $L = 10^{34} \text{ cm}^{-2}\text{s}^{-1}$ . Each of the two rings will be filled with 2,835 bunches of  $10^{11}$  particles each in order to allow such a high luminosity reach. However, the main drawback of such a system is the resulting large beam cur-

rent of 0.53 A, which will prove to be a particular challenge to a machine made of delicate superconducting magnets operating at cryogenic temperatures. Such a high luminosity also puts severe demands on the LHC detectors in areas of radiation hardness and speed of readout [15].

The LEP tunnel imparts to the LHC an eightfold symmetry and consequently, eight possible interaction points around the ring as shown in Figure 2.2 . These are not all used for experiments though [17]. The LHC beams will cross at four interaction points, used for collision experiments planned for the LHC. These experiments are [10]:

- ATLAS - a high luminosity general purpose proton-proton detector situated at interaction point 1.
- CMS - similar detector to ATLAS situated at interaction point 5. Both CMS and ATLAS will be used to exploit the full discovery potential of the LHC machine.
- LHCb - a beauty physics experiment located at interaction point 8. Its purpose is to allow for more progress in the field of CP violation and rare decays by taking precise measurements.
- ALICE - a heavy ion detector located at interaction point 2. It owes its existence to physics study of strongly interacting matter at extreme energy densities.

As mentioned above, ATLAS is situated at interaction point 1 and the positive  $z$ -direction in this thesis refers to the direction in the LHC region 1 pointing towards the interaction point 8.

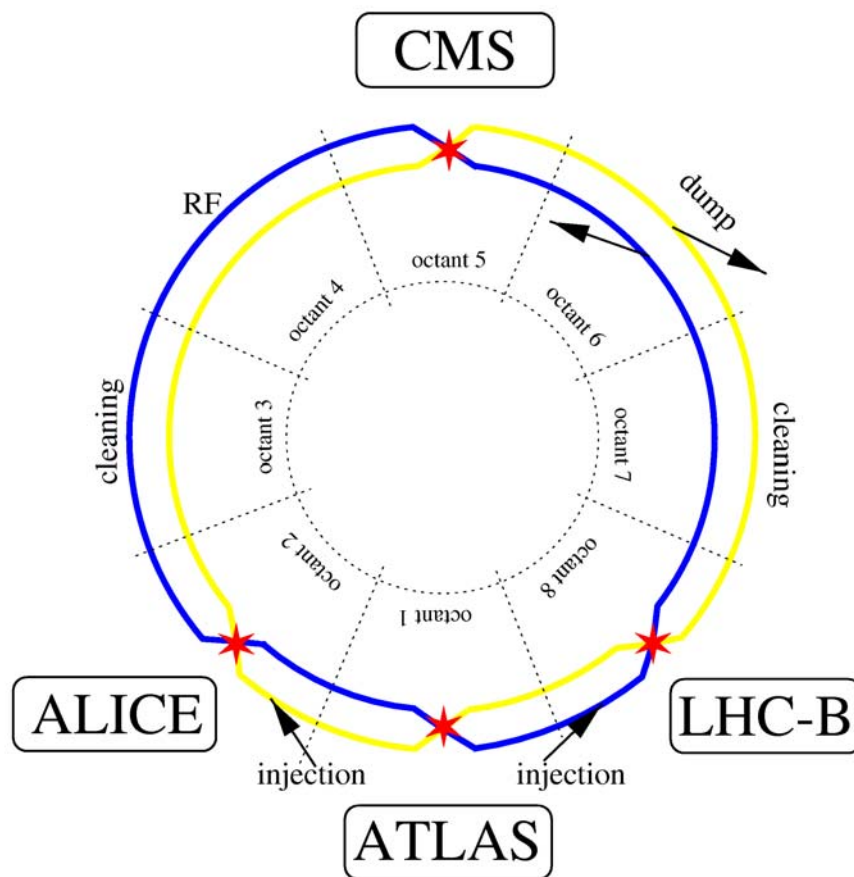


Figure 2.2: The layout of the LHC. Taken from [17].

### 2.3 Motivation behind the ATLAS Detector

ATLAS (*A Toroidal LHC ApparatuS*), one of the proposed detectors for the LHC, is the only one discussed in detail in this thesis. It is a general-purpose detector designed by a collaboration of approximately 2,000 physicists, working at 150 institutions in 34 countries. In October 1992, a Letter of Intent [18] was submitted to the LHC Committee (LHCC) by the ATLAS Collaboration. Published in December 1994, the ATLAS Technical Proposal [6] contains a more detailed design of ATLAS. The experiment is scheduled to make its first physics run in 2007, depending upon completion of the LHC machine [17].

### 2.3.1 Higgs searches

SM predictions for new physics, such as the quest for the origin of spontaneous symmetry breaking in the electroweak (EW) sector of the SM, has strongly guided the design of the ATLAS detector. The search for a SM Higgs boson,  $H$ , (a possible manifestation of this symmetry breaking), or the family of Higgs (two charged Higgs  $H^\pm$ , two CP-even Higgs bosons  $h$  and  $H$ , and a CP-odd Higgs boson  $A$ ) in the Minimal Supersymmetric extension of the Standard Model (MSSM), is thus a prime benchmark when optimising the detector design [9, 6]. For a SM Higgs, ATLAS must be sensitive to the following processes:

- $H \rightarrow b\bar{b} : 80 < M_H < 100 \text{ GeV}$
- $H \rightarrow \gamma\gamma : 90 < M_H < 150 \text{ GeV}$
- $H \rightarrow ZZ^* \rightarrow 4l (l = \mu, e) : 130 \text{ GeV} < M_H < 2M_Z$
- $H \rightarrow ZZ \rightarrow 4l$  and  $H \rightarrow ZZ \rightarrow ll\nu\nu : M_H > 2M_Z$
- $H \rightarrow WW \rightarrow l\nu jj$  and  $H \rightarrow ZZ \rightarrow lljj : M_H$  up to 1 TeV

When searching for the MSSM Higgs, ATLAS is required to be sensitive to the following:

- $A \rightarrow \tau\tau \rightarrow e\mu + \nu$ 's
- $H^\pm \rightarrow \tau^\pm + \text{hadrons} + \nu$ 's
- $H^\pm \rightarrow 2 \text{ jets}$

The Higgs decay products include photons,  $b$ -quarks,  $Z$ ,  $W$ ,  $\tau$ , jets and indirectly produced leptons and neutrinos. The cross-sections of most of the Higgs processes written above are small over most of the mass range explorable at the LHC. Operating at a high luminosity and maximising the detectable rates above backgrounds by high-resolution measurements of electrons, muons and photons are therefore vital due to the small cross-sections.

### 2.3.2 SUSY searches

Another important goal for ATLAS is to search for supersymmetric particles. Supersymmetric extensions of the SM predict that many new particles can exist over a large mass range. According to SuperSymmetry (SUSY), every elementary particle has a partner which is identical to it in all respects except for its spin and mass. The LHC will have access to a wider spectrum of mass than any previous machine has had. This will enable it to carry out supersymmetric particle searches in mass regimes that have never been explored before. To take full advantage of the signature of the undetected lightest stable SUSY particle, the detector must meet stringent hermeticity and missing transverse energy ( $E_T^{miss}$ ) requirements.

### 2.3.3 Top physics

When discovered at Fermilab in 1995, the top quark completed the three-generation structure of the SM. The Tevatron has examined various properties of the top quark. These include the measurements of the top mass [19] and the cross-section measurement for top production amongst others [20]. However, most of these measurements have been limited by the low statistics of top quarks collected at the Tevatron until now. “The LHC is, in comparison, a top factory, producing about 8 million  $t\bar{t}$  pairs per experiment per year at low luminosity ( $10 \text{ fb}^{-1}/\text{year}$ ), and a few million (anti-)tops in EW single (anti-)top production” [21]. Therefore, the LHC will be able to examine the top quark properties with great precision.

### 2.3.4 B-physics

The LHC will provide an environment in which extensive  $B$ -physics studies can be carried out. This is because the cross-section for  $b$ -quark production at the LHC is many orders of magnitude higher than that for  $B$ -physics experiments at  $e^+e^-$  machines. Hence a wide range of precision measurements can be performed.

The main focus of the ATLAS  $B$ -physics programme is to test the Standard Model through precision measurements of  $B$ -hadron decays. ATLAS expects to be able to measure CP-violation through a number of  $B$ -decay channels. The main emphasis will be on the study of CP violation in the  $B_d^0$  system. The following decay channels are very promising for the study of CP violation and have been identified by ATLAS as benchmark channels for detector optimisation for ATLAS  $B$ -physics [10]:

- $B_d^0 \longrightarrow J/\Psi K_s^0$
- $B_d^0 \longrightarrow \pi^+ \pi^-$
- $B_s^0 \longrightarrow J/\Psi \phi$

Studies of the  $B_s^0$  system, searches for rare decays such as  $B_d^0 \longrightarrow \mu^+ \mu^-$  and  $B_s^0 \longrightarrow \mu^+ \mu^-$ , the study of  $B$ -baryon decay dynamics and the spectroscopy of rare  $B$ -hadrons are among a few other physics studies that are central to the ATLAS  $B$ -physics programme [9].

$B$ -physics studies will generally be easiest during the first few years of the LHC when the luminosity will be low (integrated luminosity in one year = 10 fb<sup>-1</sup>) and the effect due to the overlap of hard scattering events with several soft collision events arising at the same time (making the interpretation of the event complicated) are small. This effect is a direct consequence of the high bunch-crossing rate, meaning that none of the particles created at bunch-crossing will have had time to leave the detector. The term **pile-up** is often used to describe this effect. However,  $B$ -physics studies will still be performed by ATLAS even during the high luminosity phase at the LHC.

Tracks from the decays of  $B$ -hadrons will typically be of low transverse momentum ( $p_T$ ). The ATLAS detector will have strong features for studying  $B$ -physics and a few requirements on the ATLAS detector are [10]:



- good reconstruction of tracks down to a  $p_T$  of 0.5 GeV,
- particle identification at low  $p_T$  for triggering and tagging decays,
- excellent primary and secondary vertex reconstruction for proper time measurements and background rejection,
- good reconstructed mass resolution for  $B$ -meson separation and background rejection,
- charge determination for lepton and jet charge tagging.

### 2.3.5 Other searches

Detection of new, heavy gauge bosons  $W'$  and  $Z'$  of masses up to 5-6 TeV requires high-resolution lepton measurements and charge identification even in the  $p_T$  range of a few TeV. ATLAS will explore other new physics, such as studies of the compositeness of the fundamental fermions. Many theoretical models beyond the SM predict the existence of leptoquarks. Their origin is due to the symmetry between quark and lepton generations. If quarks and/or leptons exhibited compositeness, ATLAS would be able to observe any deviations from the SM [17].

## 2.4 Detector design constraints

The above mentioned physics topics have had a vital impact on the detector design. The goal of making extensive beauty and top studies has imposed many constraints. Some of them are precise secondary vertex determination, full reconstruction of final states with relatively low- $p_T$  particles and low- $p_T$  lepton first-level trigger thresholds as well as second-level track triggering capability. The first-level trigger decides what events to keep and reject and at the second-level, only interesting information identified by first-level trigger is kept. This set of examples demonstrates the changing emphasis when LHC will evolve from initial

low to high-luminosity running. The basic design considerations for ATLAS can therefore be summarised as follows [6]:

- very good electromagnetic calorimetry for electron and photon identification and measurements;
- hermetic jet and missing  $E_T$  calorimetry;
- efficient tracking at high luminosity for lepton momentum measurements, for b-quark tagging, and for enhanced electron and photon identification;
- $\tau$  and heavy-flavour **vertexing**. Tracks coming from the decay of a short-lived particle produced in the collision of a colliding beam experiment can be accurately reconstructed and seen to emerge from a “vertex” point that is different from the collision point. The term **vertexing** is often used to describe this.
- stand-alone, precise,  $\mu$  momentum measurements up to the highest luminosity;
- very low- $p_T$  trigger capability at lower luminosity;
- large acceptance in pseudorapidity,  $\eta$ , as well as almost full azimuthal,  $\phi$ , coverage;
- triggering and measurements of particles at low  $p_T$  thresholds together with high precision for most physics processes;

Even at high luminosity, pile-up in detectors will be unavoidable. Detectors will be required to have a very fast response time in order to minimise the effect due to pile-up. This problem can be solved by using detectors with high granularity. Furthermore, a high luminosity will also lead to a high radiation environment. Hence, radiation hardness of detectors is of utmost importance [10].

## 2.5 The ATLAS Detector

### 2.5.1 Overall detector concept

Figure 2.3 shows the layout of the ATLAS detector and Figure 2.4 gives a cross-sectional view of the detector. It has the familiar tracker-calorimeter-muon chamber onion skin configuration [17] as depicted in Figure 2.4. Cylindrical in shape, the detector has a total length of 42 m and a radius of 11 m. It weighs 7,000 tonnes. Mechanically, the detector is divided into three different sections, namely the barrel in the central region and two end-caps at either end of the barrel. The overall layout of the ATLAS detector consists of the inner detector, the electromagnetic and hadronic calorimeters, the muon spectrometer and the magnet system. Overall trigger and data acquisition system as well as the offline computing requirements are also present [10].

The magnet configuration largely determines the geometry of the ATLAS detector. A superconducting solenoid surrounds the inner tracking cavity. The calorimeter, itself surrounded by superconducting air-core toroids consisting of independent coils with eight-fold  $\phi$  symmetry, is found on the outside of the magnet system. Because of the magnet configuration, it is possible to build a high-resolution, large acceptance, robust and stand-alone muon spectrometer with very little constraints on the calorimeter and inner detector [17].

The inner detector is found at the innermost radius in the central region. It is contained within a cylinder of full length 6.8 m and radius 1.15 m. Surrounded by a solenoid providing a 2 T magnetic field parallel to the beam axis, the inner detector is essential for high pattern recognition and momentum and vertex measurements with the main emphasis on high precision and efficiency. This is achieved by combining discrete high-resolution pixel and strip detectors in the part of the tracking volume closest to the interaction point with continuous straw-

tube tracking with transition radiation capability in the outer part of the tracking volume [10].

Highly granular **liquid argon (LAr) electromagnetic sampling calorimetry** is situated external to the inner detector. Present in both the barrel and end-cap region, its purpose is to identify and measure photons and electrons. The LAr electromagnetic (EM) calorimeter is employed in the pseudorapidity range  $|\eta| < 3.2$  in order to give excellent performance in terms of energy and position resolutions. The EM calorimeter in the barrel and extended barrel region is surrounded by the **hadronic scintillating tile calorimeter**, which constitutes the bulk of the hadronic calorimeter. The end-caps of the EM calorimeter share cryostat with a **hadronic LAr calorimeter**. The same cryostat also houses the **LAr forward calorimeters** which cover a pseudorapidity range of  $3.2 < |\eta| < 4.9$ .

Contained within a cylinder of outer radius 2.25 m, the LAr calorimetry extends to 6.65 m along each length of the beam axis. The bulk of the hadronic calorimetry is based on a novel scintillating tile technique, and it has an outer radius of 4.25 m. It extends in length to 6.10 m. The tile calorimeter is separated into a large barrel and two smaller extended barrel cylinders, one on each side of the barrel. “The whole calorimeter system contributes to the very good jet and  $E_T^{miss}$  performance of the detector. The total weight of the calorimeter system, including the solenoid flux-return iron yoke which is integrated into the tile calorimeter support structure, is about 4,000 tonnes” [6].

The calorimeter is surrounded by the muon spectrometer. The latter contains three stations of high precision tracking chambers. In the toroidal magnetic field, these chambers allow excellent momentum resolution to be obtained. A fast trigger is mounted on each muon chamber. This is achieved by equipping the muon instrumentation with resistive plate chambers (RPCs) which have a very fast time response.

The muon spectrometer defines the ATLAS detector’s overall dimension. The

outer chambers of the barrel are situated at a radius of about 11m. The half-length of the barrel toroid coils is 12.5 m, and the third layer of the forward muon chambers is located about 23 m from the interaction point. The third layer of the forward muon chamber is mounted on the cavern wall.

The ATLAS magnet system provides the bending power needed to measure the momenta of charged particles. The air core toroid system is 26 m long, with an outer radius of 10 m determined by the barrel toroid, and occupies a volume of 8,000 m<sup>3</sup> [10]. Along with the magnet power system, controls, cryogenics and refrigeration plant, the magnet system is made up of four magnet subsystems. They are [10]:

- the central solenoid, which provides a magnetic field of 2 T to the inner detector;
- the air-core barrel toroid;
- two air-core end-cap toroids (ECT), which provide a toroidal configuration to the muon spectrometer.

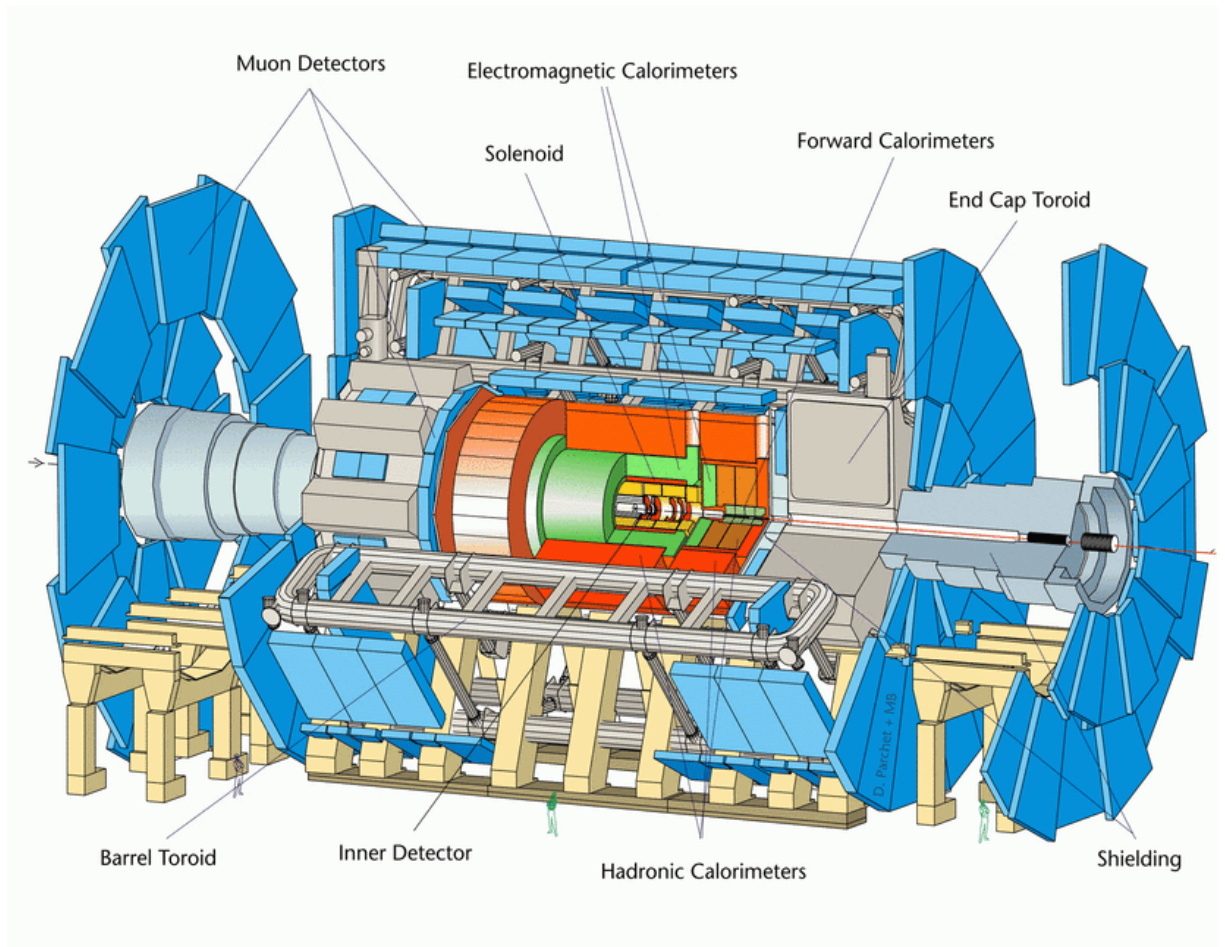


Figure 2.3: The ATLAS detector. Taken from [6].

## 2.5.2 The inner detector

A three-dimensional view of the inner detector is shown in Figure 2.5. The inner detector is located inside all of the other detector components, closest to the beam line and its main purpose is to:

- reconstruct with high efficiency particle tracks and decay vertices in any event.
- make high-precision measurements of leptons and identify electrons and photons at high luminosities.

## ATLAS Detector

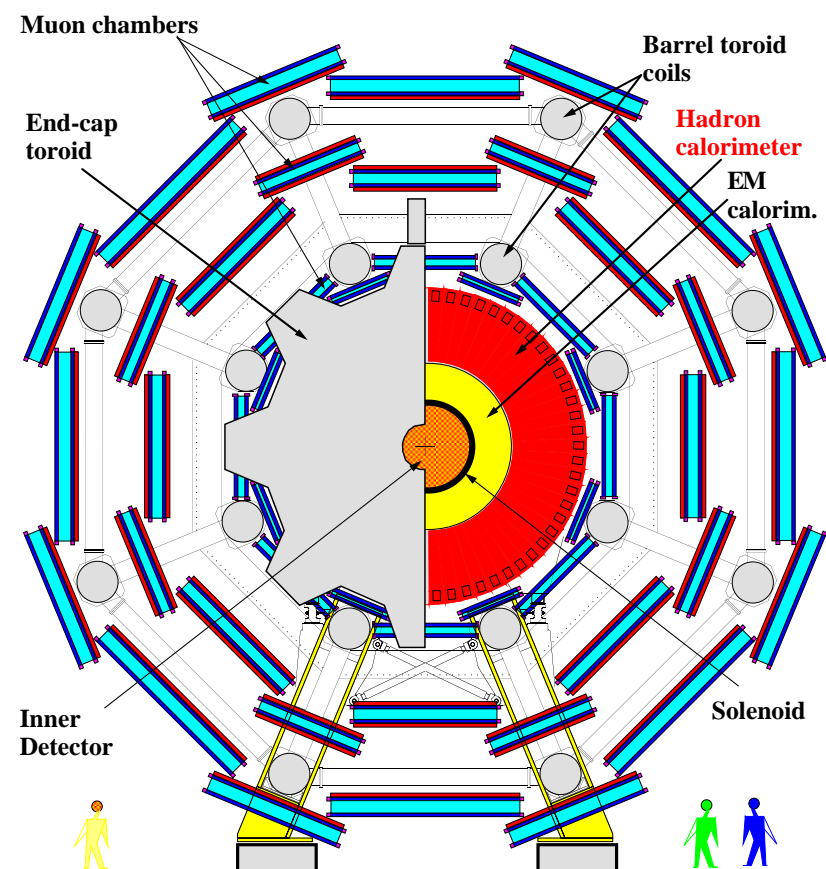


Figure 2.4: Section through the ATLAS detector. Taken from [16].

- perform  $\tau$  and  $b$  tagging at lower luminosities.

Major physics requirements for the inner detector are [17, 10]:

- coverage over the pseudorapidity range  $|\eta| \leq 2.5$ ;
- transverse momentum resolution better than 30% at  $p_T = 500$  GeV;
- high tracking efficiency for isolated and associated tracks whilst keeping the rate from fake tracks low;
- good identification of charge of high- $p_T$  tracks;

- good identification of electrons, photons and jets;
- high-efficiency b-tagging;
- precise secondary vertexing;
- identification of primary vertex;
- identification of a high- $p_T$  track to reduce the level-1 EM cluster trigger rate from di-jet events;
- tracking trigger at Level 2;

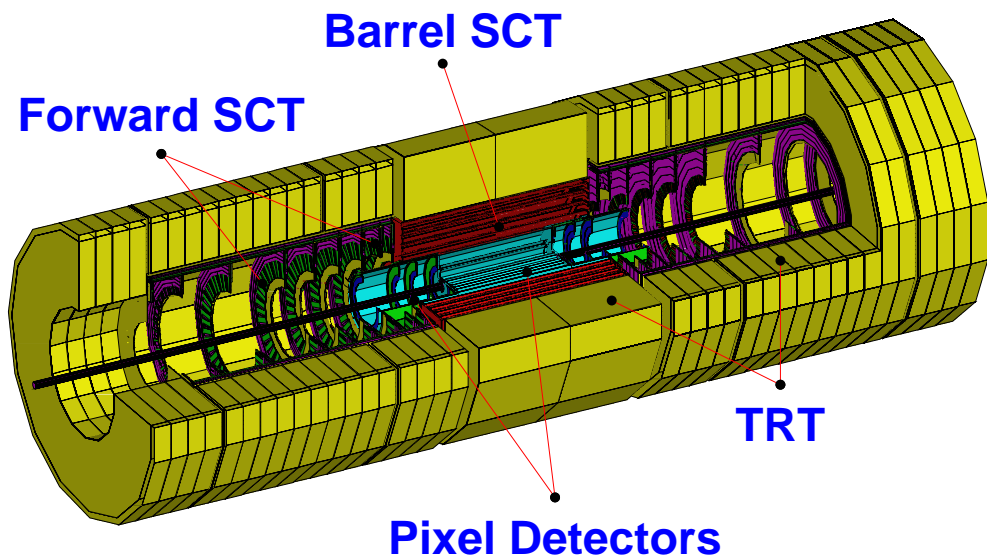


Figure 2.5: The inner detector. Taken from [16].

High granularity tracking allows high precision measurements to be made in order to achieve the high track density and the stringent momentum and spatial resolution targets. To maximise the capability of resolving any ambiguity resulting from overlapping tracks, secondary interactions and detector inefficiencies, it is important to take a large number of measurements along the length of a given



track. A combination of high precision discrete (i.e. few point) and low precision continuous (i.e. many point) tracking is thought to offer the best possible track finding and track fitting capabilities. The discrete tracking will be made by semiconductor pixel and strip detectors at radii close to the beam axis. Straw drift tubes, located at larger radii, will provide the continuous tracking [17].

The passage of ionising radiation in semiconductors causes the incident radiation to interact with the material of the detector. This creates electron-hole pairs in the semiconductor which are collected by charged electrodes. The geometry is the major difference between strips and pixels. Pixels are closely spaced pads with good two-dimensional reconstruction while strips provide better spatial resolution in one coordinate than the other.

The significant amount of material that these precision layers introduce and the relatively high cost per unit area of semiconductor layers mean that their number has been limited. Therefore, three pixel layers and eight strip layers (four space points) are crossed by each track. In order to obtain a large number of tracking points (typically 36 per track) required for pattern recognition, a straw tube tracker (TRT) is used at higher radii. The straw TRT offers the possibility of continuous track-following with much less material per point and a lower cost. The combination of the two techniques provides very good pattern recognition and high precision in both  $\phi$  and  $z$  coordinates.

The inner detector can be divided into three geometrically and mechanically separate parts. They are a barrel part extending over  $\pm 80$  cm and two end-caps extending to  $\pm 350$  cm along the  $z$ -direction. In the barrel, the pixel and silicon micro-strip detectors are arranged on concentric cylinders around the beampipe, extending in pseudorapidity  $|\eta| < 1.4$ .

The inner detector lies in a 2 T axial magnetic field provided by a solenoid magnet. The outer radius of the whole cavity is 1.15 m, limited by the inner dimension of the cryostat containing the LAr EM calorimeter. The total length

is 6.6 m, fixed by the position of the end-cap calorimeters. The inner detector is centred at the nominal beam crossing point. Table 2.2 gives a summary of the basic design parameters and resolutions for the inner detector.

Table 2.2: Parameters of the inner detector [6].

System	Position	Area (m <sup>2</sup> )	Resolution $\sigma$ ( $\mu\text{m}$ )	$\eta$ coverage
Pixels	1 removable barrel layer (B-layer)	0.2	$R\phi = 12, z = 66$	$\pm 2.5$
	2 barrel layers	1.4	$R\phi = 12, z = 66$	$\pm 1.7$
	5 end-cap disks on each side	0.7	$R\phi = 12, z = 77$	1.7-2.5
Silicon strips	4 barrel layers	34.4	$R\phi = 16, z = 580$	$\pm 1.4$
	9 end-cap wheels on each side	26.7	$R\phi = 12, z = 580$	1.4-2.5
TRT	Axial barrel straws		170 (per straw)	$\pm 0.7$
	Radial end-cap straws		170 (per straw)	0.7-2.5
	36 straws per track			

### The pixel detector

The pixel detector is made up of three barrel layers at average radii of 4 cm, 11 cm and 14 cm. It is also made up of five disks in each end-cap between radii of 11 and 20 cm. The individual sensitive element is a very high granularity pixel,  $50 \mu\text{m}$  in  $(r, \phi)$  and  $300 \mu\text{m}$  in  $z(r)$ . This is the reason behind the effectiveness of the pixel detector system in producing a good track separation. The system is designed to provide very high-granularity and high-precision sets of measurements close to the interaction point. The pixel detector system also provides three precision

measurements over the full acceptance range, and is vital in determining the impact parameter resolution and the ability of the inner detector to find short-lived particles such as  $B$ -hadrons and  $\tau$ -leptons. The innermost barrel layer at radius 4 cm, also known as the  $B$ -layer, is used to resolve the very fast  $B_s^0$  meson oscillations. The  $B$ -layer improves ATLAS's sensitivity to  $B$ -hadrons decays [22]. Because this layer is as close as is practical to the beam pipe, at a radius of 4 cm, its lifetime will be limited by radiation damage and hence, it will need to be replaced after a few years. The mechanical design of the pixel system allows the possibility of replacing the  $B$ -layer [10].

The pixel detector is able to provide three to four measurements along a track. Overlaps in  $z$  (barrel) or  $r$  (end-cap) and in  $(r, \phi)$  means that a single track may give two hits in a single plane in small regions of the detector. The  $B$ -layer covers the entire pseudorapidity range  $|\eta| < 2.5$ . The barrel layers at radii of 11 cm and 14 cm and the four disks on each end-cap provide at least two additional measurements on a track [10].

The major drawback of the pixel detector is its complex readout electronics required for each pixel. The readout chips have a large area and each chip is bonded to the detector substrate so as to achieve the required density of connections. Furthermore, these chips must be radiation hardened to withstand ten years of running at the LHC. The pixel detector system contains 140 million detector elements, each  $50 \mu\text{m}$  in the  $R\phi$  direction and  $300 \mu\text{m}$  in the  $z$  direction.

### **The semiconductor tracker**

The semiconductor tracker (SCT) is designed to make eight precision measurements per track in the intermediate radial range. This contributes to the measurement of impact parameter and vertex position, momentum, in addition to good pattern recognition by the use of high granularity.

The barrel semiconductor tracker is made of eight layers of silicon micro-strip detectors. Precision measurement is achieved by using small angle stereo to obtain a  $z$  measurement. In the barrel, each silicon detector is  $6.36 \times 6.40 \text{ cm}^2$  with 768 readout strips of  $80 \text{ }\mu\text{m}$  pitch. Four silicon detectors make up a module. Two such detectors are wire-bonded together to form 12.8 cm long strips on each side of the module. Two pairs of detectors are then glued back-to-back at a 40 mrad stereo angle. The barrels are positioned at radii 300, 373, 447 and 520 mm.

In the pseudorapidity range  $1.16 < |\eta| < 2.5$ , the transition from barrel to end-cap geometry takes place. The end-cap modules are very similar in construction to the barrel ones but they use tapered strips instead, with one set aligned radially. These modules are mounted in three rings onto nine wheels covering the required pseudorapidity range and the wheels are interconnected by a space-frame.

The detector has a spatial resolution of  $16 \text{ }\mu\text{m}$  in  $R\phi$  and  $580 \text{ }\mu\text{m}$  in  $z$ , per module containing one  $R\phi$  and one stereo measurement. It is possible to distinguish tracks if they are separated by more than  $\sim 200 \text{ }\mu\text{m}$ .

The structures of both the pixel and the SCT systems are designed with materials with a low coefficient of thermal expansion. This is due to the fact that these two detector systems require:

- a very high dimensional stability,
- cold operation of the detectors, and
- the removal of heat generated by the electronics and the detector leakage current.

### **The transition radiation tracker**

The transition radiation tracker (TRT) makes use of straw tube detectors, surrounded by radiator material (foam and foil) [9]. This allows an improved elec-

tron identification capability independent of energy-momentum matching between the calorimeter and the tracker. Electron identification is achieved from the detection of transition-radiation photons created by the passage of electrons in the radiator between the straws.

Each straw is made of aluminium and has a diameter of 4 mm and a maximum length of 144 cm in the barrel. In the barrel, the straws are arranged in concentric layers giving on average 36 hits on each track but with a lower precision than that of the SCT [9]. The barrel consists of 50,000 such straws parallel to the beam axis and with readout at both ends. The end-caps are made of 320,000 radial straws with readout at the outer radius. 420,000 electronic channels make up the TRT. Each channel provides a drift time measurement giving a spatial resolution of  $170 \mu\text{m}$  per straw at two independent thresholds. One threshold is used for tracking hits while the other is used for transition radiation hits.

The barrel section is built from three cylinders and it has an inner radius of 56 cm and an outer radius of 107 cm [9]. The two end-caps contain 18 wheels. The first 14 of them are situated near the interaction point, covering a radius of 64 to 107 cm. The last four wheels extend to an inner radius of 48 cm. The TRT has been designed in such a way as to deal with high occupancy and high counting rate. The layout of the tracking layers is chosen to ensure that a track crosses two pixel layers and four silicon strip superlayers over the pseudorapidity range  $|\eta| < 2.5$ . A transition from barrel to disk geometry occurs at  $|\eta| \sim 1$ . This is done to minimise the amount of material traversed. The spatial resolution of each straw is  $170 \mu\text{m}$ . However, the large number of straws per track means that an accuracy of  $50 \mu\text{m}$  is achieved when averaged over all straws at the LHC design luminosity.

### 2.5.3 Calorimetry

Figure 2.6 gives the layout of the calorimeter. It consists of the liquid argon (LAr) electromagnetic (EM) calorimeter, the hadronic calorimeter (mixture of scintillating tiles and LAr) and the forward calorimeter (EM and hadronic LAr). These can then be divided into barrel, end-cap and forward. A gap is left intentionally between the barrel and end-cap sections at  $|\eta| \sim 1.3-1.5$  for the inner detector and cryostat services.

The EM calorimeter at the inner radius covers a pseudorapidity range of  $|\eta| < 3.2$ , the hadronic barrel calorimeter covers  $|\eta| < 1.7$ , the two hadronic end-cap ones cover  $1.5 < |\eta| < 3.2$ , and the forward calorimeter covers  $3.1 < |\eta| < 4.9$ .

The identification and reconstruction of the energy and position of electrons, photons and jets together with the measurement of  $E_T^{miss}$  are among a few vital requirements of the ATLAS detector. Designed to meet these requirements in the very high luminosity environment of the LHC, the ATLAS calorimeter has an acceptance range of  $|\eta| < 4.9$  [17].

Higgs processes and decays of new heavy gauge bosons  $W'$ ,  $Z'$  to electrons dictate the requirements of the electromagnetic calorimeter.  $H \rightarrow \gamma\gamma$  and  $H \rightarrow ZZ \rightarrow 4e$  place the most stringent requirements on the energy resolution. An EM energy resolution of  $\frac{10\%}{\sqrt{E}} \oplus 0.7\%$  is the main objective. To reach a rejection of  $10^4$  against single jets for sensitivity to  $H \rightarrow \gamma\gamma$ , fine segmentation of the EM calorimeter is needed. Furthermore, a wide dynamic range is required, ranging from 2 GeV (for identifying electrons from semileptonic  $b$  decays) to 5 TeV (for  $Z' \rightarrow ee$  and  $W' \rightarrow e\nu$ ) [17].

The need for identification and measurement of the energy and direction of jets, and precise measurement of  $E_T^{miss}$  have made it necessary to construct a hadronic calorimeter. This calorimeter will enhance the performance of the EM calorimeter by taking measurements of quantities such as leakage and isolation. The goal is to have a hadronic calorimeter energy resolution of  $\frac{50\%}{\sqrt{E}} \oplus 3\%$  in the

barrel (with segmentation  $0.1 \times 0.1$  in  $\eta \times \phi$  space) and  $\frac{100\%}{\sqrt{E}} \oplus 10\%$  in the forward regions (with segmentation  $0.2 \times 0.2$  in  $\eta \times \phi$  space) [17].

## ATLAS Calorimetry (Geant)

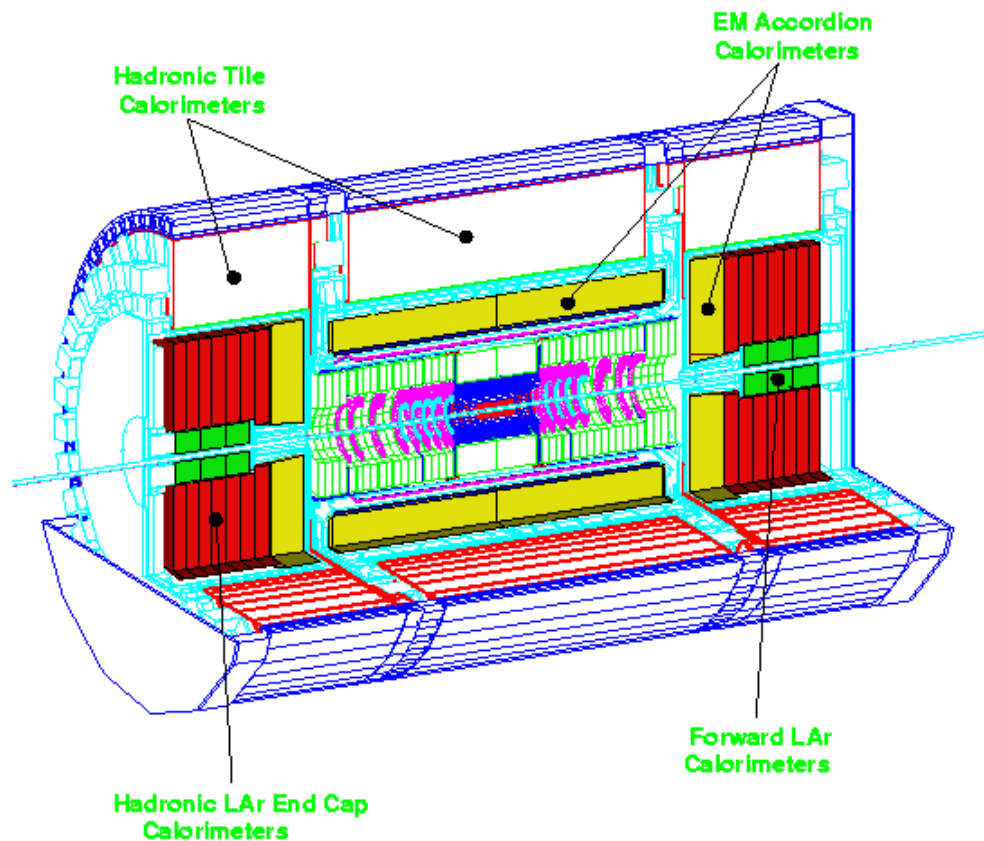


Figure 2.6: View of the ATLAS calorimeter. Taken from [6].

### The electromagnetic calorimeter

The EM calorimeter is divided into two major parts, the barrel and the end-cap together covering a pseudorapidity range of  $|\eta| \leq 3.2$ . The EM calorimeter is a sampling lead LAr detector with Kapton electrodes and lead absorber plates over its full coverage. The thickness of the lead absorbers varies as a function of pseudorapidity to optimise the performance of the EM calorimeter in terms of

energy resolution. Finely segmented presamplers, designed to pinpoint particle position and recover any energy lost in front of the calorimeter (inner detector, coil and cryostat) by early-showering particles, are installed in front of each LAr calorimeters.

The EM barrel calorimeter covers the pseudorapidity region  $|\eta| < 1.4$  and its first sampling, at a depth of  $4.3 X_0$  (radiation length), is finely segmented in  $\eta$  ( $\Delta\phi \times \Delta\eta = 0.1 \times 0.003$ ). The second sampling has a granularity of  $0.025 \times 0.025$  in  $\Delta\phi \times \Delta\eta$  while that of the third sampling is  $0.025 \times 0.05$  in  $\Delta\phi \times \Delta\eta$ . Such segmentation should allow good electron and photon identification and position resolution.

The EM barrel calorimeter consists of two identical half-barrels, separated by a small gap (6 mm) at  $z = 0$ . In order to allow a minimum number of particles to escape through uninstrumented cracks in the detector, it is designed to be hermetic. For this reason, a new accordion geometry is used. The absorber plates are bent into the shape of an accordion, the waves of the plates and the readout electrodes being perpendicular to the incident particles.

The end-cap EM calorimeter is a LAr calorimeter. It is also of an accordion shape but with a fan layout. The end-cap is made of two concentric wheels covering the pseudorapidity range  $1.4 < |\eta| < 2.5$  and  $2.5 < |\eta| < 3.2$ . Up to  $|\eta| < 2.5$ , the granularities in the end-cap are identical to that of the barrel. However the granularity in the first sampling is up to two times less in pseudorapidity. For  $2.5 < |\eta| < 3.2$ , the granularity is  $0.1 \times 0.1$ . The segmentation does not have to be as fine as for the barrel region because most of the processes of interest have high  $p_T$  and are expected to be central [9].

The signals from the EM calorimeters are extracted at the detector inner and outer faces and sent to preamplifiers located outside the cryostats.



### **The hadronic calorimeter**

The ATLAS hadronic calorimeters cover the range  $|\eta| < 4.9$  using different techniques to suit the widely varying requirements and radiation environment over the large pseudorapidity range. The scintillating tile technique is used for the barrel and extended barrel tile calorimeters over the range  $|\eta| < 1.7$ . The intermediate tile calorimeter is placed between the barrel and extended barrel tile calorimeters so as to instrument the gap between them. Over the range  $1.5 < |\eta| < 4.9$ , LAr calorimeters are used.

ATLAS contains a large scintillating tile hadronic calorimeter in the barrel region. It is based on a sampling technique using iron as the absorber material and 3 mm thick plastic scintillator tiles. An innovative design is the unusual orientation of the scintillating plates, placed in perpendicular planes to the colliding beams and staggered in depth. Monte Carlo simulations have predicted that this orientation will provide good sampling homogeneity [17].

The hadronic end-cap calorimeter is a sampling LAr calorimeter using copper plates as the absorber. The end-cap has two major divisions in  $z$ , known as wheels. The first wheel has a 25 mm copper plate while the second one, which is farther from the interaction point, has a 50 mm copper plate. The segmentation is  $0.1 \times 0.1$  for a pseudorapidity range of  $1.5 < |\eta| < 2.5$  and  $0.2 \times 0.2$  for a pseudorapidity range of  $2.5 < |\eta| < 3.2$ .

### **The forward calorimeter**

To have complete coverage of jets for ATLAS, the forward calorimeters are needed. The LAr forward calorimeter will operate in an environment of extreme particle and energy flux. Hence speed and radiation hardness are essential. These are achieved by the use of a metallic tube and rod electrode structure with a very small LAr gap ( $250\ \mu\text{m}$ ), embedded in a copper absorber for the electromagnetic front module, and a tungsten alloy absorber for the two hadronic modules behind it. The tungsten alloy is used to limit the transverse spreading of the hadronic showers [17].

All the three sections contain a metal matrix with longitudinal channels spaced at regular intervals. These channels are filled with concentric rods and tubes. Liquid argon flows between the rods and the matrix and the liquid argon gap is very narrow ( $250\ \mu\text{m}$ ) to avoid build up of positive argon ions in the gap, occurring because of the high energy flux in that region [9].

### **2.5.4 The muon spectrometer**

Standard Model and MSSM Higgs decays with muons in the final states as well as new vector boson decays are the important processes regulating the performance of the muon spectrometer [10]. Beauty physics, CP violating channels particularly, have also had an important factor in the design of the muon spectrometer [23]. The function of the muon spectrometer is to [10]:

- identify, reconstruct and measure the momenta of muon tracks. Transverse momentum resolution must be maintained down to 5 GeV and pseudorapidity coverage of up to 3 is required;
- trigger on both single-muon and multi-muon events. The trigger system must have a wide acceptance, be efficient and selective;

- associate all muons unambiguously with the correct bunch crossing by making use of timing information provided by the trigger chambers;

For track reconstruction in rare processes, a wide pseudorapidity coverage of up to  $\eta \sim 3$  is vital. Momentum and mass resolutions of the order of 1% are needed to reconstruct narrow final states with two or four muons, to reject background and to identify charge. The muon spectrometer must also be able to measure a second coordinate in the non-bending plane for muon tracks. The spatial resolution is of the order of 5-10 mm. Such a resolution is required to ensure good track reconstruction and momentum measurement [10].

Figures 2.7 and 2.8 show the layout of the muon spectrometer. The muon spectrometer is based on the deflection of muon tracks in the superconducting air-core muon toroid magnet system, instrumented with separate trigger and high-precision tracking chambers. Over the pseudorapidity range  $1.4 \leq |\eta| \leq 2.7$ , two small end-cap magnets inserted at both ends of the barrel toroid bend the muon tracks. For  $|\eta| \leq 1.0$ , the large barrel toroid provides the magnetic bending. Over  $1.0 \leq |\eta| \leq 1.4$ , magnetic bending is provided by a combination of barrel and end-cap fields. In the barrel, there are three layers of chambers, one at the inner and outer edges of the toroids and one in the mid-plane. In the forward region, the chambers are located one on either side of the end-cap cryostat and a third layer is situated on the cavern wall to maximise the lever-arm.

The chambers have been divided into two categories reflecting their use. One is precision chambers, having good spatial resolution and the other category is trigger chambers with very good time resolution which enables the identification of bunch crossings [9].

### **The precision chambers**

For precision muon tracking, monitored drift tube (MDT) chambers are used at

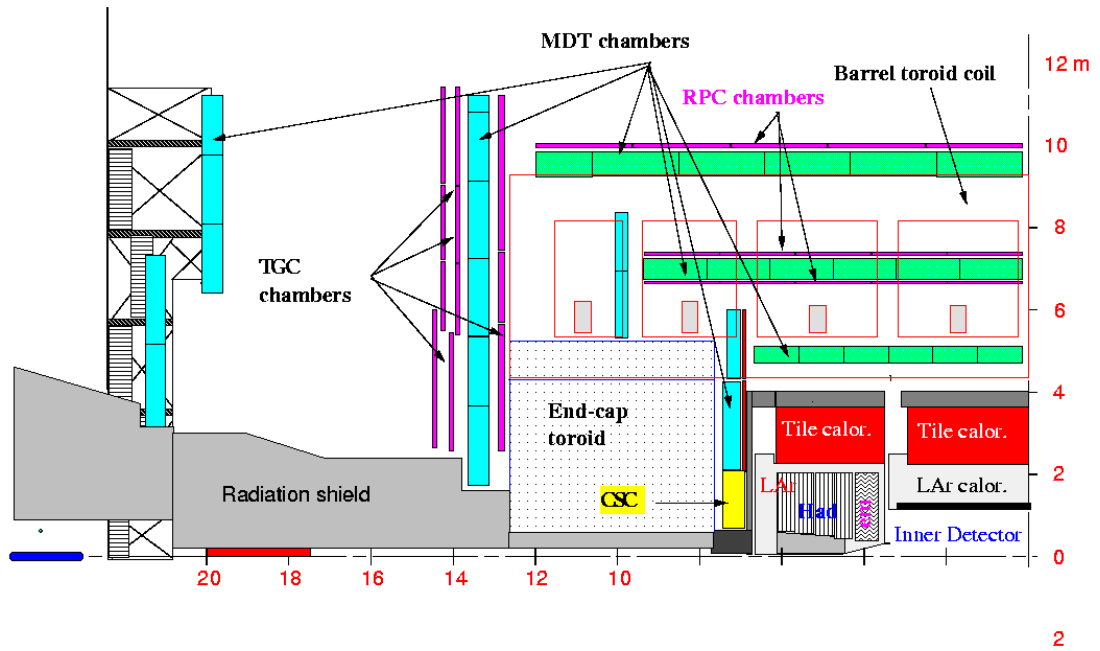


Figure 2.7: Side view of one quadrant of the muon spectrometer. Taken from [16].

low pseudorapidity  $\eta$ , up to  $|\eta| = 2$ . At large values of  $\eta$ , cathode strip chambers (CSCs) are used because of the need for increased granularity due to higher particle fluxes. Table 2.3 shows the number of chambers for the MDT and CSC.

Each muon chamber is made of two multilayers of detectors on either side of a support structure. This structure provides accurate positioning of drift tubes with respect to each other, and mechanical integrity under the effects of temperature and gravity. The MDT chambers are made of two multilayers of three or four planes of pressurised thin-wall aluminium drift tubes with a diameter of 30 mm and  $400 \mu\text{m}$  wall thickness. The tube lengths vary from 70 cm to 630 cm. The pressurised gas is a non-flammable mixture of 93% Ar and 7%  $\text{CO}_2$  at a pressure of 3 bar and has a total volume of  $800 \text{ m}^3$ . At such a pressure, a maximum drift time of  $\sim 700 \text{ ns}$  and a single straw resolution of  $\sim 80 \mu\text{m}$  can be obtained.

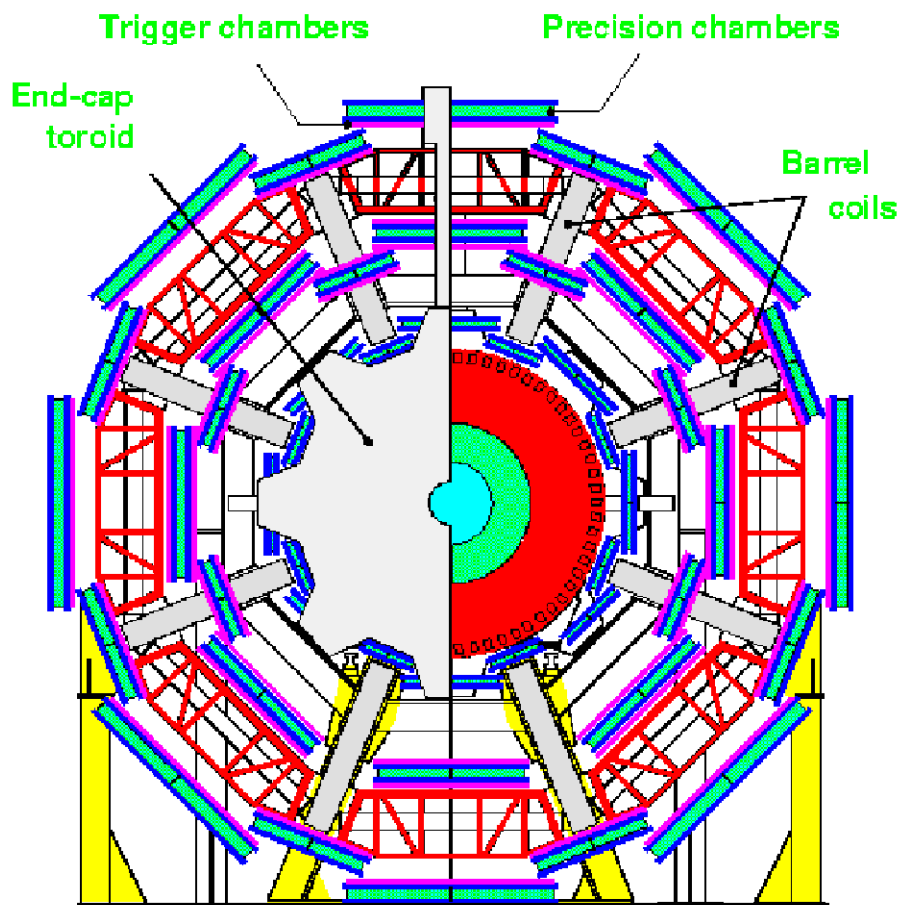


Figure 2.8: Transverse view of muon spectrometer. Taken from [16].

The CSCs are fast multiwire proportional chambers with cathode strip read-out and a symmetric cell in which the anode-cathode spacing is equal to the anode wire pitch. By measuring the charge induced on the segmented cathode due to the formation of an avalanche on the anode wire, a precision coordinate can be obtained. By segmenting the readout cathode and by charge interpolation between neighbouring strips, it is possible to achieve good spatial resolution. For the precision measurement, the cathode strips are orthogonal to the anode wires. The cathode readout pitch is 5.08 mm and the anode wire pitch is 2.54 mm.

The baseline CSC gas is made of a non-flammable mixture of 30% Ar, 50% CO<sub>2</sub> and 20% CF<sub>4</sub>, with a total volume of 1.1 m<sup>3</sup>. A few other important characteristics of the CSCs are:

- small electron drift time of 30 ns;
- good time resolution (7 ns);
- good two-track resolution;
- low neutron sensitivity. The fact that the baseline CSC gas contains no hydrogen, combined with the small gap width, explains the low neutron sensitivity;

Orthogonal strips, oriented parallel to the anode wires, form the second cathode of the chamber. These orthogonal strips give a measurement of the transverse coordinate. Because the spatial resolution of the CSCs is very sensitive to the inclination of the tracks, degradation of the resolution is minimised by installing the CSCs in a tilted position. Hence, stiff tracks coming from the interaction point are normal to the chamber surface. The CSCs are arranged in  $2 \times 4$  layers.

### **The trigger system**

Costs considerations together with the high-rate environment have led to the use of two trigger chamber technologies: Resistive Plate Chambers (RPC) in the barrels and Thin Gap Chambers (TGC) in the forward regions. Table 2.3 gives the number of chambers for the RPC and the TGC.

The RPC is a gaseous parallel plate detector with a space-time resolution of  $1 \text{ cm} \times 1 \text{ ns}$  with digital readout. The RPC unit is a narrow gas gap formed by two parallel resistive bakelite plates, which are separated by insulating spacers. Ionisation electrons are multiplied into avalanches by a high, uniform electric field.

The gas is a mixture of tetrafluoroethane ( $C_2H_2F_4$ ) and  $SF_6$ . Position information is obtained from external pick-up electrodes generated into strips. A trigger chamber is made from two rectangular detector layers, each one of which is read out by two orthogonal series of pick-up strips. The two strips are:

- the  $\eta$ -strips, which are parallel to the MDT wires and provide the bending view of the detector.
- the  $\phi$ -strips which are orthogonal to the MDT wires. These strips provide the second-coordinate measurement needed for the offline pattern recognition.

Since the RPCs use no wires, they are easy to manufacture. The bakelite plates mentioned earlier are separated by polycarbon spacers of 2 mm in thickness. These spacers, which define the size of the gas gap, are glued on both plates at 10 cm intervals. To seal the gas gap, a 7 mm wide frame of the same material and thickness as the spacers is used. Thin layers of graphite paint which are connected to the high voltage supply are used to coat the outside surfaces of the resistive plates. The graphite electrodes are separated from the pick-up strips by 200  $\mu\text{m}$  thick insulating films and these films are glued on both graphite layers. The readout strips are arranged such that the pitch varies from 30.0 to 39.5 mm.

Each chamber is made from two detector layers and four strip panels. Two support panels hold the elements together and thereby provide the required mechanical stiffness of the chambers. The readout strips are optimised for good transmission properties and are terminated at both ends to avoid signal reflections.

The TGC is a wire chamber operating in saturated mode with capacitive readout on the pads (or strips). Signals from the anode wires, arranged parallel to the MDT wires, provide the trigger information together with readout strips arranged orthogonal to the wires. These strips are also used to measure the second

coordinate. The TGC is operated with a highly quenching gas mixture of 55% CO<sub>2</sub> and 45% *n*-pentane (*n*-C<sub>5</sub>H<sub>12</sub>). The volume of the gas is 16 m<sup>3</sup> and it is highly flammable; therefore requiring precautions. The configuration of the electric field together with the small wire distance contributes to a short drift time and hence a good time resolution.

The TGCs are constructed in doublets and triplets of chambers. The inner station, used to measure the second coordinate, is made up of one doublet. There are seven chamber layers in the middle station, arranged in one triplet and two doublets. They provide the trigger and the second coordinate measurements. Between two cathode planes made of 1.6 mm plates on which graphite is deposited is the anode plane. Etched copper strips on the backside of the cathode plates, facing the centre plane of the chamber, provide the readout of the azimuthal coordinate. There are no readout strips for the central layer of a triplet. 20 mm thick paper honeycomb panels, which provide a rigid mechanical structure for the chambers, separate the TGC layers. On the outside, the gas pressure is maintained by 5 mm thick honeycomb panels.

Table 2.3: The muon chamber instrumentation. “Area covered” refers to chamber modules which are normally made of several detectors.

	CSC	MDT	RPC	TGC
Number of chambers	32	1194	596	192
Number of readout channels	67,000	370,000	355,000	440,000
Area covered (m <sup>2</sup> )	27	5,500	3,650	2,900



## 2.5.5 Trigger, data acquisition and computing

The trigger and data acquisition (DAQ) systems are very important at ATLAS. The high rate at which data will be produced at ATLAS means that a high speed system is required to select interesting events and store them while discarding the rest. The rate of events must be reduced from the initial bunch crossing rate of 40 MHz to  $\sim 100$  Hz for permanent storage.

The ATLAS trigger is categorised in three levels as shown in Figure 2.9. They are [17]:

- **Level 1** : a synchronous system of hardware acting at 40 MHz (receiving data every 25 ns). It is based on reduced-granularity information from a restricted subset (calorimeter, muon) of the detector subsystems. During the Level 1 processing, data from all parts of the ATLAS detector are stored in pipeline memories. For each bunch crossing, a yes/no trigger decision is delivered with a fixed target latency (time taken to form and distribute the Level 1 trigger decision) of  $\sim 2 \mu\text{s}$ .
- **Level 2** : an asynchronous system of programmable processors using full granularity data from inner tracking and other detectors. It however only examines Regions of Interest (RoIs) chosen by Level 1 as containing interesting information. It is able to reduce the rate of information by a factor of  $10^3$ .
- **Level 3** : an event filter (EF) using farms of commercial processors with a decision time of up to 1 s. It is the Level 3 trigger that makes the final decision about which events to permanently store, and it does so at a rate of 100 Mbytes/s for subsequent offline analysis. The EF will mainly use offline reconstruction algorithms so as to minimise development and enable comparison of online and offline efficiencies [9].

Computing is a major aspect of the ATLAS experiment. This is due to the large amount of data and high computing performance required for the trigger, DAQ and offline analysis. The Level 2 trigger requires an estimated processing power of  $10^6$  MIPS. The EF has a similar requirement [9]. The anticipated data storage capacity is estimated to be of the order of  $10^{15}$  bytes per year of raw data. This therefore requires new methods for data reduction and selection.

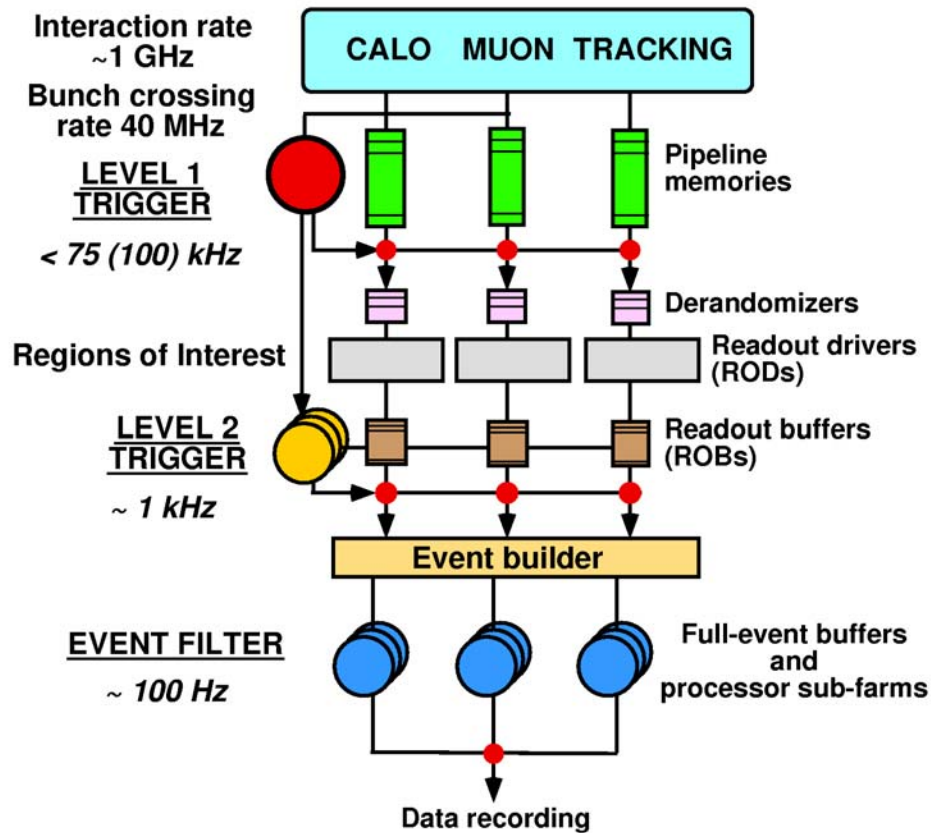


Figure 2.9: Trigger and DAQ system. Taken from [24].

The offline computing system can be divided into these categories [9]:

- reconstruction of events in real time with a delay of  $\sim 1$  hour.

- Monte Carlo event simulation of  $\sim 10\%$  of the real events.
- performance monitoring.

The reconstruction and Monte Carlo production require the main computing power which are estimated at  $3 \times 10^7$  MIPS and  $2 \times 10^6$  MIPS respectively. The total computing power required by ATLAS is expected to be approximately  $34 \times 10^6$  MIPS [9].

# Chapter 3

## Simulation and Reconstruction

Monte Carlo (MC) methods are widely used to simulate high-energy collisions between elementary particles. Such high-energy collisions between these elementary particles give rise to complex final states. The solution to the complexity is mastered by subdividing the main physical problem into a set of simpler separate tasks, where all main aspects of the events are simulated. These can range from hard-process selection to decays. MC methods generate any physics process as predicted by the theory being tested. Hence the generated events should be similar to those observed experimentally [25].

This chapter gives an insight of the tools used to generate Monte Carlo events for the physics analysis presented in this thesis. Section 3.1 deals with the ATLAS offline software while section 3.2 discusses the generation of Monte Carlo events by using the Pythia generator package. Then in section 3.3, a description of the Athena-Atlfast simulation package is given.

### 3.1 ATLAS Offline Software

The ATLAS offline software is made up of a set of programs used to simulate and reconstruct event. These programs are written in C++ and run in the Athena

framework. This section gives a brief description of the Athena framework, followed by the organisation of the ATLAS offline software.

### 3.1.1 Athena and GAUDI

Athena is a control framework that represents a concrete implementation of an underlying architecture. A **framework** itself can be defined as an architectural pattern made up of a set of cooperating classes that make up a reusable design for a specific class of software [26]. An **architecture** consists of the specifications of a number of components and how they interact with each other [27]. A **component** is a block of software which has a well specified collection of methods along with a statement of what each method actually does [28].

Athena is based upon an underlying structure called GAUDI (originally developed for the Large Hadron Collider beauty (LHCb) experiment). It is the specific implementation for ATLAS of the GAUDI architecture, together with ATLAS-specific enhancements like the event data model and the event generator framework [27]. The GAUDI project is still going on today, with the collaboration between ATLAS and LHCb being extended for other High Energy Physics experiments to contribute new architectural concepts to the GAUDI framework.

Figure 3.1 shows the Athena-GAUDI framework. A summary of the concepts used in the Athena framework is provided below. The main Athena-GAUDI components are [27]:

- **Algorithms:** the basic building blocks of user applications. They take input data and produce new output data by manipulating the input data. They can perform tasks like the association of calorimeter hits into clusters and towers, and the association of particle types with tracks and clusters. The *Algorithms* can be simple or composite, and they can act as filters, rejecting any event that does not meet the selection criteria.

- **Services:** globally available software components that provide specific capabilities of the framework [29]. Some examples of *Services* are *Histogram Service* and *Random Number Generator Service*. As the name suggests, *Services* provide a service to their clients. They tend to be hidden behind interfaces such that multiple implementations, selectable at run time, can be provided.
- **Properties:** the control and data parameters for *Algorithms* and *Services*, allowing run-time configuration [29]. Usually the algorithm designer decides which parameters need adjusting. *Properties* are specified via a text file read at startup or interactively at run-time if scripting is enabled.
- **Job Options file:** conventional text file used to control the configuration of an Athena application at run time. One of the main purposes of this file is to allow the user to specify which *Algorithms* should be run.
- **Data Objects:** input and output of *Algorithms*. They are passed between *Algorithms*.
- **Transient Stores:** the temporary repository for *Data Objects*. *Algorithms* locate input information from a transient store and write out newly generated information derived from its processing back into the *Transient Store*, where it can be later retrieved by downstream *Algorithms*. There exist different *Transient Stores* with different lifetime policies. The main ones are: *Event Data Store*, *Detector Data Store* and *Histogram Store*.
- **Converters:** the provider of conversion of objects from one representation to another. They convert *Data Objects* to and from persistent objects. These converters can also convert objects to a graphical representation.

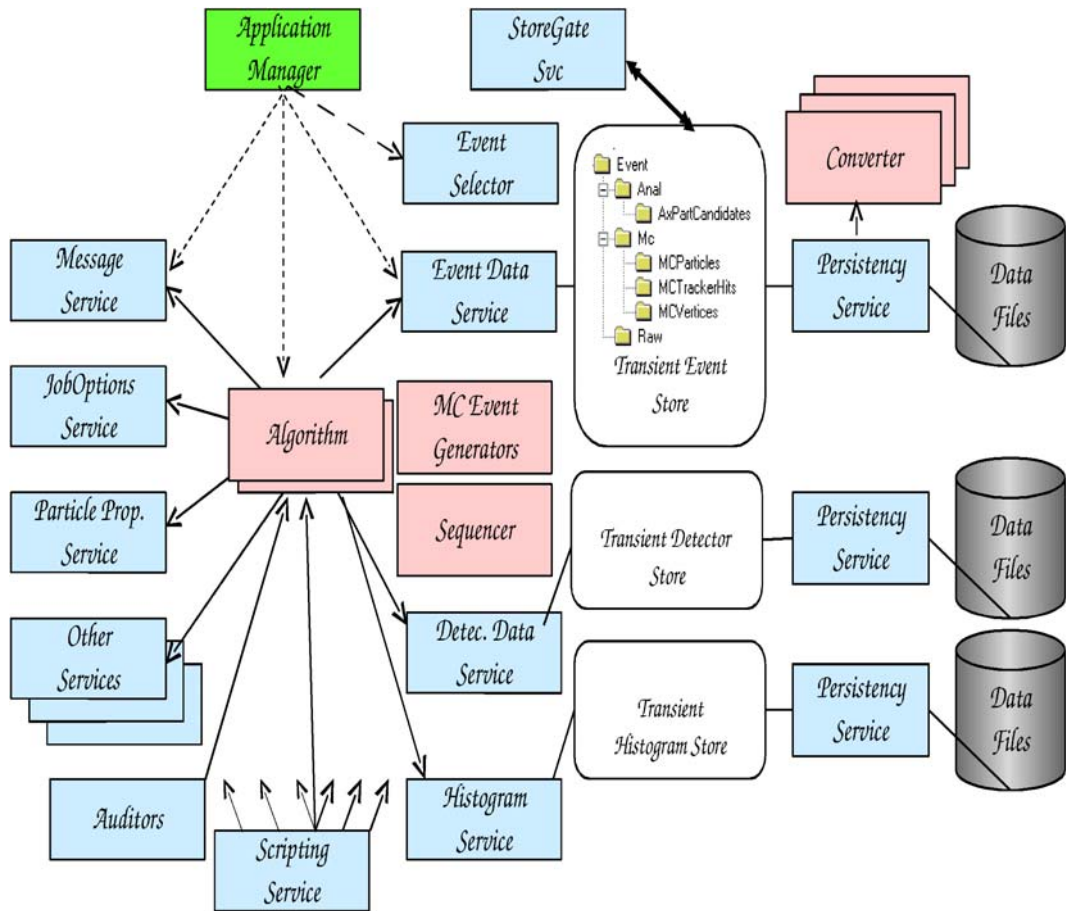


Figure 3.1: The Athena-GAUDI framework. Take from [26].

### 3.1.2 ATLAS offline computing

The ATLAS software environment is based upon *Packages*. A **Package** is a set of C++ classes and *Algorithms* that carry out a common application. Each package usually depends on some other package, leading to the generation of one or more libraries or executables [27].

All packages are kept in a centralised code repository, managed by Concurrent Versions System (CVS). The ATLAS offline software is organised in releases. Each release can be identified by a three-component identifier of the form **i.j.k**. A new version of the ATLAS software is released whenever any modification is made to

the packages [28].

Configuration Management Tool (CMT) is used to compile and link GAUDI libraries and applications and run the required software. The software is grouped into separate packages, where some packages may be related or depend upon each other. This dependency means that a package requires information from other packages. For example this requirement can be the need to link with the library produced in another package. CMT groups together all of the information needed to build or run the build-products of a package into a single file in each package. Using CMT allows the user to work in a rather simple model of development [26].

Athena scripting support is in prototype form. It is an abstract scripting service interface, with the possibility of several different implementations. One of the implementations is based upon the Python scripting language [28] and is the one used in the analysis presented here.

For this thesis, the packages within the **AtlasRelease 6.3.0** are used. The generator level package employed is the *McEventSelector* package that contains the C++ code to interface with different Monte Carlo (MC) generators. *PythiaModule* is used as the MC generator and it is the Athena Algorithms interfacing with the Pythia MC in FORTRAN. Athena-Atlfast is used as the simulation package for fast event simulation. It is described in more detail later in section 3.3.

## 3.2 Monte Carlo Generators

Monte Carlo event generators are frequently used in high-energy physics to generate events. In order to generate a high-energy event, an event generator should contain a simulation of several physics aspects. Reference [25] gives the evolution of an event in some semblance of a time order. Generation of high-energy processes are usually quite complex and a large amount of computer coding is



required to simulate all the physical aspects of the process. The next section gives a summary of the Pythia MC generator used for the analysis in this thesis.

### 3.2.1 Pythia and PythiaModule

Pythia is written in FORTRAN 77 and is also fully compatible with FORTRAN 90. The typical running time is 10-1000 events per second, depending on the process being studied [25]. The Pythia and Jetset programs are widely used because of their ability to offer multiparticle production in collisions between elementary particles. These two programs are now merged under the Pythia header from version 6.1 onwards, although they were originally conceived separately.

Pythia can generate more than 200 different subprocesses. Some components of the program are aspects not necessarily covered by standard theory but they do represent original research. Pythia can simulate a variety of physics aspects such as hard and soft interactions, initial- and final-state radiation, multiple interactions, fragmentation and decays. **Pythia version 6.203** is used for this thesis.

*PythiaModule Algorithm* of the *GeneratorModules* packages runs Pythia within the Athena framework. The module acts as an interface to the FORTRAN Pythia code and puts the events into the *Transient Store* in HepMC (an environment for storing and manipulating the output of physics event generators) format so that these data can be used later by other *Algorithms* such as AtIfast or KtJet (described later). The Pythia parameters are set using the *Job Options Service* via the *jobOptions.txt* file [29].

## 3.3 ATLFAST: A Fast Simulation Package for ATLAS

As a way of improving on simple parton-level analysis (which is the reconstruction performed directly from the output of Pythia), particle level simulation (fast simulation) is an alternative to full detector simulation, which is usually

CPU-consuming. However it is quite common for physicists to require a high statistical sample of background processes at the LHC and these samples need to be generated quickly. This is where fast simulation seems to be the preferred solution because, even though it is not as accurate as the full detector simulation, it gives much closer results than parton-level simulation.

This section gives an overview of the fast simulation package for ATLAS, together with the organisation of the package and other important physics aspects of the package such as jet reconstruction, isolated particles, etc .

### 3.3.1 Athena-Atlfast overview

Athena-Atlfast is the ATLAS fast simulation package used to analyse fully generated events by performing reconstruction algorithms on four-vectors representing particles. The algorithm is a C++ object oriented implementation of the ATLAS fast simulation package, running in the Athena framework.

The aim of the package is to reproduce as accurately as possible the results obtained from the full detector simulation, where the detector response is modelled using the GEANT package [30]. This is achieved by tuning the detector-dependent parameters to the expected performance of the ATLAS detector from full detector simulation and reconstruction. A number of reconstructed quantities have been calculated using the simulated detector response for use in subsequent physics analysis. These quantities include jets and isolated electrons among others.

Detailed studies were done for the  $WH$ ,  $H \rightarrow b\bar{b}$  and  $A \rightarrow \tau\tau$  channels in order to make a comparison between full and fast simulation, in terms of selection cuts acceptances, jet reconstruction efficiencies and reconstruction efficiency. There was good agreement between fast and full simulation [31].

Not all detector effects can be readily parametrised in fast simulation. Hence,

only the basic information about the detector geometry is used by Athena-Atlfast. This can be the  $\eta$ -coverage for physics, and for the calorimetry, this can be: the size of the barrel/end-cap transition region for the electromagnetic calorimeter, and the granularity of the calorimeters. Effects related to the detailed shapes of particle showers in the calorimeters, the charged track multiplicity in jets, etc., are not considered [32].

The main aim of Athena-Atlfast is to attempt to simulate and fully analyse the generated events and select isolated leptons and photons, reconstruct jets and estimate the missing transverse energy. An accurate parametrisation of photon, electron and muon momentum resolution is included, as well as the parametrisation of the hadronic calorimeter energy resolution and the effect of the ATLAS magnetic field on jet reconstruction. Separate parametrisations of the energy resolutions for muon, electron and pion tracks provide the reconstruction of helix track parameters in the Inner Detector [32].

For this thesis, **Atlfast-01-00-59** is used for the detector simulation and reconstruction.

### 3.3.2 Organisation of Athena-Atlfast package

The organisation of the Athena-Atlfast package has greatly evolved during its development. From now onwards, the term Atlfast is used to refer to Athena-Atlfast. Atlfast is made up of the following packages:

- AtlfastAlgs
- AtlfastEvent
- AtlfastUtils
- AtlfastAnalysis
- AtlfastExamples

- TestAtlfast

The main packages for Athena-Atlfast are *AtlfastAlgs* and *AtlfastEvents*. These Atlfast packages have important functions, some of which are to [33]:

- contain all the core of Atlfast code. All algorithms required to run Atlfast are found in a specific package called *AtlfastAlgs*. The latter consists of algorithms such as *Atlfast::CellMaker*, used to read Monte Carlo information and then run a calorimeter simulation of their energy deposits. Another example of an algorithm used is *Atlfast::Isolator* to test particles for isolation.
- contain utility classes used by some of the Atlfast algorithms but which bear little or no dependence on other Atlfast objects.
- consist of a very simple package made up of two algorithms, designed to be used as examples on how to write one's own algorithms.

*AtlfastEvent* contains all the *Data Objects* produced by *AtlfastAlgs*, some of which are cells, clusters, jets, tracks and reconstructed particles. The output objects are stored in the *Transient Data Store*. The user can then use some *Algorithms* to produce information about all the Atlfast output entities in terms of ntuples (an ntuple being a standard way of storing large quantities of events, where each event may contain several variables such as momentum and energy). These algorithms can be used to produce either HBOOK or ROOT files. Section 3.4 provides an explanation of HBOOK and ROOT. ROOT files are used for this analysis. Figure 3.2 shows the sequence in which Algorithms in *AtlfastAlgs* are executed. These Algorithms in Atlfast are Athena-Algorithms.

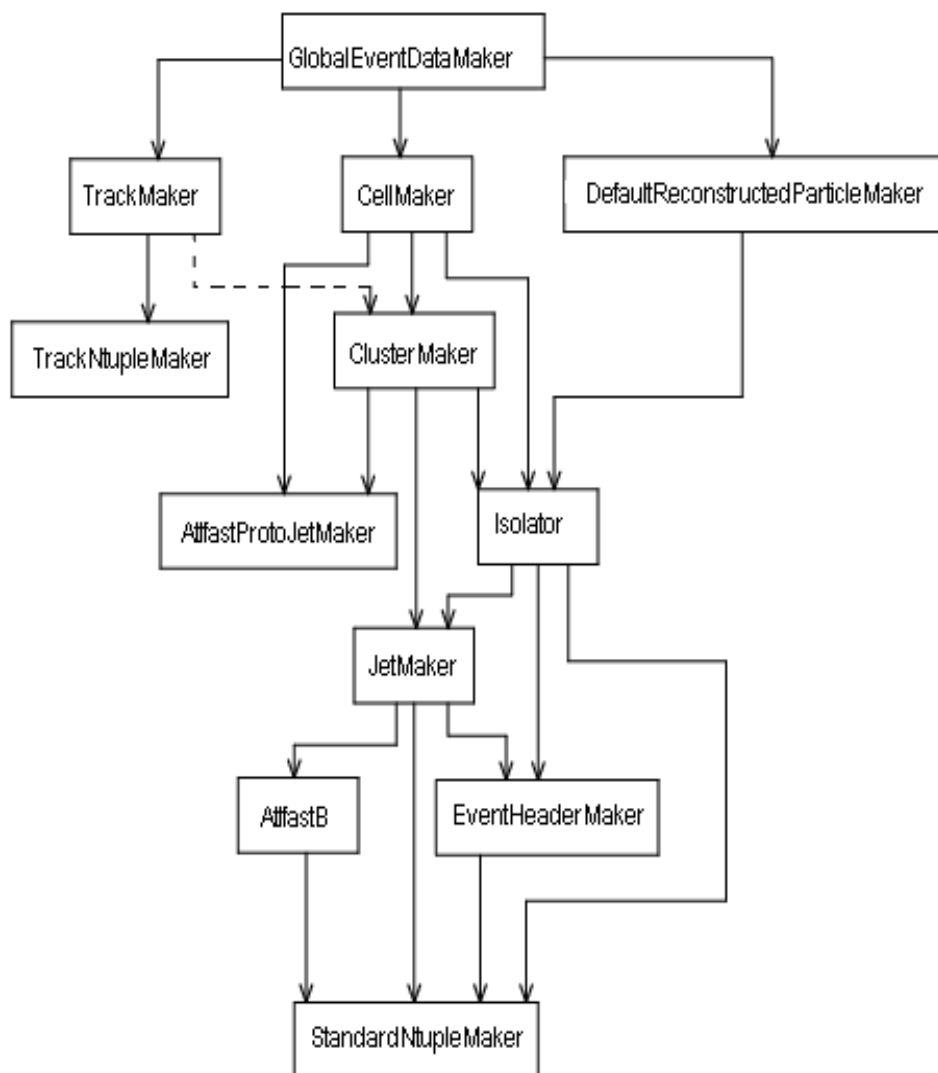


Figure 3.2: The Atfast Algorithm execution sequence. Taken from [33].

### 3.3.3 Calorimetric clusters

Atfast defines a calorimeter as a grid of cells in  $\eta \times \phi$  space. The transverse energies of particles that did not decay, apart from neutrinos, muons and SUSY LSP (Lightest Supersymmetric Particle), are summed up in calorimeter cells of a given granularity in  $\eta \times \phi$  coordinates over the full calorimeter coverage, the

default value being  $|\eta| < 5$ . For  $|\eta| < 3$ , the default granularity is  $0.1 \times 0.1$  and  $0.2 \times 0.2$  for  $|\eta| > 3$ . Note that the term default is used to denote that when Atlfast is installed by the user, the values are set to the default ones although the user can easily change them for his/her analysis.) Each particle that reaches the calorimeter then deposits all of its energy in the cell it reaches. Thus the sum of the energies of all particles hitting the cell constitutes the energy in a cell [32]. The effect due to the 2 T solenoidal magnetic field on the  $\phi$ -position of charged particles with  $p_T$  above the default 0.5 GeV threshold is parametrised, i.e., contributions coming from charged particles below this threshold value are ignored [32].

The Atlfast cluster algorithm described below is the cone algorithm, being that it is the default one. Atlfast, however, allows the user to choose between several other algorithms such as Mulguisin [34] algorithm and  $k_T$ -algorithm [35]. For this thesis, the cone algorithm and the  $k_T$ -algorithm are used. The package for the  $k_T$ -algorithm used in this thesis does not form part of Atlfast. “It is designed to run stand alone and to be used by any High energy Physics experiment where clustering of objects into jets is required” [36]. A brief description of the  $k_T$ -algorithm is given in section 3.3.8. A summary of the cone algorithm within Atlfast follows.

All calorimeter cells having a transverse energy greater than the default  $E_T > 1.5$  GeV are used as initiators of clusters, called seed cells. These are sorted in order of decreasing  $E_T$  to check whether the total  $E_T$  summed over all cells in a cone,  $\Delta R = \sqrt{(\Delta\eta)^2 + (\Delta\phi)^2}$ , exceeds the reconstructed cluster threshold energy (default:  $E_T > 10$  GeV). If this happens to be the case, Atlfast defines the set of cells within  $\Delta R$  as a cluster and gets rid of all cells within it from its list of seed cells.

No energy smearing is applied to the clusters yet as some of them are photon or electron clusters. The energy smearing is applied only when the clusters have

been identified [29].

### 3.3.4 Isolated particles

Atlfast identifies the final state particles with  $|\eta| < 2.5$  in order to create reconstructed particles such as  $\gamma$ ,  $e^\pm$  or  $\mu^\pm$ . For an electron or a photon, Atlfast creates a reconstructed particle only if the particle has  $p_T > 5.0$  GeV while a reconstructed muon requires  $p_T > 6.0$  GeV.

The photon and electron four-momenta are smeared with a Gaussian parametrisation derived from full simulation studies. The momentum of each muon track is smeared according to some resolution dependent on the muon  $p_T$ ,  $|\eta|$  and  $\phi$ . This parametrisation factor depends on which subdetector system is used for muon measurement: muon system stand-alone, Inner Detector stand-alone or combined.

These reconstructed particles can be part of a jet or isolated particles. Isolation criteria, in terms of the distance from other clusters and of maximum  $E_T$  deposition in cells in a cone around the photon/electron, are applied [29]. It should be noted that Isolation tests are done in two phases: one against clusters and the other against cells. The Atlfast algorithm starts by testing the reconstructed particles against clusters. Any cluster within  $\Delta R < 0.15$  of the reconstructed particle for photons or electrons is associated with the reconstructed particle if there are no other clusters within a radius  $0.15 < \Delta R < 0.4$  of the reconstructed particle. A reconstructed particle is defined as non-isolated if there are clusters around a cone of radius  $0.15 < \Delta R < 0.4$  of the reconstructed particle. For the case of the muon, it does not have any cluster associated with it because it does not deposit any energy in the calorimeter. A muon is defined as a non-isolated particle if there are any clusters within  $\Delta R < 0.4$  of it.

After passing cluster isolation criteria, cell isolation is performed as follows:

- The  $E_T$  of all cells within  $\Delta R < 0.2$  of the particle is summed in order to determine cell isolation. This sum is denoted as  $E_{cells}$ .
- If the reconstructed particle is an electron or photon, the transverse energy of the reconstructed particle is subtracted from  $E_{cells}$ .
- The particle is identified as isolated if the result of the subtraction is less than 10 GeV.
- The isolation of a muon is, however, different. A muon is classified as isolated only if  $E_{cells}$  within  $\Delta R < 0.2$  is less than 10 GeV.

Atfast does not take into account the efficiencies for identifying electrons, photons or muons and/or misidentifying jets. Hence the user should include the estimated efficiencies in the event analysis. For example the efficiency for a lepton identification is 90% [37]. These efficiency corrections were not applied in this thesis.

### 3.3.5 Jet reconstruction

Clustered cells are used to reconstruct jets. The energies of the clustered cells not associated with isolated electrons or photons are smeared with a Gaussian energy resolution, obtained from results of full simulation. Two options for the energy resolution can be used: low luminosity and high luminosity.

Upon calling the high luminosity option, the effect of pile-up is included in the parametrisation. This effect makes use of the shape of signals in the calorimeter cells and the average number of low  $p_T$  events [32].

A cone radius of  $\Delta R = 0.4$  is constructed around the centre of the cluster. Non-isolated muons falling within the cluster cone are added to the smeared cluster energy. If the transverse energy summed over the cone is greater than 15 GeV, the resulting cluster is labelled as a reconstructed jet.



Jets with  $|\eta| < 2.5$ , the tracking range, are labelled as b-jets (jets originating from b-quarks) if a b-quark having a  $p_T > 5$  GeV is found in a cone  $\Delta R = 0.2$  around the reconstructed jet. If similar criteria are satisfied, jets originating from c-quarks are labelled as c-jets [32].

$\tau$ -jets originate from  $\tau$ -decays and these jets can be easily identified in the case of hadronic  $\tau$ -decays. The hadronic  $\tau$ -decay products must have a  $p_T > 10$  GeV, be inside the tracking range  $|\eta| < 2.5$ , be within  $\Delta R < 0.3$  (the maximum distance from jet of taus used for the tau-tagging) and have a ratio of  $p_T^{\tau} / p_T^{\text{jets}} > 0.9$ . This ratio tags the jet as a  $\tau$ -jet.

### 3.3.6 Missing transverse energy

The missing transverse energy  $E_T^{\text{miss}}$  is calculated by summing the transverse momenta of [32]:

- isolated electrons, muons and photons;
- jets, b-jets and c-jets;
- clusters not identified as jets;
- non-isolated muons not added to any jet cluster and
- transverse energies deposited in cells not used for reconstructing clusters and above a given energy threshold, varied between 0 and 1 GeV in this work.

Transverse energies deposited in unused cells are smeared with the energy resolution used for jets. If the high luminosity option is used in Atlfast, pile-up is included in the smearing parametrisation for energy deposited in unused cells. The net transverse energy and momentum are both zero. So the total transverse

energy,  $E_T^{obs}$  (*obs* denotes observed), is equal to  $E_T^{miss}$  and the transverse momentum components  $p_x^{miss} = -p_x^{obs}$ ,  $p_y^{miss} = -p_y^{obs}$ .

### 3.3.7 Other Athena Algorithms

As seen in Figure 3.2, Atlfast contains the following algorithms:

- AtlfastB
- AtlfastProtoJetMaker
- CellMaker
- ClusterMaker
- DefaultReconstructedParticleMaker
- EventHeaderMaker
- GlobalEventDataMaker
- Isolator
- JetMaker
- StandardNtupleMaker
- TrackMaker
- TrackNtupleMaker

For the analysis presented in this thesis, Algorithms such as AtlfastB or AtlfastProtoJetMaker, DefaultReconstructedParticleMaker, TrackMaker and TrackNtupleMaker are not used. Reference [33] gives a description of these algorithms.

### 3.3.8 $K_T$ algorithm

In cone-type algorithms, jets are defined by maximising the amount of energy covered by cones of fixed size. This is different for clustering algorithms, where particles are assigned to jets iteratively according to whether a given energy-angle resolution variable  $y_{ij}$  exceeds a fixed resolution parameter  $y_{cut}$  [38]. These algorithms, unlike the cone-type ones, do not suffer from ambiguities related to overlapping cones in multijet events.

Atfast cone algorithm does not account for overlapping jets. It reconstructs the highest energy cluster first, then removes this energy from the list of available cell energies and constructs the next cluster. It often happens that the energy from one jet is assigned to the other whenever two jets overlap. This means that less energy is available to the second jet, leading to the misplacement of the centre of each jet. There are versions of the cone algorithm that take into account overlapping of jets but they still being tested and it was not possible to use this version of the cone algorithm for the thesis due to time constraints.

In addition to the cone algorithm, the  $k_T$  algorithm is used for this thesis. The **KtJet** package is used for the analysis presented in the next chapters. It is a C++ implementation of the  $k_T$  algorithm, which closely follows the features available in the FORTRAN version. There are two modes of operation of the  $k_T$  algorithm: inclusive mode and exclusive mode. The difference between these two modes lies in the way the hard final state jets are defined. Reference [39] describes in detail the difference between the two modes but for this analysis, the inclusive mode is used.

The  $k_T$  algorithm assigns a particle to the jet nearest in angle. A final state object  $k$  (this can be partons, hadrons, calorimeter cells, etc.) is defined. Then two resolution variables are computed for each final state object. The first one called  $d_{kB}$  is the squared relative transverse momentum of the object with respect to the beam direction in the small angle limit:

$$d_{kB} \approx E_k^2 \theta_{kB}^2 \quad (3.1)$$

The other parameter,  $d_{kl}$ , is the squared relative transverse momentum of object  $k$  with respect to the closest other object,  $l$ :

$$d_{kl} \approx \min(E_k^2, E_l^2) \theta_{kl}^2 \quad (3.2)$$

$d_{kB}$  is scaled by a dimensionless parameter  $R$ , which plays a radius-like role in defining the extent of jets:

$$d_k = d_{kB} R^2 \quad (3.3)$$

$R$  is analogous to the cone radius in the cone algorithm. If  $d_{kl} < d_k$ , the objects  $k$  and  $l$  are combined to give a single object with momentum  $p_{kl}$ . However if  $d_{kl} > d_k$ , object  $k$  is taken to be a jet and is removed from the list of objects to be merged. The above procedures are repeated until all objects have been included in jets [39].

After forming jets from the hadronic final state, the structure of the jets themselves can be investigated. This is known as subjet analysis and will be used as part of the analysis here. A description of the subjet analysis is given in chapter 4.

### 3.4 Analysis Parameters

The set of Atlfast parameters used in this thesis are shown in Table 3.1. The outputs from Atlfast are stored as HBOOK ntuples containing information on reconstructed quantities such as jets and isolated electrons and are later converted to

ROOT files, ROOT being a very commonly used C++ based analysis package in High Energy Physics.

For this thesis, the outputs for smeared and unsmeared simulations are performed in order to compare the effects of detector smearing. The smeared results include effects due to underlying event, detector smearing and pile-up, while the unsmeared results contain the effect arising from the underlying event only. An **underlying event** consists of all event activity except the two outgoing hard scattered jets coming from hadronic events containing jets. Examining high-energy hadron-hadron collisions, one finds events in which a hard parton-parton scatter results in large transverse momentum outgoing partons that manifest themselves as jets.

As seen in Table 3.1, a calorimeter cell energy threshold is applied in Atlfast. Cells with a transverse energy below the cell energy threshold are not registered by the calorimeter. The energy of that cell is set to zero. This threshold can be very effective in real detectors because it eliminates energy pile-up and noise in the detector. For the work presented in this thesis, various energy thresholds are applied to see what difference these have on the output. This explains the range of cell threshold used in Table 3.1.

Table 3.1: Atlfast parameters.

Parameter	Value
Electron $p_T^{min}$	5.0 GeV
Muon $p_T^{min}$	6.0 GeV
Photon $p_T^{min}$	5 GeV
Cluster $E_T^{min}$	5.0 GeV
Jet $p_T^{min}$	10 GeV
$\Delta R_{jet}$	0.4
b-quark jet $p_T^{min}$	5.0 GeV
c-quark jet $p_T^{min}$	5.0 GeV
$\tau$ -jet $p_T^{min}$	10.0 GeV
Cell threshold $E_m$	variable (0-1.0 GeV)
Integrated luminosity	100 fb <sup>-1</sup>
Magnetic field	2 T

# Chapter 4

## WW Scattering Studies

This chapter presents a detailed study of  $WW$  scattering at the Large Hadron Collider (LHC) for the case that no new particles are discovered before the start of the LHC. It is an extension of the work presented in [7]. The analysis presented in this chapter is done using **smeared** events.

It is likely that new physics will manifest itself in or below the TeV region and that the LHC will be able to examine this new physics in great detail [7]. Data collected at LEP, SLC and the Tevatron seem to suggest that this new physics should be a Higgs boson with a mass of less than around 200 GeV [40]. Such a limit on the mass of the Higgs is model dependent and it is possible that no light scalar particle exists at all [7]. It is therefore vital to reconsider the indirect constraints on the mass of the Higgs boson,  $M_H$ , which parametrise the lack of understanding of the electroweak symmetry breaking sector in the Minimal Standard Model (MSM) [41].

If the MSM is regarded as an effective theory of some more fundamental theory which explains the origin of electroweak symmetry breaking, then the energy scale,  $\Lambda$ , of such a fundamental theory provides a scale of new physics for the Standard Model [42]. Theoretical considerations are the only way of putting a limit on  $M_H$  and  $\Lambda$  due to the absence of experimental evidence. Choosing a

particular value for the energy scale  $\Lambda$  means that a certain range of Higgs mass is allowed. Thus one can predict  $M_H$  given a framework. However, there is nothing special about the Higgs scalar and this thesis deals with a model independent treatment of physics by using a model that is **not** the SM and a model that does **not** contain any Higgs.

This chapter is organised as follows. In the sections that follow, the electroweak chiral lagrangian, unitarisation to predict resonances for the  $WW$  signal and parton-level predictions for  $WW$  production cross-section are discussed. Then the signal and background processes are discussed and various cuts are used to effectively reduce the background events.

## 4.1 Framework

The enhanced production of longitudinal vector boson pairs ( $V_L V_L$ ) at high energy colliders such as the LHC is promising because studies done [43] show that the data is consistent with the strongly interacting symmetry breaking sector (SBS). At low energies, all the effects due to electroweak symmetry breaking can be described by a gauge invariant chiral Lagrangian, in which the higher-dimensional operators are suppressed by  $\Lambda$ .

The Electroweak Chiral Lagrangian (EChL) describes the low energy effects of different strongly interacting SBS models. This EChL can only describe electroweak physics accurately at low energies. This is because electroweak observables are given as a truncated series in powers of external momenta and will therefore violate unitarity at high energy, in particular at the LHC due to the longitudinal gauge bosons. The perturbative EChL predictions can be extended to high energy using unitarisation methods. The unitarised amplitudes for the  $V_L V_L$  production process can reproduce resonant behaviours [43].

In the approach used in this thesis,  $\Lambda$  defines the scale of the physics respon-



sible for electroweak symmetry breaking, where an upper limit is set to the value of  $\Lambda$ . J.A.Bagger, A.F.Falk and M.Swartz have shown that the cut-off value for  $\Lambda$  is 3 TeV, based on present data without any fine tuning for  $\Lambda$  [44]. General unitarity considerations require that  $\Lambda \leq 3$  TeV.

## 4.2 Lagrangian

New physics due to electroweak gauge symmetry breaking appears in the Lagrangian, which is constructed from the Goldstone bosons  $w_a$  associated with breaking  $SU(2) \times U(1) \rightarrow U(1)$ . The scale of this new physics must be around  $\nu = 246$  GeV ( $\nu$  is the vacuum expectation value) and the degree of symmetry breaking informs us that there are three Goldstone bosons involved in the Lagrangian [7]. Any model of the electroweak symmetry breaking sector must have three Goldstone bosons involved and because of their existence, the longitudinal  $W$  and  $Z$  boson can be described by chiral Lagrangian techniques [45].

After the symmetry breaking, a residual global  $SU(2)$  symmetry is left according to experimental data. This residual global  $SU(2)$  symmetry gives a value of unity to the  $\rho$ -parameter ( $\rho = M_W^2 / (M_Z^2 \cos^2 \theta_W)$ ).  $M_W$  is the  $W$  boson mass,  $M_Z$  is the  $Z$  boson mass and  $\theta_W$  is the Weinberg angle ( $\sin^2 \theta_W = 1 - (M_W/M_Z)^2$ ). In chiral perturbation theory the residual  $SU(2)$  symmetry arises due to the breaking of a global chiral symmetry,  $SU(2)_L \times SU(2)_R$  [7]. The  $w_a$  fields are assembled into group element

$$U = \exp(i \frac{w \cdot \tau}{\nu}) \quad (4.1)$$

where  $\tau$  are the Pauli matrices. The gauged chiral Lagrangian is then built. It is written as a derivative expansion,

$$L = L^{(2)} + L^{(4)} + \dots \quad (4.2)$$

where

$$\begin{aligned} L^{(2)} &= \frac{\nu^2}{4} \langle D_\mu U D^\mu U^\dagger \rangle \\ L^{(4)} &= a_4 (\langle D_\mu U D^\nu U^\dagger \rangle)^2 + a_5 (\langle D_\mu U D^\mu U^\dagger \rangle)^2 \end{aligned} \quad (4.3)$$

Reference [7] gives a detailed treatment of the origin of these terms in the Lagrangian. The terms in  $L^{(2)}$  give rise to the  $W$  and  $Z$  masses. The terms in  $L^{(4)}$  are responsible for anomalous three- and four-gauge boson self couplings [44]. In this thesis, the focus is mainly on the quartic couplings between vector bosons.

$a_4$  and  $a_5$  are the two parameters used to categorise the new physics one is not aware of. They contain information about the physics of electroweak symmetry breaking. For example for the Standard Model with a heavy Higgs boson of a mass  $M_H$ , one gets  $a_4 = 0$  and  $a_5 = \nu^2/(8M_H^2)$  before any renormalisation. There are no strong constraints on  $a_4$  and  $a_5$  according to a study performed in Reference [46]. Therefore similar loose constraints on  $a_4$  and  $a_5$  as in [7] are taken. It is assumed that these constraints can be in the range  $[-0.01, 0.01]$  in order to find any potential new physics.

### 4.3 Unitarisation Procedure

The scattering amplitudes of longitudinally polarised vector bosons ( $V_L$ ) can be approximated by the scattering of the Goldstone bosons  $w_a$  [45]. This thesis will be dealing with strongly-interacting longitudinal  $W$ s in the TeV region, meaning that  $SU(2)$  isospin is conserved. Isospin indices are assigned as follows:

$$W_L^a W_L^b \rightarrow W_L^c W_L^d \quad (4.4)$$

Thus,  $W_L W_L$  scattering amplitudes can be written in terms of isospin indices:

$$\mathcal{M}(W_L^a W_L^b \rightarrow W_L^c W_L^d) = A(s, t, u) \delta^{ab} \delta^{cd} + A(t, s, u) \delta^{ac} \delta^{bd} + A(u, t, s) \delta^{ad} \delta^{bc}, \quad (4.5)$$

where  $a, b, c, d = 1, 2, 3$ , and  $s, t$  and  $u$  are the usual Mandelstam variables. The definitions of these variables can be found in Appendix A. The amplitude function  $A$  contains all the information about the  $W_L W_L$  scattering process. Note that the term  $W_L$  refers to either  $W_L^\pm$  or  $Z_L$ .

It is quite common to project the amplitudes onto partial waves,  $a_{IJ}$ , with definite angular momentum  $J$  and weak isospin  $I$  as:

$$a_{IJ}(s) = \frac{1}{64\pi} \int_{-1}^1 d(\cos \theta) P_J(\cos \theta) A_I(s, t, u) \quad (4.6)$$

where  $\theta$  is the centre-of-mass scattering angle. The values of the isospin depend on the process being studied. For this thesis, it is the  $WW$  scattering process and  $I = 0, 1, 2$ . Bose symmetry means that for  $I = 0, 2$  only even values of  $J$  are allowed while for  $I = 1$ , odd values of  $J$  are allowed. Therefore, higher order partial waves from the above partial wave equation can be neglected because they are numerically small [7].

The isospin amplitudes  $A$  can be derived by using [45]:

$$\begin{aligned} A_0(s, t, u) &= 3A(s, t, u) + A(t, s, u) + A(u, t, s) \\ A_1(s, t, u) &= A(t, s, u) - A(u, t, s) \\ A_2(s, t, u) &= A(t, s, u) + A(u, t, s) \end{aligned} \quad (4.7)$$

and

$$A_I(s, t, u) = 32\pi \sum_{J=0}^{\infty} (2J+1) a_{IJ} P_J(\cos\theta) \quad (4.8)$$

The amplitudes can be written as [7]:

$$\begin{aligned} A_0(s, t, u) &= 32\pi a_{00} \\ A_1(s, t, u) &= 32\pi 3a_{11} \cos\theta \\ A_2(s, t, u) &= 32\pi a_{20} \end{aligned} \quad (4.9)$$

The amplitudes for the different combinations of  $W_L W_L$  scattering are [7]:

$$\begin{aligned} A(W_L^+ W_L^- \rightarrow W_L^+ W_L^-) &= \frac{1}{3} A_0 + \frac{1}{2} A_1 + \frac{1}{6} A_2 \\ A(W_L^+ W_L^- \rightarrow Z_L Z_L) &= \frac{1}{3} A_0 - \frac{1}{3} A_2 \\ A(ZZ \rightarrow ZZ) &= \frac{1}{3} A_0 + \frac{2}{3} A_2 \\ A(WZ \rightarrow WZ) &= \frac{1}{2} A_1 + \frac{1}{2} A_2 \\ A(W_L^\pm W_L^\pm \rightarrow W_L^\pm W_L^\pm) &= A_2 \end{aligned} \quad (4.10)$$

The amplitudes of the elastic  $W_L W_L$  scattering processes can be unitarised using the Inverse Amplitude Method (IAM). Reference [43] describes this in more detail. Because of unitarisation, the partial waves develop resonances to satisfy unitarity conditions. Resonances are observed when the corresponding phase shift passes through  $\pi/2$  [7]. Figure 4.1 gives a map of the  $a_4$ - $a_5$  parameter space as determined by the IAM.

The region below the dotted line in the parameter space is forbidden because it violates causality. This occurs whenever there is a phase shift of  $-\pi/2$ . There is also a region where no resonance occurs and it is labelled as E. The renormalisation scale  $\mu$  is taken to be 1 TeV. The region in the parameter space map is defined such that it contains a resonance with a mass below 2 TeV [7].

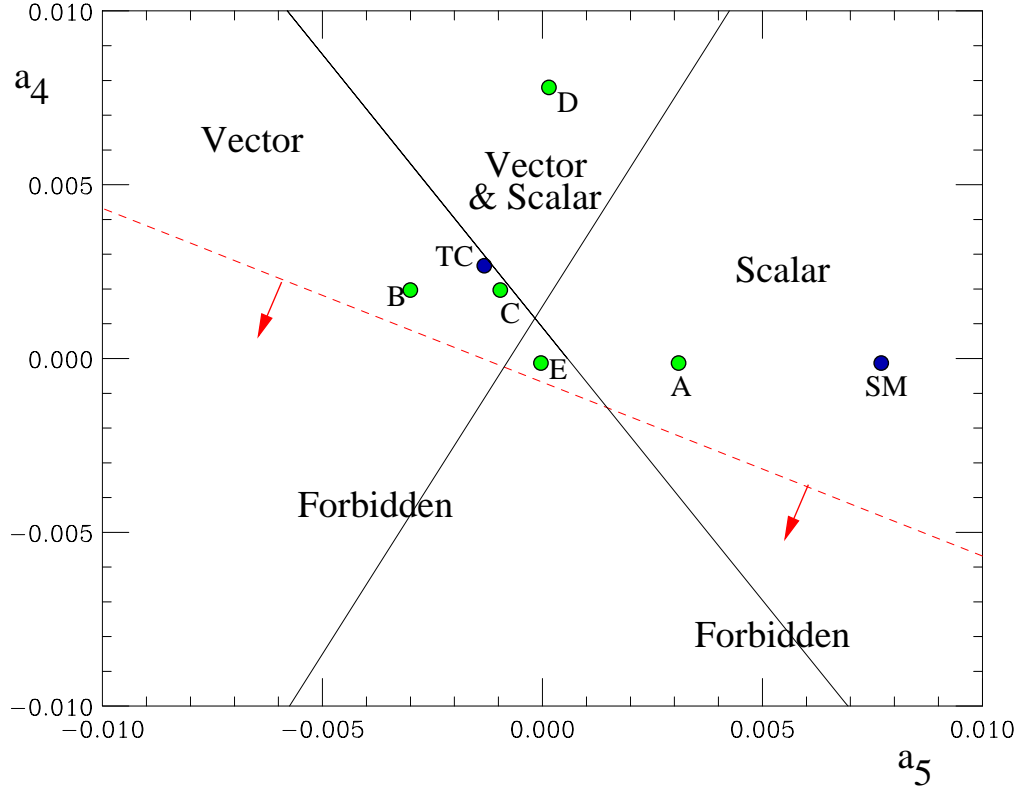


Figure 4.1: Parameter space map as determined from IAM. Taken from [7].

## 4.4 Parton-Level Cross-Sections

Table 4.1 shows the choice of the 5 different parameters that give rise to 5 different scenarios for the process  $pp \rightarrow W^+W^-jj + X$  at a centre-of-mass of 14 TeV, where  $j$  denotes a jet. The choice of these parameters leads to a 1 TeV scalar (scenario A), a 1.4 TeV vector (scenario B), a 1.9 TeV vector (scenario C), a 800 GeV scalar and 1.4 TeV vector (scenario D) and a no resonance scenario (scenario E). These scenarios are the green points labelled A-E in Figure 4.1.

The parton-level cross-sections for the five scenarios are shown in Figures 4.2-4.6. Fig. 4.2, 4.3 and 4.4 have got a resonance while Fig. 4.5 has two resonances. Fig. 4.6 has no resonance at all. These plots are consistent with the choice of the five different parameters of  $a_4$  and  $a_5$ .

Table 4.1: Parameters for the 5 different scenarios.

Scenario	$a_4$ (1 TeV)	$a_5$ (1 TeV)
A	0.0	0.003
B	0.002	-0.003
C	0.002	-0.001
D	0.008	0
E	0	0

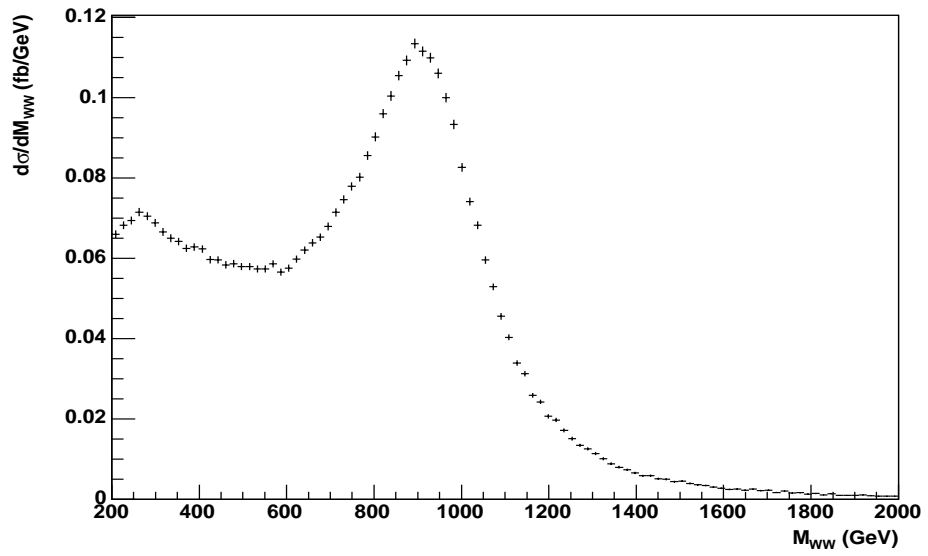


Figure 4.2: Partonic cross-section for scenario A.

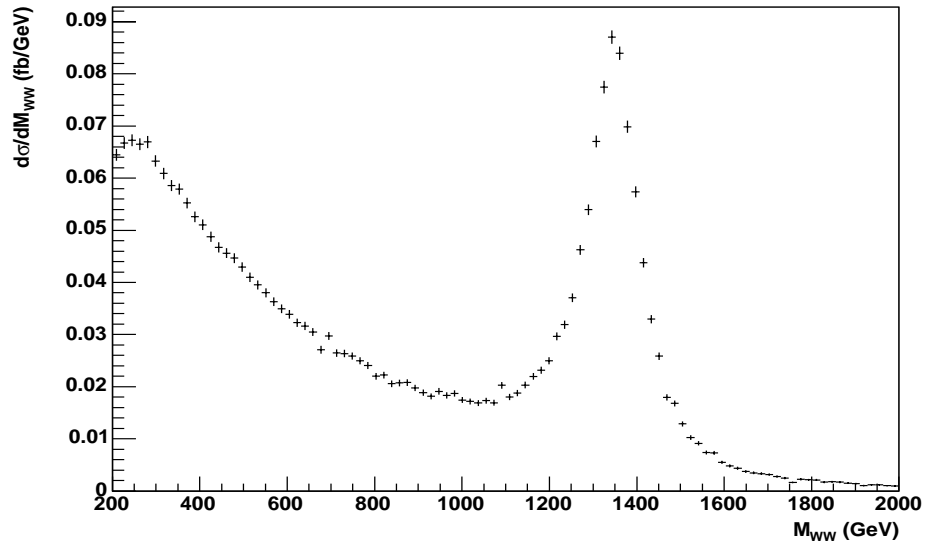


Figure 4.3: Partonic cross-section for scenario B.

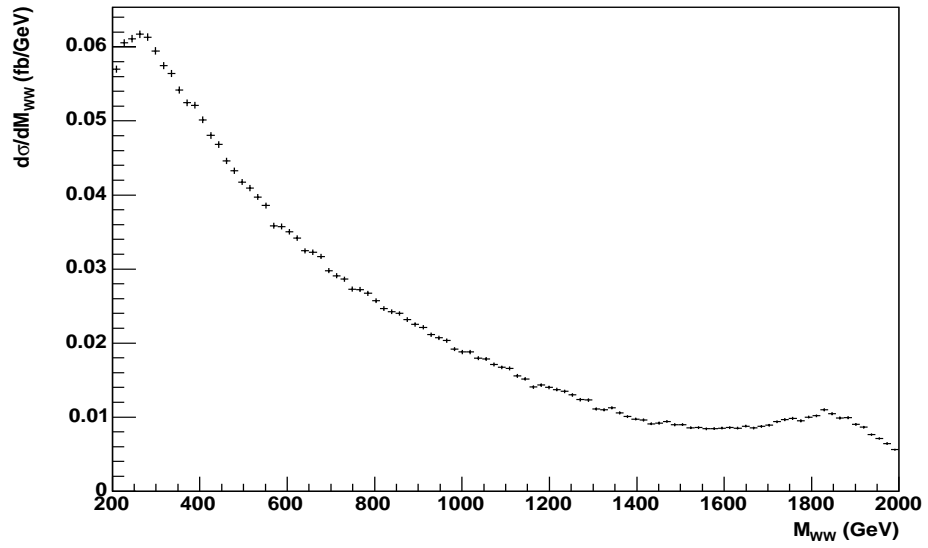


Figure 4.4: Partonic cross-section for scenario C.

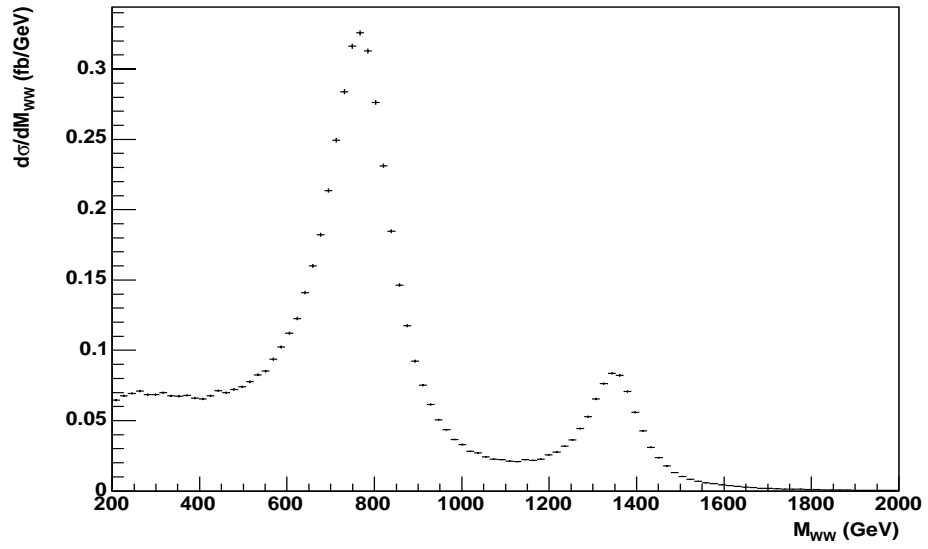


Figure 4.5: Partonic cross-section for scenario D.

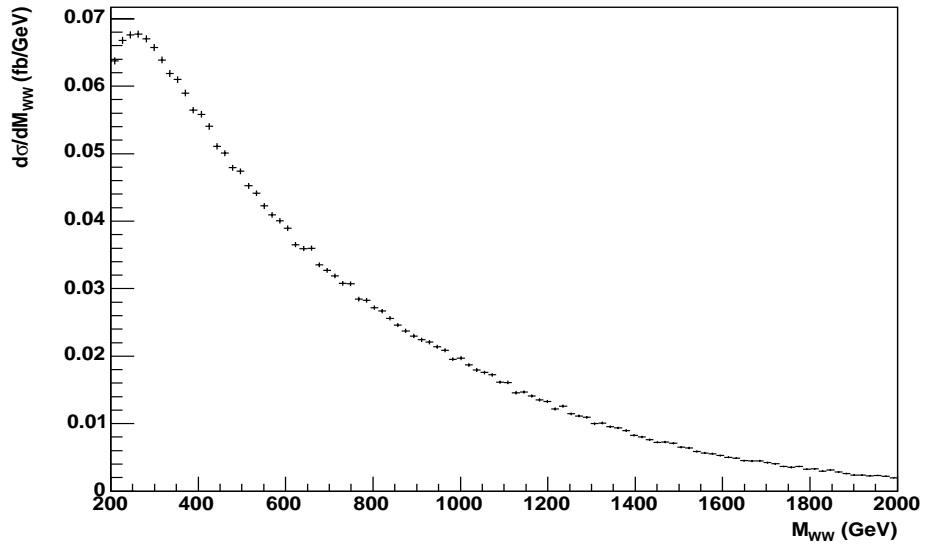


Figure 4.6: Partonic cross-section for scenario E.



## 4.5 Signal and Background Processes

The diagrams for the signal and background processes are illustrated in Figure 4.7. The signal is the scattering of  $WW$  and it has a large enough rate to be able to be observed at low luminosity operation. It is usual to focus on leptonic decay modes of gauge bosons because it is the cleanest way to detect them at hadron colliders [43] in order to reduce backgrounds. This thesis however focuses on semileptonic final states, i.e, where one  $W$  decays leptonically and the other  $W$  decays hadronically. This is because the leptonic decay mode  $W \rightarrow l\nu$  has a low branching ratio. The hadronic decay mode of the  $W \rightarrow jj$  is quite messy but has the advantage of having a high branching ratio.

A few main characteristics of the signal are [6]:

- large missing transverse energy because of neutrino arising from  $W \rightarrow l\nu$ .
- 2 high- $p_T$  jets from the  $W \rightarrow jj$  decay, close in  $\eta$ - $\phi$  space,  $\Delta R$ .
- a high- $p_T$  central lepton.

QCD  $t\bar{t}$  production and radiative  $W$ +jets are the dominant backgrounds, having some similarities to the  $WW$  signal. The  $t\bar{t} \rightarrow l\nu jj b\bar{b}$  background contains a real  $W \rightarrow jj$  in addition to a hadronic activity from the  $b$ -jets when they fall in the central region. The  $W$ +jets background is possibly the largest one, containing two jets [47] with invariant mass close to  $M_W$ . One of the  $W$ s (not shown in Figure 4.7(b)) comes from the quark which fakes a  $W$  by becoming a jet or jets. Although the probability for this is quite low, the process does have an appreciable contribution to the background due to the large  $W$ +jets production cross-section. The  $W$ +jets background however suffers from significant theoretical uncertainties [6].

The Pythia Monte Carlo generator is modified to include the EChL approach using the Inverse Amplitude Method approach of unitarisation. Pythia **6.203** is

used to generate the signal and background events. Pythia itself is implemented in **Atlfast-01-00-59** used for the analysis in this thesis. The cross-sections of the processes can be found in Table 4.2. The minimum  $p_T$  of hard scatter is set to 250 GeV for the  $W$ +jets and to 300 GeV for the  $t\bar{t}$  [7]. This is done in order to improve the generation efficiency. The effects due to underlying events and pile-up from multiple  $pp$  interactions are also simulated in both the signal and background events.

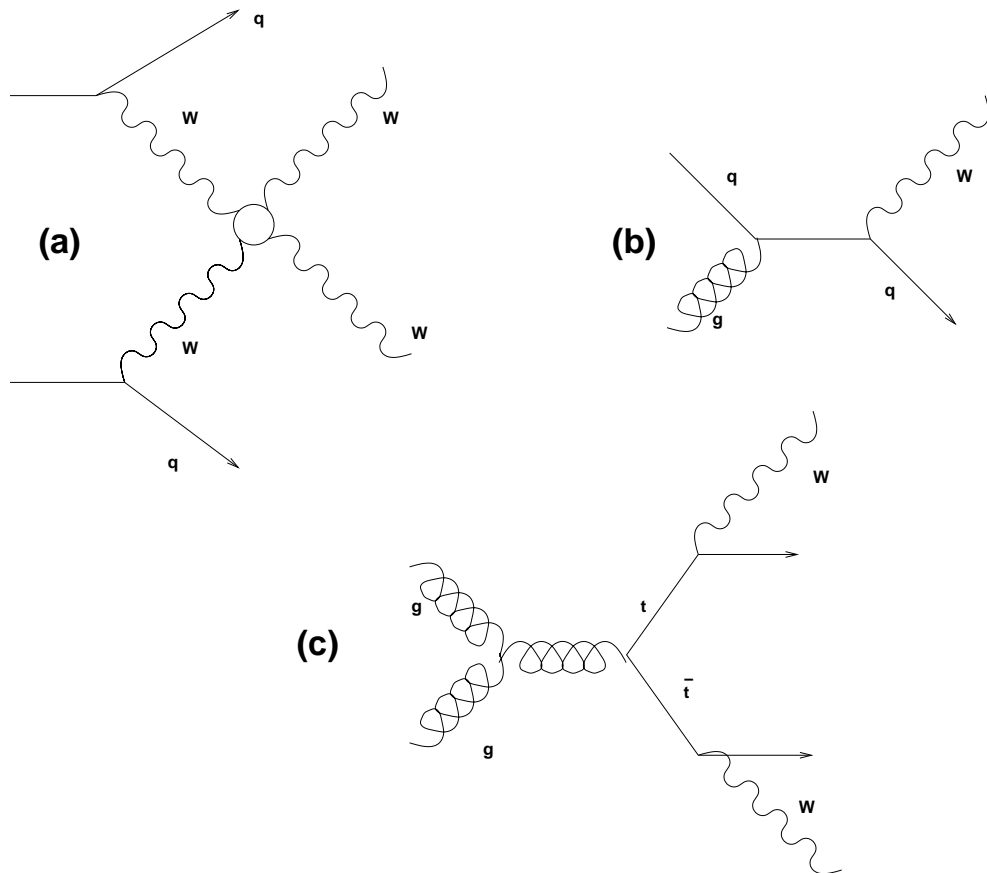


Figure 4.7: Feynman diagrams for signal and backgrounds: (a) signal; (b)  $W$ +jets; One of the  $W$ s (not shown in Figure 4.7(b)) comes from the quark which fakes a  $W$  by becoming a jet or jets; (c)  $t\bar{t}$

A series of cuts optimised exclusively in terms of the statistical significance of

the signal above the backgrounds is applied to reject events. These cuts follow from some characteristics typical of the background processes. The cuts applied in this thesis were first used in [7].

Before describing the cuts in more detail, it should be noted that a preliminary study was done to find out the value of the optimum  $k_T$   $R$ -parameter used to reconstruct the jets, together with the optimum cone radius  $R$  for the cone algorithm. These are described in chapter 5. The  $k_T$  algorithm is used for the study in this chapter because it allows us to perform subjet analysis. Later in chapter 5 an evaluation of performing the subjet analysis as far as reducing the background is made. This is done by repeating the whole analysis of this chapter but by making use of the cone algorithm instead.

Table 4.2: Cross-sections for signal and backgrounds used to generate events in Pythia. For the background, the cross-sections are in the restricted kinematic range given on p.90.

<b>Signal</b>	<b>Cross-section (fb)</b>
1 TeV scalar (A)	75
1.4 TeV vector (B)	52.5
1.9 TeV vector (C)	44.0
Scalar and vector (D)	117.9
Continuum (E)	44.0
<b>Background</b>	<b>Cross-section (fb)</b>
$W$ +jets	29,290
$t\bar{t}$	15,580

## 4.6 The Signal

As mentioned in section 4.5, it is quite common to focus on leptonic decay modes of gauge bosons because it is the cleanest way to detect them at hadron colliders [43] in order to reduce backgrounds. This analysis however focuses on semileptonic final states. This is achieved by:

- selecting a leptonically decaying  $W$  (identify electron/muon and find missing transverse energy),
- then finding a hadronically decaying  $W$  (from the jets), and
- selecting some event environment, e.g. for tagging jets.

Only one signal sample is shown in the diagrams that follow because the other signals follow a similar shape. The scalar 1 TeV signal (scenario A) is used. It is vital to investigate how the cuts affect the signal to background ratio. 300,000 events were generated for the scalar 1 TeV sample, while approximately 30 million  $t\bar{t}$  events and approximately 30 million  $W$  + jets events were generated. Table 4.3 gives a summary of the number of events used for the signal and background. The statistics used for the number of events bear no physics reason. They only reflect the samples available at the time of the analysis.

### 4.6.1 Leptonic $W$

All events having no isolated electron or muon are rejected. The highest  $p_T$  lepton in each remaining event is then selected and its pseudorapidity is calculated.

The momentum of the escaping neutrino is then found, from which the leptonic  $W$  will be reconstructed. Any missing momentum in the transverse plane can be associated with the neutrino because the detector has a hermetic coverage

Table 4.3: Number of events generated for signal and backgrounds.

<b>Signal</b>	<b>Events</b>
1 TeV scalar (A)	0.3 million
1 TeV vector (B)	0.15 million
1.9 TeV vector (C)	0.6 million
Scalar and vector (D)	0.6 million
Continuum (E)	0.6 million
<b>Background</b>	<b>Events</b>
$W$ +jets	$\sim 30$ million
$t\bar{t}$	$\sim 30$ million

in this plane. However the same assumption does not hold in the beam direction because particles escape detection along the beam pipe. So the missing momenta are not necessarily those of the neutrinos.

The leptonic  $W$  mass is assumed to be 80.1 GeV and a quadratic equation for the  $z$  component of momentum is formulated (as shown in Appendix B). Note that it does not make much of a difference which value of the momentum one uses as shown in Appendix B. So out of the two solutions, the one with the higher neutrino momentum is taken at random.

The leptonic  $W$  candidate is then reconstructed by summing the four-momenta of the neutrino and the lepton with the highest  $p_T$ . Figure 4.8 shows the transverse momentum and pseudorapidity of the highest  $p_T$  lepton for both the signal and background. The  $W$ +jets have similar  $\eta$  characteristics to the signal, whereas the  $t\bar{t}$  events have more centrally-produced leptons. The missing transverse momentum of the leptonic  $W$  is also shown in Figure 4.8. The distribution is softer for the  $t\bar{t}$  events. The transverse momentum distribution of the leptonic  $W$  reconstructed from the lepton and assumed neutrino shows that the signal has a

much harder spectrum than the backgrounds. Any event with a  $p_T < 320$  GeV is rejected.

## 4.6.2 Hadronic W

For each jet out of the remaining signal and background sample, the  $p_T$  and pseudorapidity are calculated. These are shown in Figures 4.9(a) and (b). Then the jet with the highest  $p_T$  within the range  $|\eta| < 4.0$  is found and the invariant mass of that jet is calculated. The highest  $p_T$  jet is taken to be the hadronic  $W$  candidate. This is because the two quarks emerging from the hadronic  $W$  decay are so boosted that Atfast considers them to be one jet. Hence the invariant mass of this jet is assigned as the mass of the hadronic  $W$  candidate.

Figure 4.9(c) shows the mass of the hadronic  $W$  candidate. A  $W$  mass peak is visible for the signal. The  $t\bar{t}$  background also shows a  $W$  mass peak, together with a peak at around 175 GeV, which is the top mass. An event is kept if the hadronic  $W$  satisfies the following criteria:  $p_T > 320$  GeV, invariant mass between 70 and 90 GeV and  $|\eta| < 4.0$ .

The next step is to perform a subjet analysis by forcing the jet to decompose into two subjets. Extra information which can be obtained from decomposing the jet is the resolution parameter  $y_{cut}$  at which subjets are defined [39]:

$$y_{cut} = Q_0^2/E_{cut}^2. \quad (4.11)$$

where  $E_{cut}$  is chosen to be the  $p_T$  of the jet in consideration and  $Q_0$  is the relative  $p_T$  of the quarks in the jet.

If an event has a genuine  $W$  decay, the scale at which the jet is resolved into subjets (i.e.,  $y_{cut} p_T^2$ ) will be  $O(M_W^2)$ . Jets originating from a real  $W$  will have  $Q_0^2 \sim M_W^2$  but for QCD radiation, the relative  $p_T$  of the gluons are low. In fact, the

relative  $p_T$ ,  $Q_0 \ll M_W^2$ . This explains why the scale at which the jet is resolved into subjets ( $y_{cut} p_T^2 = Q_0^2$ ) is  $O(M_W^2)$  for a real  $W$ .

Figure 4.9(d) shows the  $\log(p_T \sqrt{y_{cut}})$  distribution, where it is clear that the scale of splitting is high in the signal and softer in the  $W$ +jets. For the case of the  $W$ +jets, the hadronic  $W$  is usually a QCD jet rather than a genuine  $W$ . The shape for the  $t\bar{t}$  events follows that of the signal quite closely. A cut of  $1.6 < \log(p_T \sqrt{y}) < 2.0$  is applied to reduce the  $W$ +jets background.

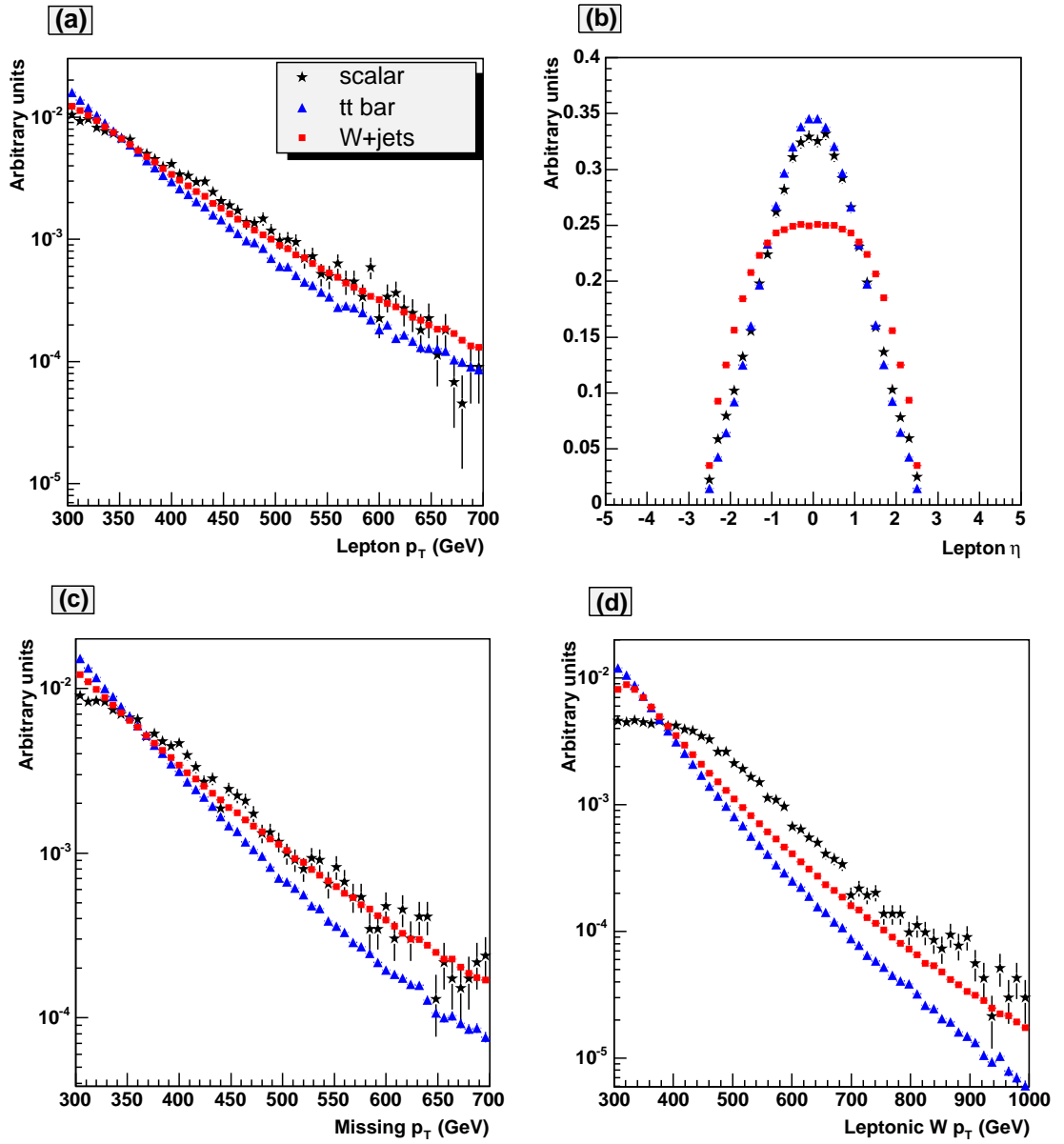


Figure 4.8: Leptonic variables: (a) transverse momentum of leptons with highest  $p_T$  in an event, (b) pseudorapidity of the lepton, (c) missing transverse momentum and (d)  $p_T$  of the leptonic  $W$  candidate.



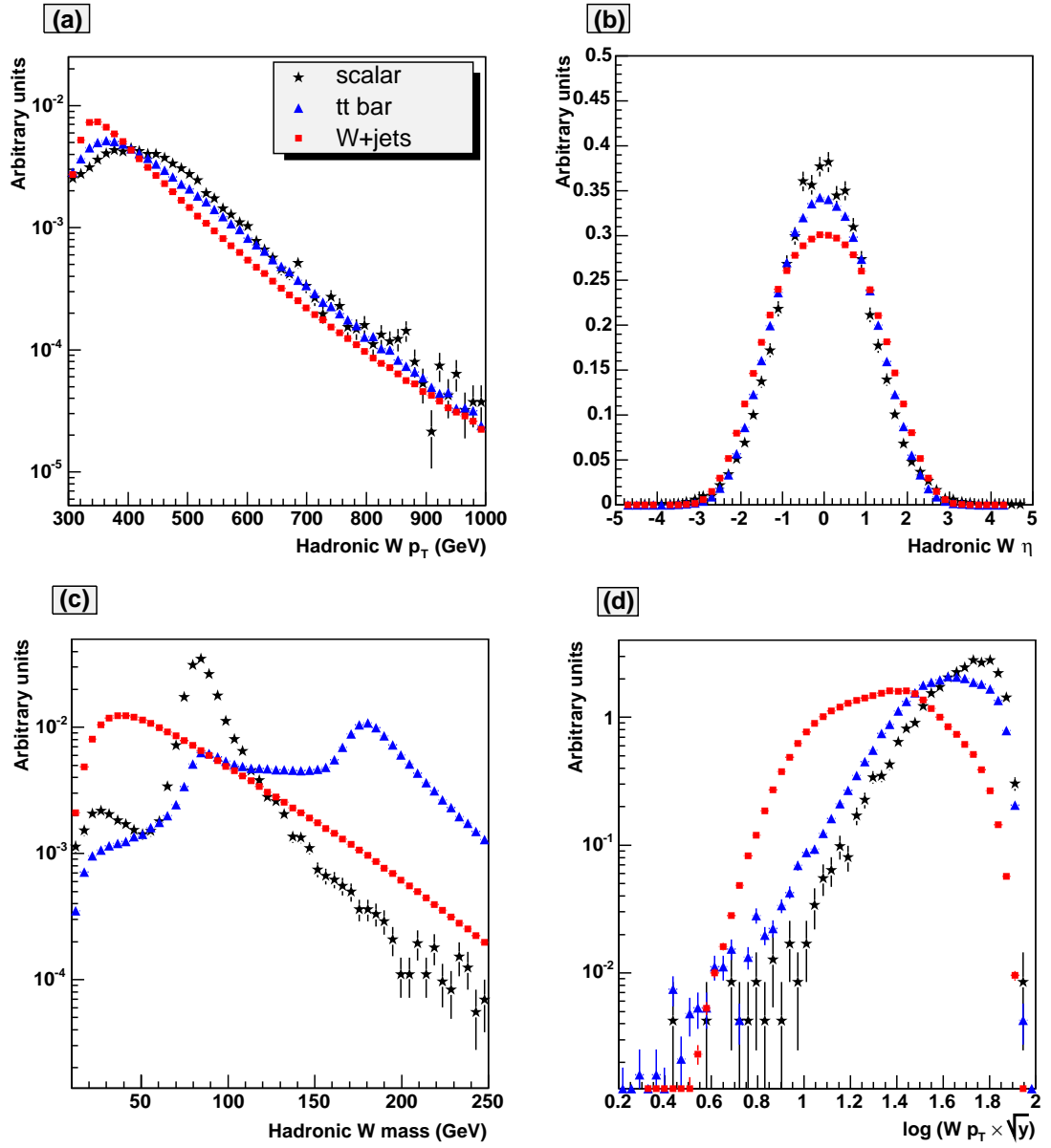


Figure 4.9: Variables for hadronic  $W$ . (a)  $p_T$ , (b) pseudorapidity, (c) invariant mass and (d)  $p_T \sqrt{|y_{cut}|}$ .

### 4.6.3 Other important cuts

A few more cuts have to be applied to further reduce backgrounds. These cuts are summarised below.

**Top quark veto** Events in the remaining  $t\bar{t}$  sample containing a genuine leptonic  $W$  will have a jet and the leptonic  $W$  giving an invariant mass close to the top quark mass. Each jet apart from the hadronic  $W$  is combined with the leptonic  $W$  candidate. The invariant mass of the jet with the leptonic  $W$  is depicted in Figure 4.10(a). The top mass peak is obvious for the  $t\bar{t}$ . A cut to get rid of the  $t\bar{t}$  events is applied. Any event with an invariant mass between 130 and 240 GeV is rejected. For the events that pass the cut, each jet is combined with the hadronic  $W$  and if its invariant mass lies in the range 130-240 GeV, the event is rejected. These cuts, which are called the “top quark veto”, are quite useful in drastically reducing the  $t\bar{t}$  background as seen in the discussion chapter 5.

**Tag jet veto** Bosons are radiated from the quarks in the initial state during the  $WW$  scattering process. This quark will give rise to a high rapidity jet. Such a jet is usually not present in the backgrounds and its presence can be used to tag the signal [7]. A tag jet is defined as follows. A forward/backward tag jet is defined as the highest  $E_T$  jet forward/backward of the most forward/backward  $W$  in terms of rapidity. Such a jet must have  $p_T > 20$  GeV. The pseudorapidity distribution of these jets is shown in Figure 4.10(b). The majority of signal events have a high absolute value of  $\eta$ , in contrast with the background. This factor is taken into account and an event is rejected if it does not have a tag jet in both the forward and backward regions satisfying:

- $p_T > 20$  GeV
- $E > 300$  GeV
- $4.5 < |\eta| < 2.0$

**Hard  $p_T$**  Figure 4.10(c) shows the transverse momentum for the  $WW$  and the two tag jets. It is obvious from the figure that the distribution for the background events is harder. This is because in the background processes extra jets from hard QCD radiation may be picked up and/or missed [7]. Using this knowledge, an event is rejected if the  $p_T$  of the  $WW +$  tag jet system is greater than 50 GeV.

**Minijet veto** For the signal, no colour is exchanged between the two quarks which emit the  $W$  bosons and the jets which are formed by the hadronically decaying  $W$  [6]. This means that there is less soft gluon radiation in the central region for the signal in comparison with the background. Soft gluon radiation due to underlying events produces the emission of minijets. Hence a cut is performed so as to reject these minijets. Minijets are defined as all jets apart from the hadronic  $W$ , having  $|\eta| < 2.0$ . A veto on these minijets would constitute a tool for isolating the scattering signal. Figure 4.10(d) shows the number of minijets satisfying the underlined characteristics. An event is rejected if there is more than one minijet with  $p_T > 15$  GeV.

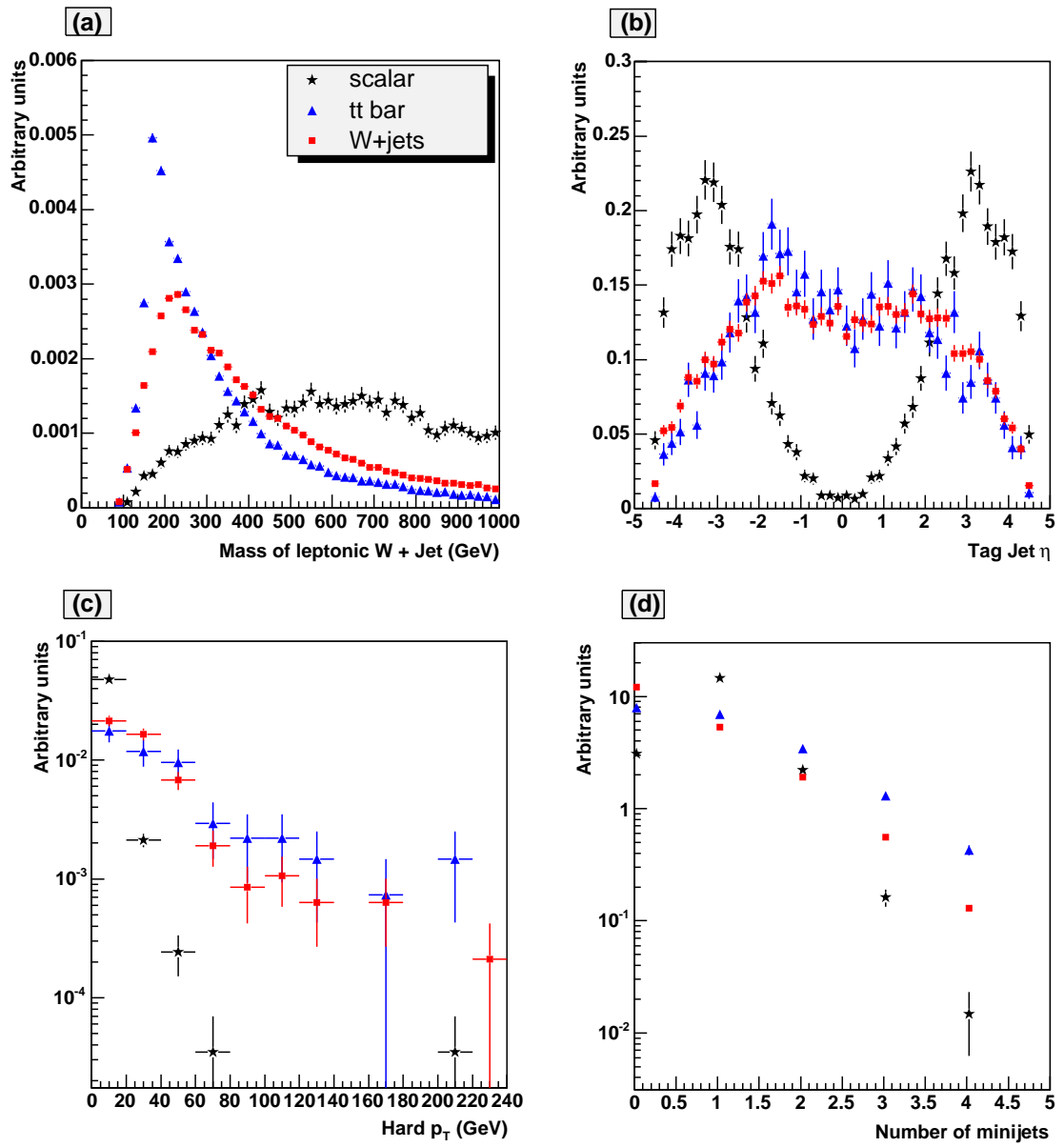


Figure 4.10: (a) Mass distribution of leptonic  $W$  and jet other than the hadronic  $W$  candidate, (b) pseudorapidity of tag jets, (c)  $p_T$  for  $WW$  + tag jets system and (d) number of minijets.

# Chapter 5

## Discussion

This chapter shows the reconstructed  $WW$  mass and the effects of cuts on the signal and background. It provides a summary of the results obtained by using the cone algorithm and the  $k_T$  algorithm for jet reconstruction. All analysis in this thesis uses smeared events except for section 5.3 where a comparison between smeared and unsmeared events is made. Finally, the effects of energy threshold,  $R$ -parameter and cone radius on the mass of the hadronic  $W$  are investigated.

### 5.1 Reconstructed $WW$ Mass

After applying all the cuts described in chapter 4, one can finally reconstruct the  $WW$  mass as shown in Figure 5.1(a) and (b). These show the mass distributions for the five different scenarios of the signal, and the background. As seen the background is very low and resonance peaks for some of the signals can be seen. For example scenario A (1 TeV scalar sample) gives a peak at around 1.0 TeV while scenario D (double resonance sample) gives two peaks, one at around 0.8 TeV and the other at around 1.4 TeV.

The angular distribution of the scattered  $WW$  in the  $WW$  centre-of-mass frame provides a good way of distinguishing between scalar and vector resonances.

Figures 5.2(a) and (b) show the distribution of  $|\cos\theta|$ , where  $\theta$  is the angle between the incoming  $W$  and the scattered  $W$  direction. Note that  $\theta$  is calculated in the  $WW$  centre-of-mass frame.

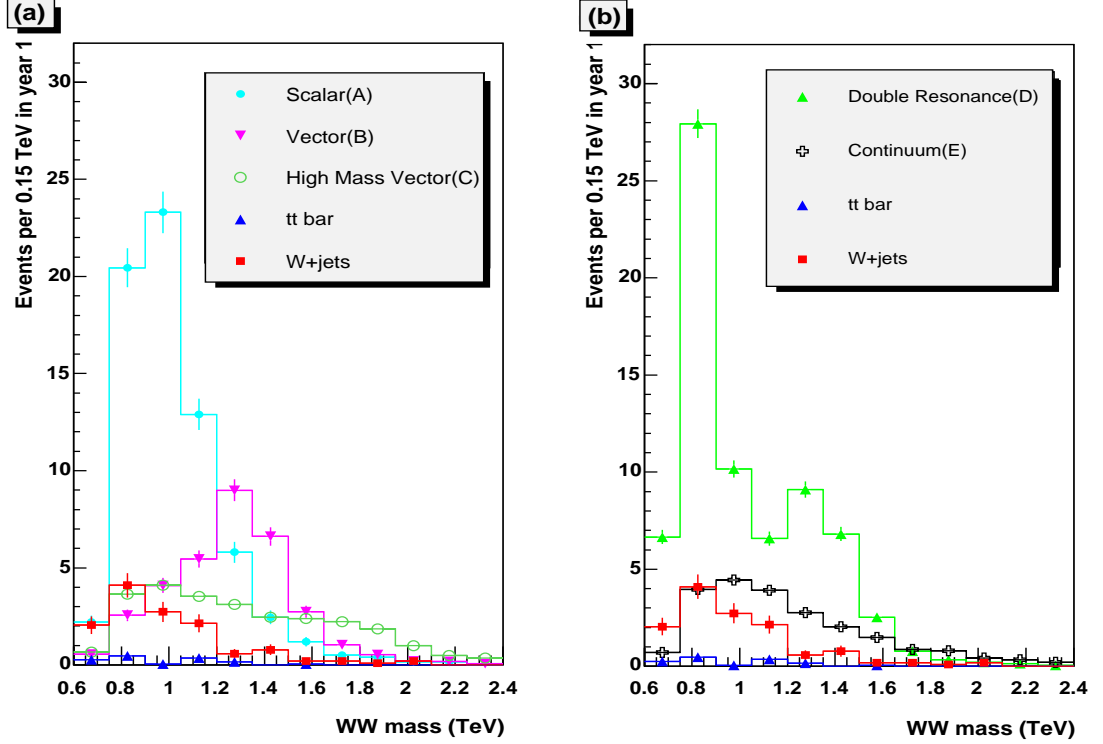


Figure 5.1: Reconstructed  $WW$  mass for signal and background separately. A: 1 TeV scalar, B: 1.4 TeV Vector, C: 1.9 TeV Vector, D: Double Resonance and E: Continuum.

Tables 5.1 and 5.2 give the effect of cuts on the signal and background samples and Table 5.3 shows how efficient the cuts are in reducing the number of events. For comparison, tables 5.4 and 5.5 show the results obtained in Reference [7]. The only relevant column is the last column with the signal to background ratio. If the results for the analysis in this thesis are compared with that obtained in Reference [7], one notices that the signal to background ratio is lower for all of the signal samples. This is due to the fact that the sample of events used in this thesis

have gone through the detector simulation and are therefore smeared, whereas the events in [7] are considered at the generator level.

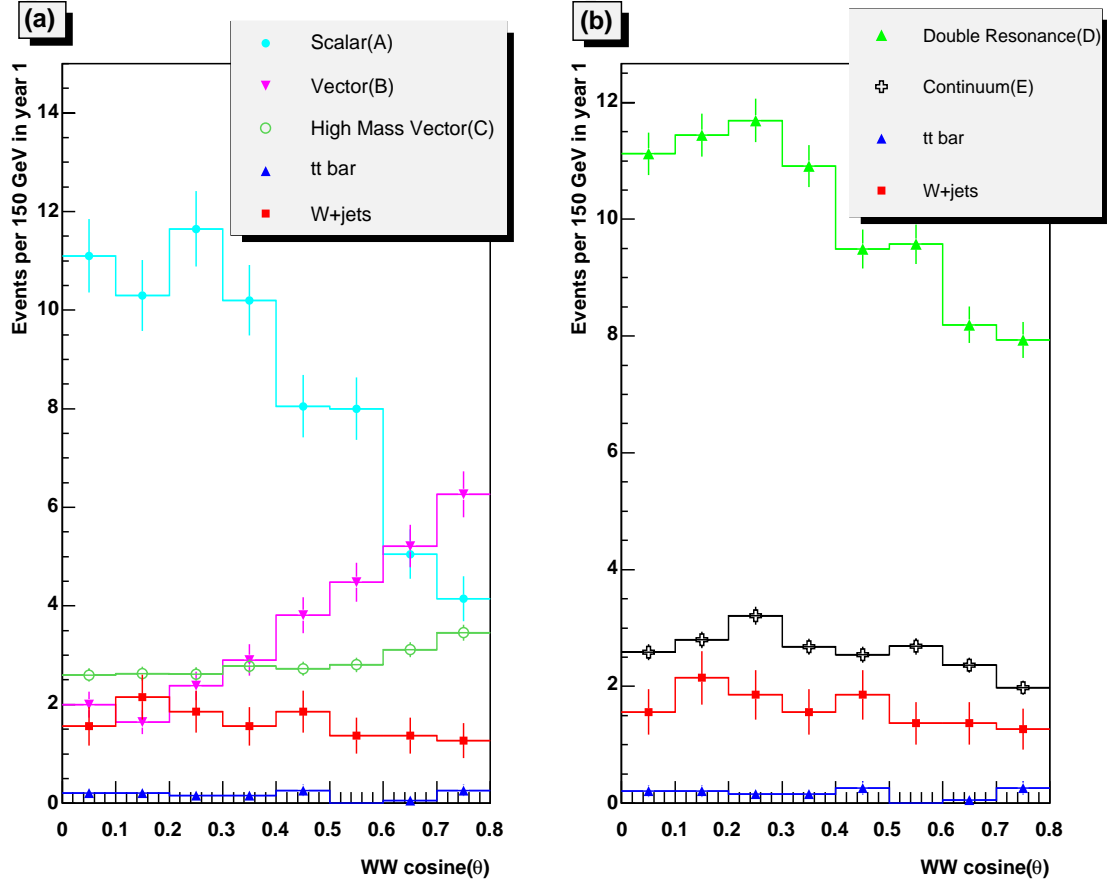


Figure 5.2:  $|\cos\theta|$  for signal and background separately. A: 1 TeV scalar, B: 1.4 TeV Vector, C: 1.9 TeV Vector, D: Double Resonance and E: Continuum.

Comparing the final signal to background ratio for the scalar 1 TeV scenario (sample A) of this analysis with that obtained in [6], the value obtained is 4.2 as opposed to  $\sim 3.0$  in [6]. The signal to background ratio obtained here is a significant improvement on the results in Reference [6], which used the cone algorithm. (Unfortunately it was not possible to show the complete results for [6] in detail

because no table with the detailed cuts and number of events left after the cuts was available in [6].) The analysis is repeated by using the cone algorithm for jet reconstruction in order to see how comparable the results in this thesis are with that in [6].



Table 5.1: Effect of leptonic and hadronic cuts on the number of events for the signal and background for an integrated luminosity of  $100 \text{ fb}^{-1}$ . A: 1 TeV scalar, B: 1.4 TeV Vector, C: 1.9 TeV Vector, D: Double Resonance and E: Continuum. S/B denotes the signal to background ratio.

Cuts	Signal	$t\bar{t}$	W+jets	S/B
Generated events	A:7,500	1,558,000	2,929,000	$1.7 \times 10^{-3}$
	B:5,250			$1.2 \times 10^{-3}$
	C:4,400			$9.8 \times 10^{-4}$
	D:11,790			$2.6 \times 10^{-3}$
	E:4,400			$9.8 \times 10^{-4}$
Require leptonic and hadronic $W p_T > 320 \text{ GeV}$	A:623.4	39,041.2	257,445.3	$2.1 \times 10^{-3}$
	B:373.4			$1.3 \times 10^{-3}$
	C:305.7			$1.0 \times 10^{-3}$
	D:836.7			$2.8 \times 10^{-3}$
	E:264.2			$8.9 \times 10^{-4}$
Hadronic $W$ mass cut: $70 < M_{hW} < 90 \text{ GeV}$ and $\eta_{hW} < 4$	A:288.1	2,716.1	37,419.4	$7.2 \times 10^{-3}$
	B:147.8			$3.7 \times 10^{-3}$
	C:118.8			$3.0 \times 10^{-3}$
	D:343.4			$8.6 \times 10^{-3}$
	E:99.7			$2.5 \times 10^{-3}$
$y_{cut}$	A:198.6	1,380.7	4,943.8	$3.1 \times 10^{-2}$
	B:101.6			$1.6 \times 10^{-2}$
	C:80.5			$1.3 \times 10^{-2}$
	D:238.0			$3.8 \times 10^{-3}$
	E:67.7			$1.1 \times 10^{-2}$

**Table 5.2:** Effect of environment cuts on the number of events for the signal and background for an integrated luminosity of  $100 \text{ fb}^{-1}$ . A: 1 TeV scalar, B: 1.4 TeV Vector, C: 1.9 TeV Vector, D: Double Resonance and E: Continuum. S/B denotes the signal to background ratio.

Cuts	Signal	$t\bar{t}$	W+jets	S/B
Top cuts	A:178.6	233.2	3,325.0	$5.0 \times 10^{-2}$
	B:90.0			$2.6 \times 10^{-2}$
	C:71.7			$2.0 \times 10^{-2}$
	D:209.0			$5.9 \times 10^{-2}$
	E:60.9			$1.7 \times 10^{-3}$
Tag jets (reject $E_{jet} < 300$ require $2 <  \eta_{tag}  < 4.5$ )	A:63.4	3.6	23.1	2.4
	B:34.7			1.3
	C:27.6			1.0
	D:75.0			2.8
	E:23.7			0.9
Hard $p_T$ (require $WW$ +tag jets $p_T < 50 \text{ GeV}$ )	A:63.3	2.3	19.6	2.9
	B:34.7			1.6
	C:27.5			1.3
	D:74.7			3.4
	E:23.7			1.1
Minijet veto (Reject $>1$ minijet, require $WW$ +tag jets $p_T < 50 \text{ GeV}$ )	A:61.3	1.5	13.2	4.2
	B:33.2			2.3
	C:26.3			1.8
	D:71.4			4.9
	E:22.5			1.5

Table 5.3: Number of events produced for an integrated luminosity of  $100 \text{ fb}^{-1}$  and the cumulative efficiencies (in %) of various cuts for the five different signal scenarios and for the  $t\bar{t}$  and W+jets backgrounds. A: 1 TeV scalar, B: 1.4 TeV Vector, C: 1.9 TeV Vector, D: Double Resonance and E: Continuum.

	A	B	C	D	E	$t\bar{t}$	W+jets
Events produced	7,500	5,250	4,400	11,790	4,400	1,558,000	2,929,000
Leptonic cut efficiency	8.3	7.1	6.9	7.1	6.0	2.5	8.8
Hadronic cut efficiency	3.8	2.8	2.7	2.9	2.3	0.17	1.3
$y_{cut}$ efficiency	2.6	1.9	1.8	2.0	1.5	0.09	0.17
Top veto efficiency	2.4	1.7	1.6	1.8	1.4	0.015	0.11
Tag jet efficiency	0.84	0.66	0.63	0.64	0.54	$2.3 \times 10^{-4}$	$7.9 \times 10^{-4}$
Hard $p_T$ cut efficiency	0.84	0.66	0.63	0.63	0.54	$1.5 \times 10^{-4}$	$6.7 \times 10^{-4}$
Minijet veto efficiency	0.82	0.63	0.59	0.61	0.51	$9.6 \times 10^{-5}$	$4.5 \times 10^{-4}$

Table 5.4: The effect of leptonic and hadronic cuts on the signal and background samples for an integrated luminosity of  $100 \text{ fb}^{-1}$ . A: 1 TeV scalar, B: 1.4 TeV Vector, C: 1.9 TeV Vector, D: Double Resonance and E: Continuum. S/B denotes the signal to background ratio. Taken from Reference [7].

Cuts	Efficiency	Signal $\sigma$ (fb)	$t\bar{t}$ $\sigma$ (fb)	W+jets $\sigma$ (fb)	S/B
Generated events	A:100%	72	18,000	65,000	$8.7 \times 10^{-4}$
	B:100%	104			$1.3 \times 10^{-3}$
	C:100%	44			$5.3 \times 10^{-4}$
	D:100%	113			$1.4 \times 10^{-3}$
	E:100%	47			$5.0 \times 10^{-4}$
Require leptonic and hadronic $W$ $p_T > 320 \text{ GeV}$	A:11%	8.2	910	4,400	$1.5 \times 10^{-3}$
	B:11%	11			$2.1 \times 10^{-3}$
	C:10%	4.4			$8.3 \times 10^{-4}$
	D:10%	11			$2.1 \times 10^{-3}$
	E:10%	4.7			$8.8 \times 10^{-4}$
Hadronic W mass cut: $70 < M_{hW} < 90 \text{ GeV}$ and $\eta_{hW} < 4$	A:6.7%	4.8	56	700	$6.3 \times 10^{-3}$
	B:6.2%	6.4			$8.4 \times 10^{-3}$
	C:5.8%	2.6			$3.4 \times 10^{-3}$
	D:5.6%	6.3			$8.3 \times 10^{-3}$
	E:5.8%	2.7			$3.6 \times 10^{-3}$
$y_{cut}$	A:4.7%	3.4	28	78	$3.2 \times 10^{-2}$
	B:4.4%	4.5			$4.3 \times 10^{-2}$
	C:4.1%	1.8			$1.7 \times 10^{-2}$
	D:4.0%	4.5			$4.3 \times 10^{-2}$
	E:4.1%	1.9			$1.8 \times 10^{-2}$

Table 5.5: The effect of environment cuts on the signal and background samples for an integrated luminosity of  $100 \text{ fb}^{-1}$ . A: 1 TeV scalar, B: 1.4 TeV Vector, C: 1.9 TeV Vector, D: Double Resonance and E: Continuum. S/B denotes the signal to background ratio. Taken from Reference [7].

Cuts	Efficiency	Signal $\sigma$ (fb)	$t\bar{t}$ $\sigma$ (fb)	W+jets $\sigma$ (fb)	S/B
Top cuts	A:4.3%	3.1	3.2	52	$5.6 \times 10^{-2}$
	B:4.0%	4.2			$7.5 \times 10^{-2}$
	C:3.8%	1.7			$3.0 \times 10^{-2}$
	D:3.6%	4.1			$7.3 \times 10^{-2}$
	E:3.8%	1.8			$3.2 \times 10^{-2}$
Tag jets (require $E_{jet} < 300$ require $2 <  \eta_{tag}  < 4.4$ )	A:1.6%	1.1	0.030	0.38	2.7
	B:1.5%	1.6			3.8
	C:1.4%	0.63			1.5
	D:1.3%	1.5			3.6
	E:1.4%	0.67			1.6
Hard $P_T$ (Require $WW$ + tag jets $p_T < 50 \text{ GeV}$ )	A:1.5%	1.1	0.020	0.32	3.2
	B:1.5%	1.5			4.5
	C:1.4%	0.61			1.8
	D:1.3%	1.4			4.3
	E:1.4%	0.65			1.9
Minijet veto (Reject $> 1$ minijet, require $WW$ + tag jets $p_T < 50 \text{ GeV}$ )	A:1.5%	1.1	0.013	0.24	4.3
	B:1.5%	1.5			6.0
	C:1.4%	0.61			2.4
	D:1.3%	1.4			5.6
	E:1.4%	0.65			2.6

## 5.2 Comparison of Results with Cone Algorithm

Table 5.6 gives the number of events generated for the five different signal scenarios and the backgrounds used for the analysis based on the cone rather than the  $k_T$  algorithm. The mass distributions for the five different scenarios of the signal, and the background are shown in Figures 5.3(a) and (b) and the signal is distinguishable above the background in all cases.

Table 5.6: Events generated using the cone algorithm. The background is generated using the restricted kinematic range given on p.90. In order to get the real number of events for an integrated luminosity of  $100 \text{ fb}^{-1}$ , a scaling must be done as in Table 5.7.

<b>Signal</b>	<b>Events</b>
1 TeV scalar (A)	0.15 million
1 TeV vector (B)	0.6 million
1.9 TeV vector (C)	0.3 million
Scalar and vector (D)	0.6 million
Continuum (E)	0.6 million
<b>Background</b>	<b>Events</b>
$W$ +jets	30 million
$t\bar{t}$	30 million

Tables 5.7 and 5.8 give the results of applying the various cuts. The last row and last column of Table 5.8 gives the final signal to background ratio after all the cuts have been applied. The overall signal rate has increased by a factor of about two as compared to that in Table 5.2. However this is done at the expense of the background. The signal to background ratio is smaller for most scenarios in comparison with the ratio obtained using the  $k_T$  algorithm. For example the signal to background ratio for the 1 TeV scalar was found to be 2.3 as compared

to 4.2 when using the  $k_T$  algorithm for jet reconstruction. It would seem that the resolution parameter  $y_{cut}$  which has been used as part of the analysis with the  $k_T$  algorithm is very effective in reducing the background.

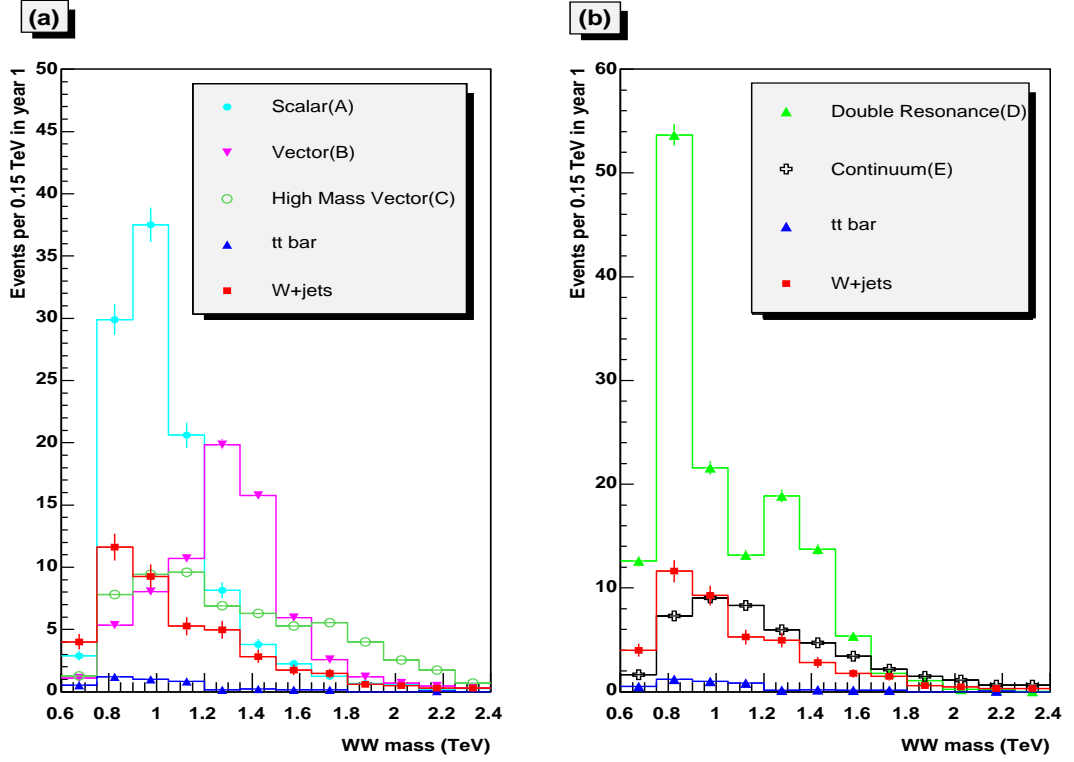


Figure 5.3: Reconstructed WW mass using the cone algorithm. A: 1 TeV scalar, B: 1.4 TeV Vector, C: 1.9 TeV Vector, D: Double Resonance and E: Continuum.

Table 5.7: Effect of leptonic and hadronic cuts on the number of events for signal and background for the cone algorithm analysis. An integrated luminosity of  $100 \text{ fb}^{-1}$  is used. A: 1 TeV scalar, B: 1.4 TeV Vector, C: 1.9 TeV Vector, D: Double Resonance and E: Continuum. S/B denotes the signal to background ratio.

Cuts	Signal	$t\bar{t}$	W+jets	S/B
Generated events	A:7,500	1,557,900	2,928,000	$1.7 \times 10^{-3}$
	B:5,250			$1.2 \times 10^{-3}$
	C:4,839			$1.1 \times 10^{-3}$
	D:11,820			$2.6 \times 10^{-3}$
	E:4,404			$9.8 \times 10^{-4}$
Require leptonic and hadronic $W_{p_T} > 320 \text{ GeV}$	A:590.6	34,185.5	244,722.3	$2.1 \times 10^{-3}$
	B:381.3			$1.4 \times 10^{-3}$
	C:332.2			$1.2 \times 10^{-3}$
	D:798.8			$2.9 \times 10^{-3}$
	E:260.1			$9.3 \times 10^{-4}$
Hadronic W mass cut: $70 < M_{hW} < 90 \text{ GeV}$ and $\eta_{hW} < 4$	A:392.6	8,385.4	22,707.4	$1.3 \times 10^{-2}$
	B:242.4			$7.8 \times 10^{-3}$
	C:201.5			$6.5 \times 10^{-3}$
	D:525.5			$1.7 \times 10^{-2}$
	E:158.7			$5.1 \times 10^{-3}$



**Table 5.8:** Effect of environment cuts on the number of events for the signal and background. An integrated luminosity of  $100 \text{ fb}^{-1}$  is used for the cone algorithm analysis. A: 1 TeV scalar, B: 1.4 TeV Vector, C: 1.9 TeV Vector, D: Double Resonance and E: Continuum. S/B denotes the signal to background ratio.

Cuts	Signal	$t\bar{t}$	W+jets	S/B
Top cuts	A:336.6	829.9	13,024.5	$2.4 \times 10^{-2}$
	B:210.1			$1.5 \times 10^{-2}$
	C:176.2			$1.3 \times 10^{-2}$
	D:444.0			$3.2 \times 10^{-2}$
	E:138.8			$1.0 \times 10^{-2}$
Tag jets (reject $E_{jet} < 300$ require $2 <  \eta_{tag}  < 4.5$ )	A:116.0	10.0	80.5	1.3
	B:77.7			0.85
	C:66.2			0.73
	D:152.7			1.7
	E:51.1			0.56
Hard $p_T$ (require $WW$ +tag jets $p_T < 50 \text{ GeV}$ )	A:115.2	6.1	63.0	1.7
	B:77.1			1.1
	C:65.8			0.95
	D:151.4			2.2
	E:50.7			0.73
Minijet veto (Reject $> 1$ minijet, require $WW$ +tag jets $p_T < 50 \text{ GeV}$ )	A:108.2	4.3	43.6	2.3
	B:72.5			1.5
	C:62.0			1.3
	D:142.4			3.0
	E:47.6			1.0

### 5.3 Effect of Smearing

Figure 5.4 shows the number of events for the reconstructed  $WW$  mass of the scalar 1 TeV sample for the case with and without smearing. Note that the jet reconstruction algorithm used was the  $k_T$  algorithm. The difference in the number of events for the unsmeared  $WW$  mass relative to the smeared  $WW$  mass is given in Figure 5.4(b). The peak around 1 TeV is due to the large number of events around this mass region.

Figure 5.5 shows the very similar result where the analysis is performed using the cone algorithm. The difference in the number of events (Figure 5.5(b)) is slightly larger for the cone data as compared to the  $k_T$  data. This is because more events survived the analysis that used the cone algorithm. It should be noted that Atlfast does the smearing at cell level based on a study using the cone algorithm. However, it should affect both the  $k_T$  and the cone analysis in a similar way as the smearing is done before any clustering.

### 5.4 Resolution as compared to the Technical Design Report [6]

In this section the resolution of the reconstructed  $W$  mass is found, where the case considered is  $W \rightarrow jj$ . The reconstruction of the two jets coming from the hadronic decay of the  $W$  boson will be vital in the search for the Higgs boson amongst other important searches and studies. Figure 5.6(a) shows the resolution obtained for the  $W$  mass, where smearing is included in the analysis, whereas Figure 5.6(b) shows the resolution for the unsmeared case. All the plots are for high luminosity with pile-up included.

The resolution obtained is  $(8.3 \pm 0.9)$  GeV, which is about 1.4 GeV worse than that obtained in [6] as shown in Figure 5.7(b). The reconstructed  $W$  mass for

this analysis is 84.2 GeV and similar values have been found for reconstructed  $W$  mass in [6]. The resolution is influenced by effects such as jet overlap, minimum-bias events, more realistic detector simulation and detector effects such as pile-up. This explains the worse resolution obtained on the reconstructed  $W$  mass.

Comparing the resolution with that found when the jet reconstruction was performed using the cone algorithm, the resolution on the  $W$  mass was found to be 7.5 GeV while the reconstructed mass is found to be 83.0 GeV.

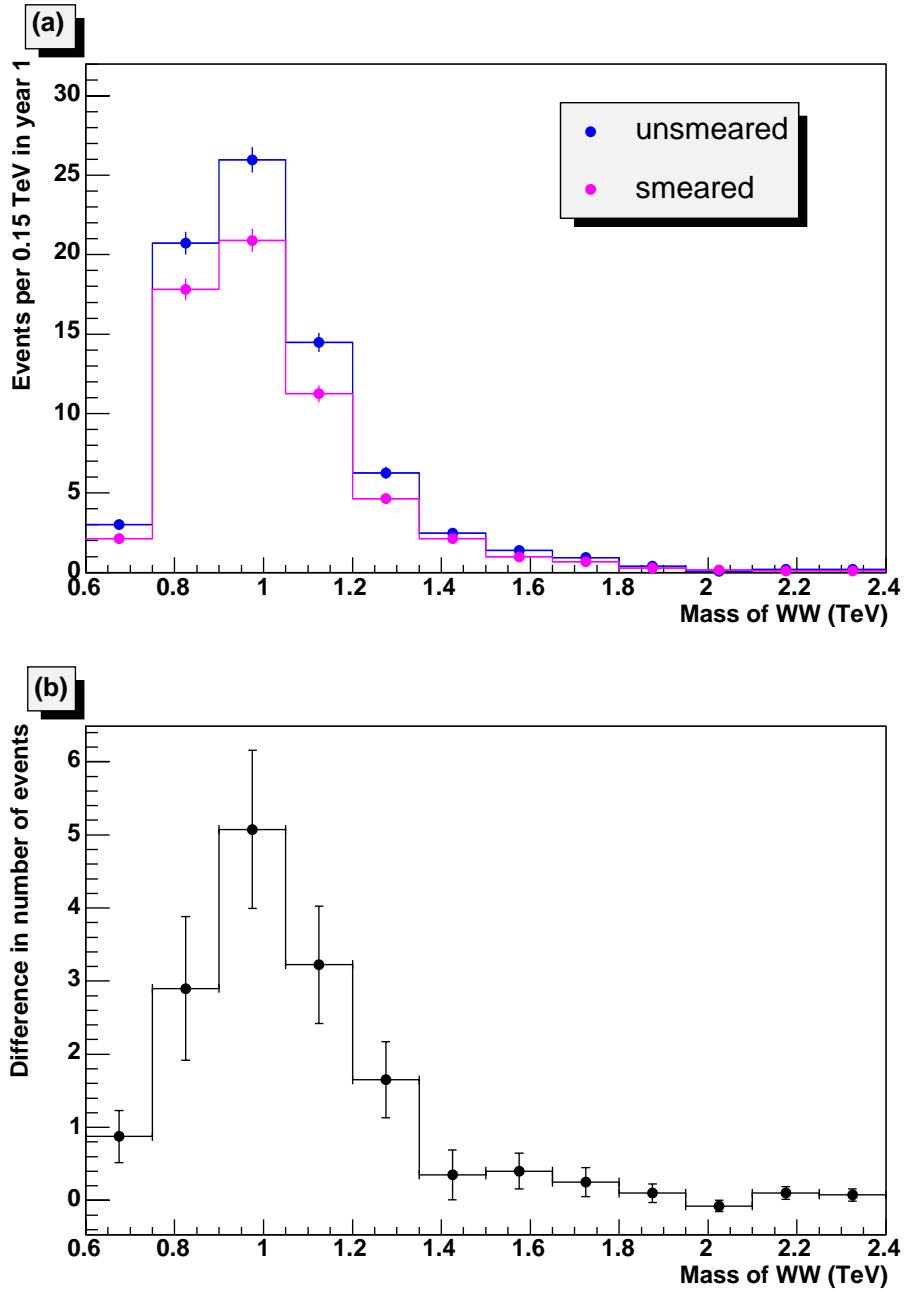


Figure 5.4: Effect of smearing using  $k_T$  algorithm for the scalar 1 TeV sample (scenario A). (a) shows the unsmeared and smeared  $WW$  mass, (b) shows the difference in the number of events between the unsmeared and smeared  $WW$  mass.

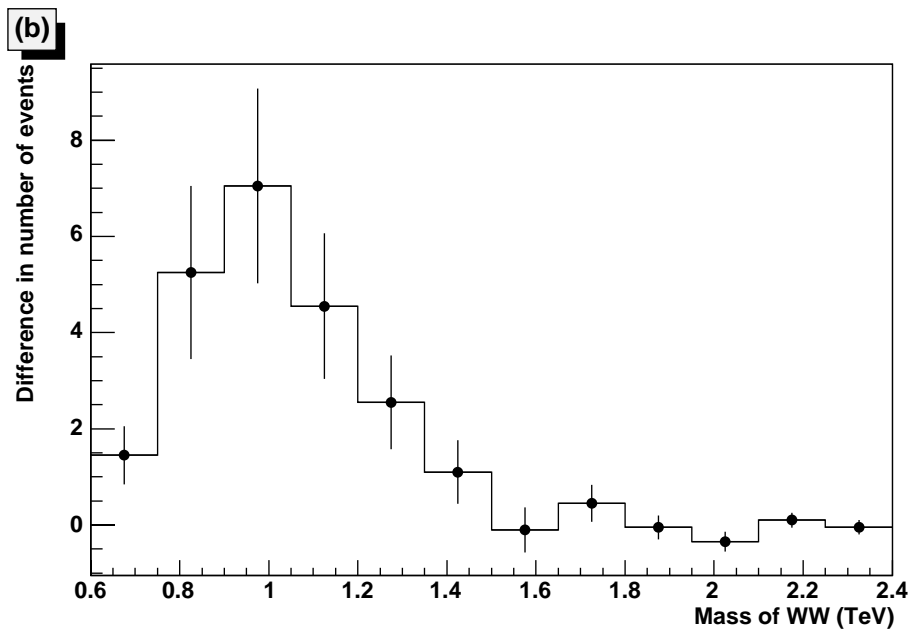
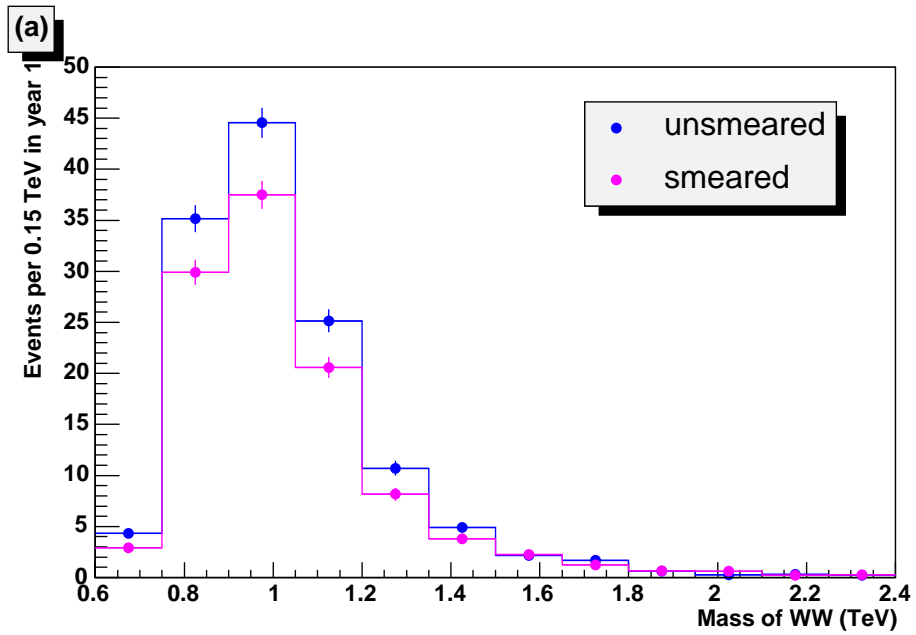


Figure 5.5: Effect of smearing using cone algorithm for the scalar 1 TeV sample (scenario A). (a) shows the unsmeared and smeared  $WW$  mass, (b) shows the difference in the number of events between the unsmeared and smeared  $WW$  mass.

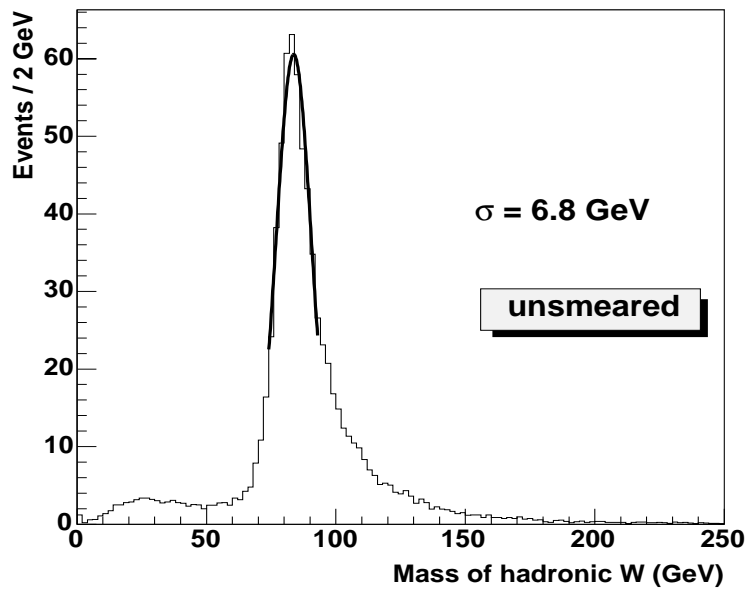
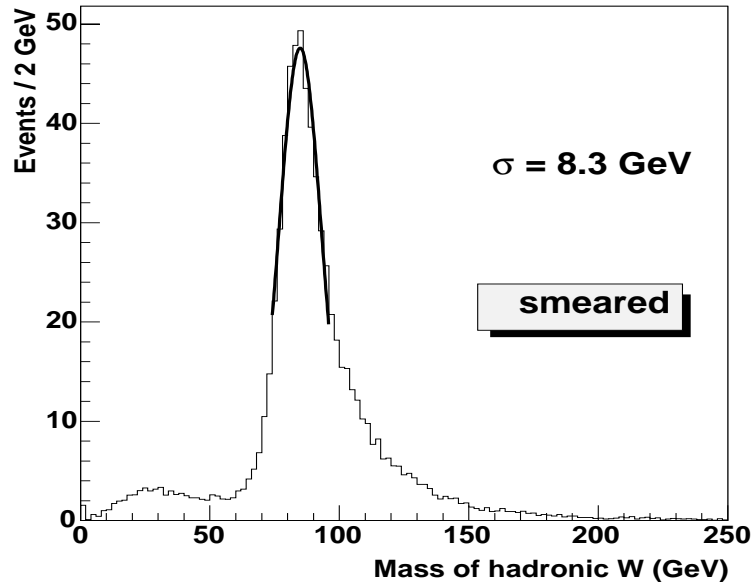


Figure 5.6: Resolution obtained using the  $k_T$  algorithm. This is the expected resolution after a year of high luminosity run at the LHC, with pile-up included. (a) shows resolution for smeared hadronic  $W$  mass, (b) shows resolution for unsmeared hadronic  $W$  mass.

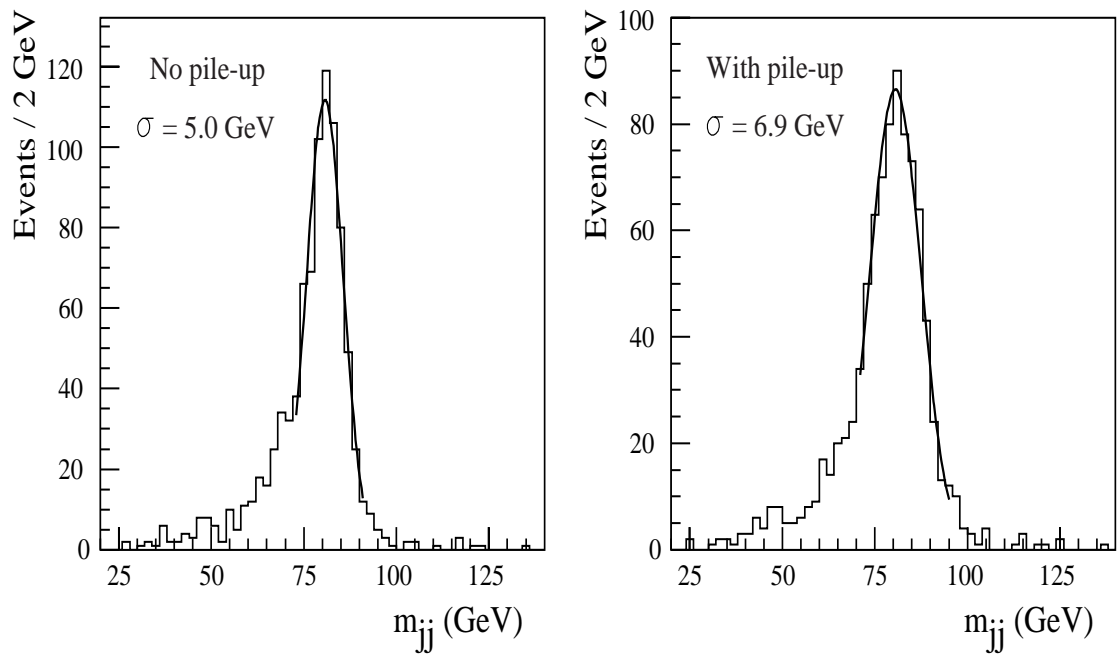


Figure 5.7: Resolution on  $W$  mass at low luminosity (left) and high luminosity with pile-up included (right) found in the Technical Design Report. The events have undergone detector simulation in both cases. Taken from [6].

## 5.5 R-parameter, Cone Radius and Cell Energy Threshold Study

As mentioned in section 4.3, a preliminary study was done to determine the value of the optimum  $k_T$   $R$ -parameter to reconstruct the jets, together with the optimum cone radius  $R$  for the cone algorithm. This was done by reconstructing the hadronic  $W$  mass and finding the best mass resolution. In order to perform this study, the continuum signal was used. 300,000 (150,000) signal samples were generated for each  $R$ -parameter (cone radius), with values ranging from 0.4 to 1.0 at cell energy thresholds from 0 to 1 GeV.

### 5.5.1 R-parameter study

Figure 5.8 shows the mass of the hadronic  $W$  for different  $R$ -parameters,  $R_{par}$ , for an energy threshold  $E_m$  of 1.0 GeV. The shape of the hadronic  $W$  mass spectrum is fairly similar for most of the  $R_{par}$ . In order to find its optimum value, a Gaussian fit was performed on the hadronic  $W$  mass for each  $R$ -parameter  $R_{par}$  at a given energy threshold  $E_m$ . Figure 5.9 shows that the resolution of the hadronic  $W$  varies slightly with  $R_{par}$  but it seems reasonable to conclude that the  $k_T$  algorithm is robust to the value of  $R_{par}$  used in this range, which is indeed interesting.

It seems that the resolution improves slightly as the cell energy threshold  $E_m$  increases as illustrated in Figure 5.9. This is also obvious from Figure 5.10, which shows the  $W$  mass for various energy thresholds for a fixed value of  $R_{par}$  (chosen as 1.0). Therefore,  $E_m = 1.0$  GeV is chosen for this study. A higher value such as 1.4 GeV could have been chosen instead but this can cause a deterioration of the final signal to background ratio after the  $WW$  mass is reconstructed. Further investigations are required but this was not possible here because of time constraints and the significant amount of signal and background events required for such an analysis.



### 5.5.2 Cone radius study

Figure 5.11(a) shows the mass of the hadronic  $W$  for cone radii  $\Delta R$  of 0.4 and 0.7 for an energy threshold  $E_m$  of 0, 0.5 and 1.0 GeV. The shape of the hadronic  $W$  mass spectrum varies substantially depending on the value of  $\Delta R$ . For example, for  $\Delta R = 0.4$  there is a peak at low energy of around 25 GeV that is as big as the peak around the hadronic  $W$ . This is not the case for the  $k_T$  algorithm as shown in Figure 5.11(b).

The next step is to find out the resolution on the hadronic  $W$  mass peak for different cone radii and energy thresholds. This is illustrated in Figure 5.12. The mass of the hadronic  $W$  has been fitted using a Gaussian as in Figure 5.6. The RMS shown in Figure 5.12 denotes the resolution obtained for the hadronic  $W$  mass.  $\Delta R = 0.7$  gives the best resolution on the hadronic  $W$  mass, irrespective of the energy threshold used. Furthermore, an energy threshold of 1.0 GeV provides the best resolution for  $\Delta R = 0.7$ .

Because the hadronic  $W$  boson is boosted, the two quark jets originating from the decay are very close and will overlap. Atlfast collects these jets into one cone and outputs the result as one jet. Therefore at a low value of  $\Delta R$ , the cone fails to include both quark jets and this gives rise to the low mass peak around 25 GeV. The first peak is less pronounced for the cone radius of 0.7.

The ratio of the number of events in the low mass peak (5-40 GeV) to that of the high mass peak (70-90 GeV) is plotted for different  $\Delta R$ . This is illustrated in Figure 5.13. Taking the case where  $E_m = 1.0$  GeV, the ratio decreases with increasing  $\Delta R$ . The ratio for  $\Delta R = 0.6$  is 0.38, that for  $\Delta R = 0.7$  is 0.25, that for  $\Delta R = 0.8$  is 0.23 and that for  $\Delta R = 0.9$  is 0.20. Therefore it is fair to assume that a stable value is reached around  $\Delta R = 0.7$ .

Another important factor in deciding whether  $\Delta R = 0.7$  is the optimum value to use is the number of events between 70 and 90 GeV. This is plotted for  $E_m = 0, 0.5$  and 1.0 GeV. For  $E_m = 1.0$  GeV, there is a maximum for a cone radius of

0.7 as shown in Figure 5.14, though this value varies depending on the energy threshold used. Hence 0.7 is chosen as the best value of  $\Delta R$  and 1.0 GeV as the energy threshold in this analysis.

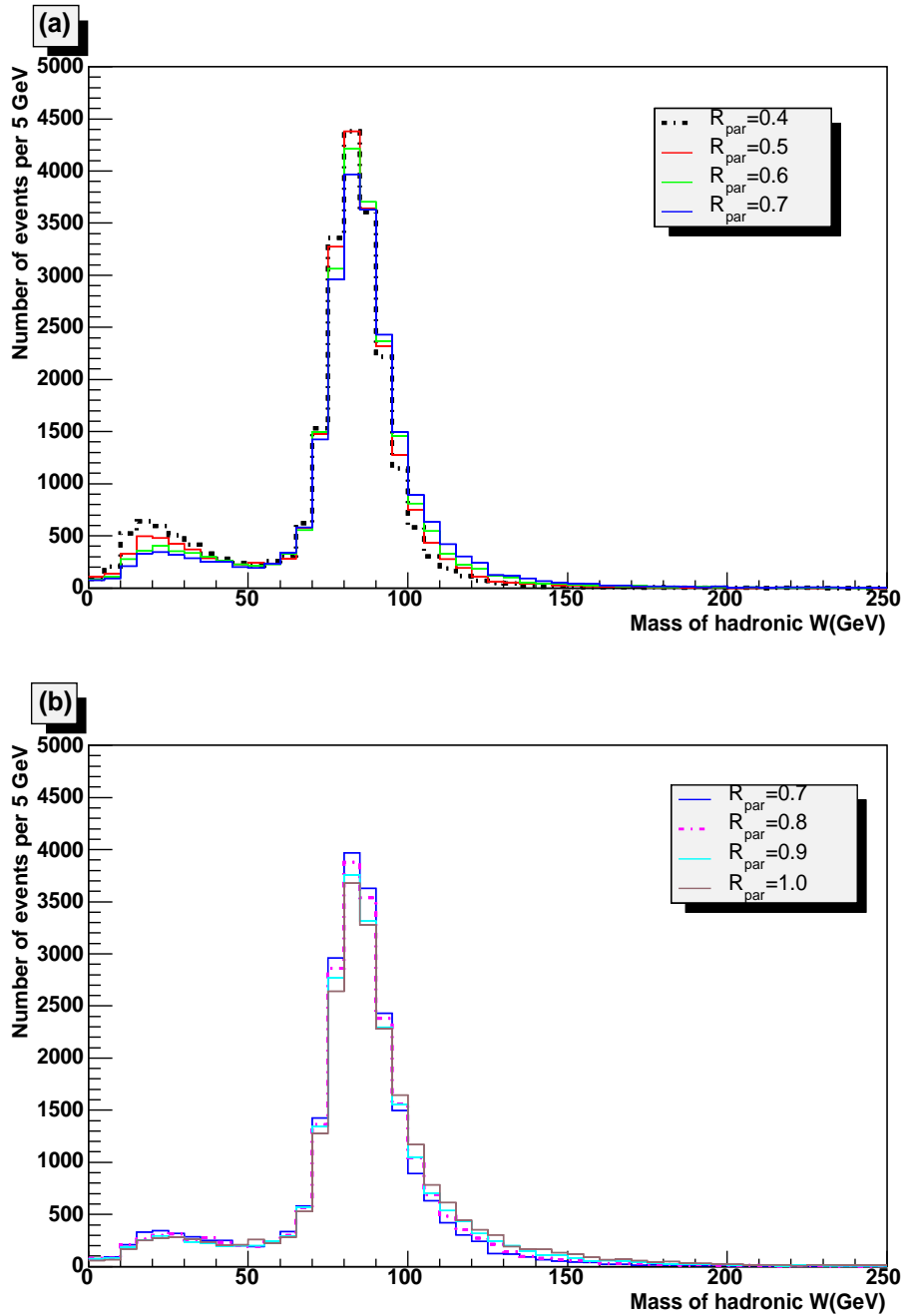


Figure 5.8: Reconstructed hadronic  $W$  mass for different  $R_{par}$  using  $k_T$  algorithm and an energy threshold  $E_m = 1.0$  GeV. Each continuum sample (scenario E) for the different  $R_{par}$  contains 300,000 events. (a) shows  $R_{par}$  0.4 to 0.7 while (b) shows  $R_{par}$  0.7 to 1.0.

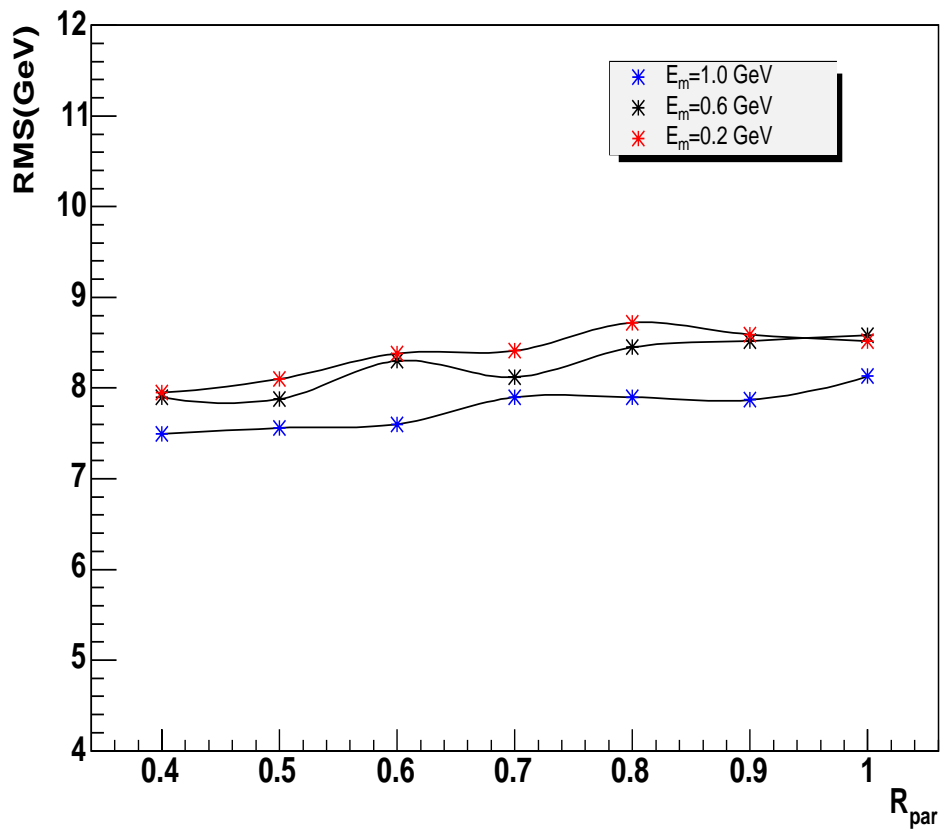


Figure 5.9:  $R_{par}$  with varying  $E_m$  using  $k_T$  algorithm for continuum sample (scenario E). A sample of 300,000 events are generated for each  $(R_{par}, E_m)$ .

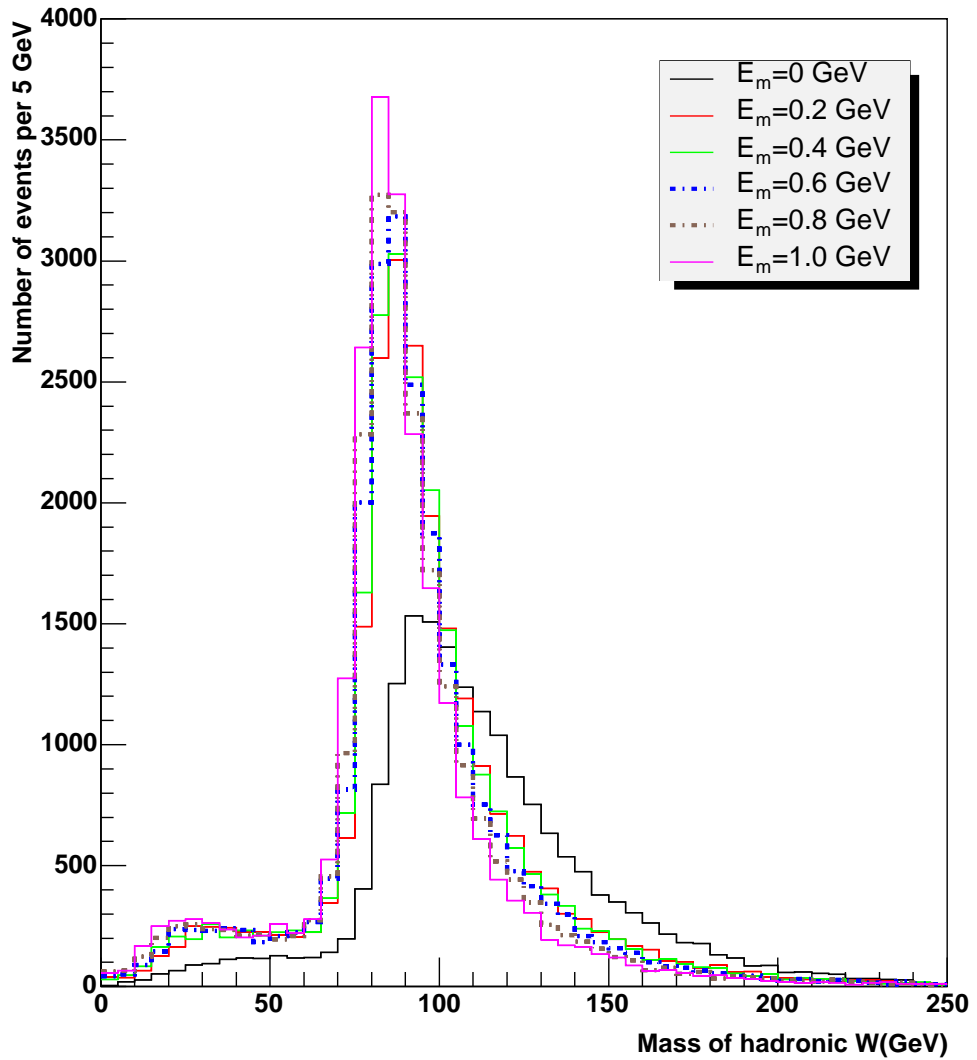


Figure 5.10:  $W$  mass for a fixed  $R_{par}$  of 1.0 and varying energy thresholds  $E_m$  using the  $k_T$  algorithm. A sample of 300,000 events are generated for each  $E_m$  and the continuum sample (scenario E) is used for this plot.

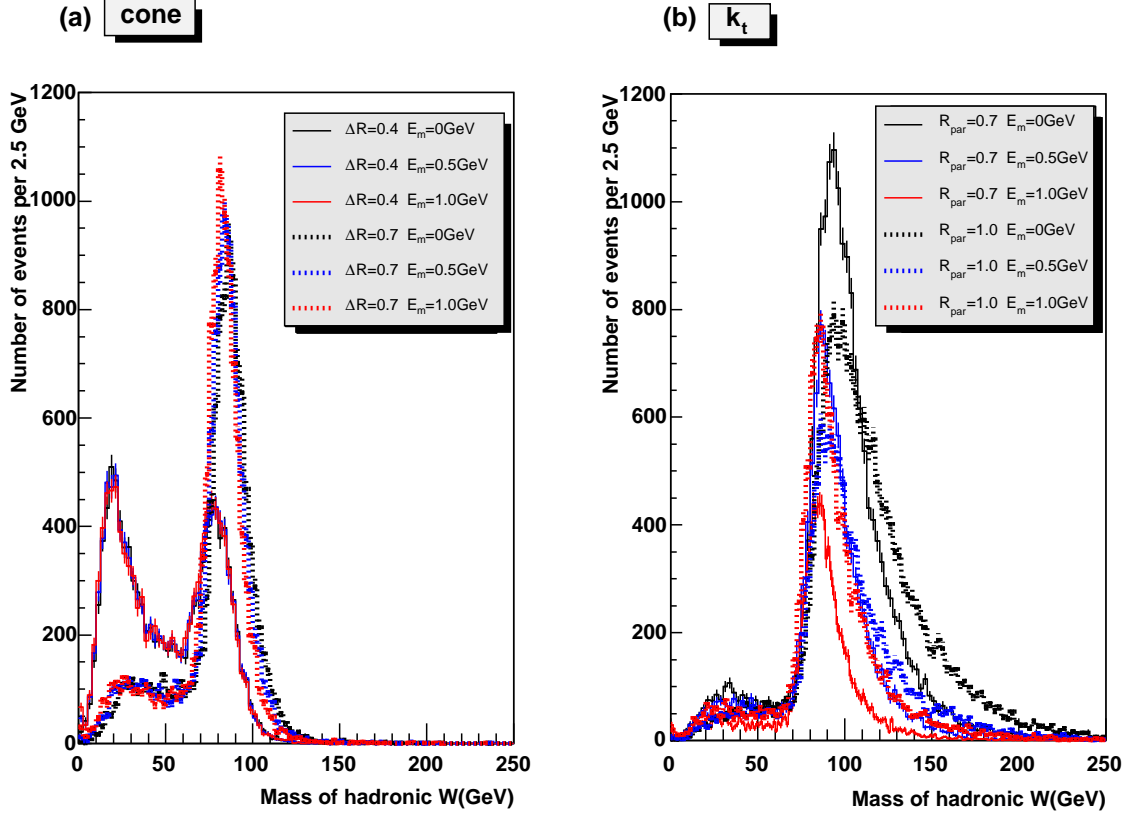


Figure 5.11: Reconstructed hadronic  $W$  mass for various energy thresholds  $E_m$ . Continuum sample (scenario E) containing 150,000 events are used for various  $E_m$  and  $R_{par}$  or  $\Delta R$ . (a) shows the hadronic  $W$  mass for a cone radius of 0.4 and 0.7, (b) shows the hadronic  $W$  mass for the  $k_T$   $R_{par}$  of 0.7 and 1.0.

### 5.5.3 Note on $k_T$ $R_{par}$

For the  $k_T$  algorithm, no clear conclusion was reached as to what value of  $R_{par}$  should be used. Hence 1.0 was used in this analysis as this value of  $R_{par}$  corresponds to the cone radius of 0.7 [48], which was found to be the optimum value for the cone method for jet reconstruction.

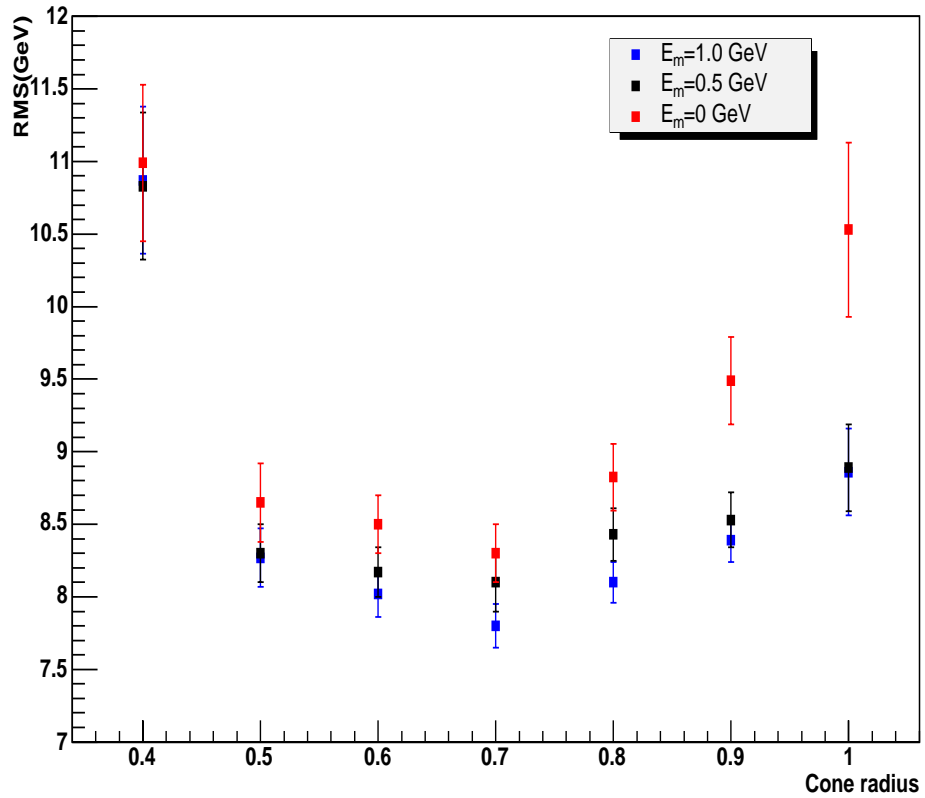


Figure 5.12: Variation of root mean square value of the hadronic  $W$  mass peak with cone radius for different energy thresholds. The peak was fitted using a Gaussian. Continuum sample (scenario E) containing 150,000 events are used for each  $(E_m, \text{cone radius } \Delta R)$ .

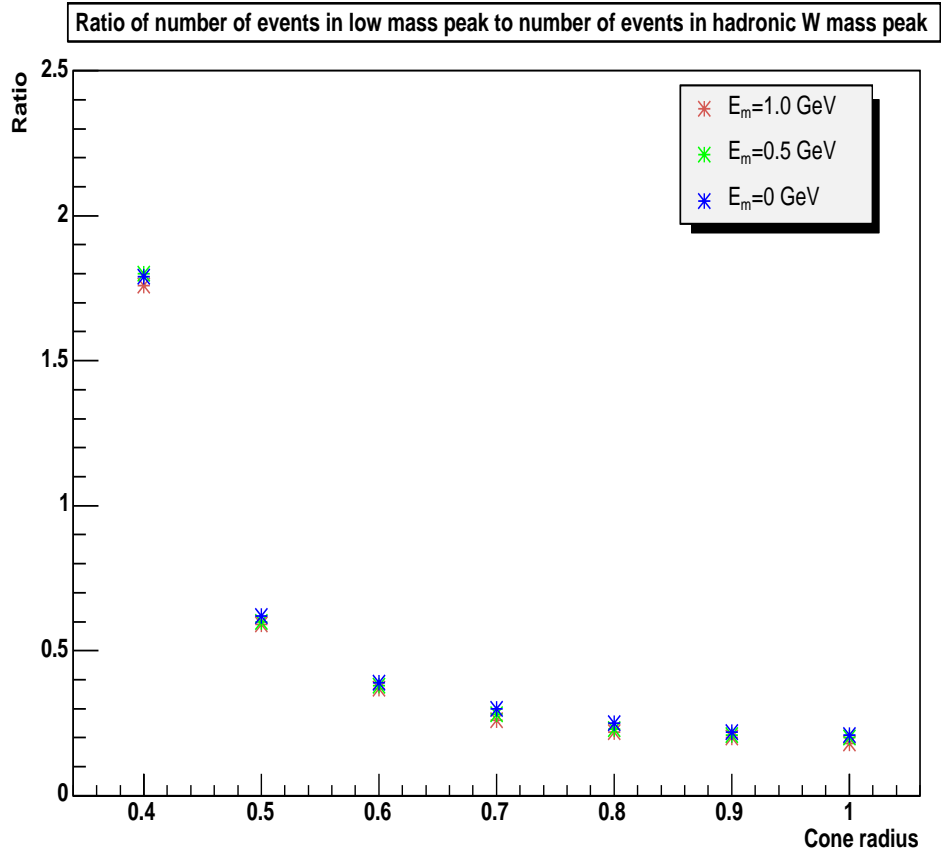


Figure 5.13: Ratio of number of events for low mass peak (5-40 GeV) to that of high mass peak taken between 70 and 90 GeV. Continuum sample (scenario E) containing 150,000 events are used for each  $(E_m, \text{cone radius } \Delta R)$



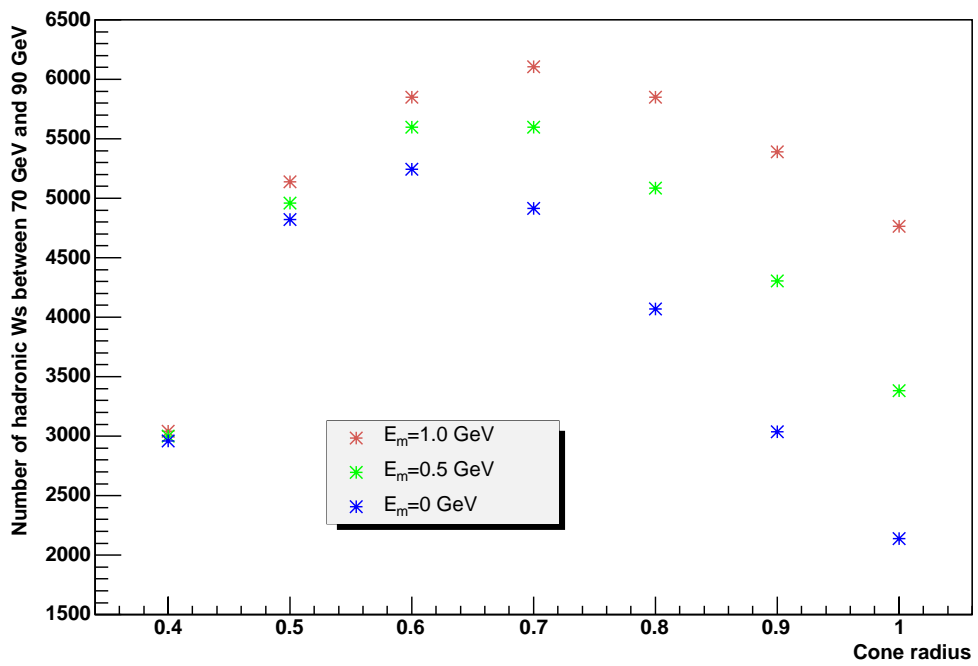


Figure 5.14: Number of hadronic  $W$  events between 70 and 90 GeV. Each continuum sample (scenario E) with various cone radii contained 150,000 events.

# Chapter 6

## Summary and Future Work

A study of  $WW$  scattering at the LHC was performed to identify any new potential physics around the TeV region which would be required to avoid violating unitarity. It was assumed that no new physics would be discovered before the start of the LHC. Semileptonic decays of the  $W$ s were considered and five different scenarios for the signal resulting from unitarisation were investigated. These five different scenarios represent the five possible types of physics one may expect at the LHC. The main backgrounds come from  $W + \text{jet}$  and  $t\bar{t}$  events.

Samples of both signal and background were generated using Atfast, where the jets were reconstructed using the  $k_T$  algorithm. A similar analysis was performed using the cone algorithm for comparison. Various cuts, such as minijet veto and hard  $p_T$ , were applied, and the invariant mass of the  $WW$  system reconstructed for the signal and background separately. The results obtained in this thesis compare well with previous studies [7] in the semileptonic channel. Most of the signal to background ratios exceeded 1.0. The expected  $WW$  mass distributions for one year of high luminosity at the LHC were found and the inputted resonances were observed.

Furthermore, the effects of both the cone radius of the cone algorithm and the R-parameter of the  $k_T$  analysis on the width of the hadronic  $W$  mass spec-

trum were investigated. A value of 0.7 for the cone radius was found to be the optimum, while the corresponding R-parameter of 1.0 was used.

Energy thresholds were also investigated to find their effect on the  $W$  mass resolution and it is obvious that as the cell energy threshold increases, the resolution of the  $W$  mass improves. An energy threshold value of 1.0 GeV was chosen for this analysis but it may be possible that higher values can give a better signal to background ratio. Further investigations are required.

In summary, this analysis has shown that ATLAS should be able to detect scalar and vector resonances of up to 1.4 TeV after a year of high luminosity leading to an integrated luminosity of  $\sim 100 \text{ fb}^{-1}$ .

# Appendix A

## Mandelstam variables

Mandelstam variables are denoted as  $s$ ,  $t$  and  $u$ . Consider two particles of momenta  $p_1$  and  $p_2$  with masses  $m_1$  and  $m_2$ . If these two particles scatter elastically to produce particles of momenta  $p_3$  and  $p_4$  with masses  $m_3$  and  $m_4$ , a set of variables which are Lorentz-invariant can be described. They are referred to as the Mandelstam variables.

Using the conservation of four-momentum

$$p_1 + p_2 - p_3 - p_4 = 0 \quad (\text{A-1})$$

one can write the Mandelstam variables as:

$$\begin{aligned} s &= (p_1 + p_2)^2 = (p_3 + p_4)^2 \\ t &= (p_1 - p_3)^2 = (p_2 - p_4)^2 \\ u &= (p_1 - p_4)^2 = (p_2 - p_3)^2 \end{aligned} \quad (\text{A-2})$$

and they satisfy

$$s + t + u = \text{constant} = m_1^2 + m_2^2 + m_3^2 + m_4^2 \quad (\text{A-3})$$

# Appendix B

## Momentum of neutrino in the z-direction

In Chapter 4, the  $z$  component of the neutrino momentum is found as follows. The total energy  $\Sigma E$  of the system and the momentum of the lepton,  $L$ , in the  $x$ ,  $y$  and  $z$  directions are known. From missing transverse energy  $E_T^{miss}$ , the  $x$  and  $y$  components of the neutrino momentum are known. The term  $K_x$ ,  $K_y$  and  $K_z$  are used to denote the  $x$ ,  $y$  and  $z$  components of the neutrino momentum respectively while  $K$  is used for its total momentum. The energy of the lepton is denoted as  $E_l$  and that of the neutrino  $E_\nu$ . The mass of the lepton is  $M_l$  and that of the neutrino is  $M_\nu$ . Since these are so small compared to the mass of the  $W$  boson, they are assumed to be zero.

As mentioned earlier in section 4.5, one of the  $W$ s from the  $WW$  scattering process is a leptonic decay:  $W \rightarrow l\nu$ . The total invariant mass of the lepton and neutrino is equal to the mass of the leptonic  $W$ , which is known because it was fed in as 80.1 GeV in the analysis. Therefore one can write:

$$(\Sigma E)^2 - (\Sigma \mathbf{P})^2 = M_W^2 \quad (\text{B-1})$$

$$(E_l + E_\nu)^2 - (\mathbf{L} + \mathbf{K})^2 = M_W^2 \quad (\text{B-2})$$

Expanding the above terms, one gets:

$$\begin{aligned} (E_l + E_\nu)^2 &= E_l^2 + E_\nu^2 + 2E_l E_\nu \\ &= (L^2 + M_l^2) + (K^2 + M_\nu^2) \\ &\quad + 2(L^2 + M_l^2)^{1/2} \times (K^2 + M_\nu^2)^{1/2} \end{aligned} \quad (\text{B-3})$$

$$\begin{aligned}
&= L^2 + K_x^2 + K_y^2 \\
&\quad + K_z^2 + 2L(K_x^2 + K_y^2 + K_z^2)^{1/2}
\end{aligned} \tag{B-4}$$

$$\begin{aligned}
(\mathbf{L} + \mathbf{K})^2 &= (L_x + K_x)^2 + (L_y + K_y)^2 + (L_z + K_z)^2 \\
&= L_x^2 + K_x^2 + 2L_xK_x + L_y^2 + K_y^2 + 2L_yK_y \\
&\quad + L_z^2 + K_z^2 + 2L_zK_z
\end{aligned} \tag{B-5}$$

Using (B-4) and (B-5), the L.H.S of equation (B-2) can now be written as:

$$2L(K_x^2 + K_y^2 + K_z^2)^{1/2} - 2L_xK_x + 2L_yK_y + 2L_zK_z \tag{B-6}$$

Equation (B-2) becomes:

$$2L(K_x^2 + K_y^2 + K_z^2)^{1/2} - 2L_xK_x - 2L_yK_y - 2L_zK_z = M_W^2 \tag{B-7}$$

Expanding:

$$\begin{aligned}
2L(K_x^2 + K_y^2 + K_z^2)^{1/2} &= 2L_xK_x + 2L_yK_y + 2L_zK_z + M_W^2 \\
4L^2(K_x^2 + K_y^2 + K_z^2) &= (2L_xK_x + 2L_yK_y + 2L_zK_z + M_W^2)^2
\end{aligned} \tag{B-8}$$

A quadratic equation for the z-component of neutrino momentum can then be obtained from the above equation.

In section 4.6.1, the higher z-component of neutrino momentum was chosen for the analysis. It does not matter which solution one uses as proven by the signal to background ratio for the scalar 1 TeV sample in Table B-1. The ratio is found to be 4.2 by using the lower z-component of  $\nu$  momentum. The number of remaining events for the signal and background can be seen in Table B-1.

**Table B-1: Number of events ( $N$ ) left after passing all cuts.**

	Signal	$t\bar{t}$	W+jets	S/B
$N$ for lower z-component of $\nu$ momentum)	61.0	1.56	13.08	4.2
$N$ for higher z-component of $\nu$ momentum	61.3	1.50	13.20	4.2

The same signal to background ratio was obtained while using the higher component of the  $\nu$   $z$ -component of momentum in section 5.1.

# Bibliography

- [1] *Elementary Particle Physics Glossary*,  
<http://hepwww.ph.qmw.ac.uk/epp/glossary.html>.
- [2] B.R. Martin and G. Shaw, *Particle Physics, Second Edition*, John Wiley and Sons, 1997.
- [3] K. Hagiwara *et al.*, *Review of Particle Physics*, Phys. Rev. **D66**, 010001 (2002).
- [4] Super-Kamiokande Collaboration, Y. Fukuda *et al.*, *Constraints on neutrino oscillation parameters from the measurement of day night solar neutrino fluxes at Super-Kamiokande*, Phys. Rev. Lett. **82** 1810 (1999).
- [5] CLRC, *Proceedings of the School for Young High Energy Physicists Held 2-14 September 2001*, Technical Report RAL-TR-2002-011, 22 May 2002.
- [6] The ATLAS Collaboration, *Technical Proposal for a General-Purpose pp Experiment at the Large Hadron Collider at CERN*, CERN/LHCC/94-43 LHCC/P2, 15 December 1994.
- [7] J.M. Butterworth, B.E. Cox and J.R. Forshaw, *WW Scattering at the LHC*, Phys. Rev. **D65** 096014 (2002) .
- [8] The ATLAS Collaboration, *ATLAS Detector and Physics Performance Technical Design Report*, CERN/LHCC/99-14, 25 May 1999.
- [9] M. Dobson, *The Second Level Trigger of the ATLAS detector at the LHC*, Royal Holloway College, September 1999.



- [10] L.R. Evans, *LHC Status and Plans*, Technical Report CERN-LHC-Project-Report-101, May 1997.
- [11] The ATLAS Collaboration, B. Zhou, *Physics Potential of ATLAS Detector with High Luminosity*, Springer-Verlag 2003.
- [12] J. Pinfold and P. Sinervo, *The TeV Frontier: Probing the Microcosm*, Physics in Canada, v.50, March/April 1994.
- [13] *Magnets for the Large Hadron Collider*,  
<http://lhc.web.cern.ch/lhc/general/magnets.htm>.
- [14] The LHC Study Group, V. Benda *et al.*, *Conceptual design of the cryogenic system for the Large Hadron Collider (LHC)*, LHC Project Report 12, 19 July 1996.
- [15] *LHC - Challenges in Accelerator Physics*,  
<http://lhc.web.cern.ch/lhc/general/acphys.htm>.
- [16] *The ATLAS Homepage*,  
<http://www.atlas.web.cern.ch>.
- [17] A.F. Fox-Murphy, *Development of a Novel Alignment System for the ATLAS Inner Detector and an Investigation of the Effect of Alignment Inaccuracies on Tracker Performance*, 1996.
- [18] The ATLAS Collaboration, *Letter of Intent by the ATLAS Collaboration for a General-Purpose pp Experiment at the LHC*, CERN/LHCC/92-4 LHCC/1 2, 1 October 1992.
- [19] The D0 Collaboration, S. Abachi *et al.*, *Direct Measurement of the Top Quark Mass*, Phys. Rev. Lett. **79** 1197, 1997.
- [20] The D0 Collaboration, S. Abachi *et al.*, *Measurement of the Top Quark Pair Production Cross Section in  $p\bar{p}$  Collisions*, Phys. Rev. Lett. **79** 1203, 1997.

- [21] M. Beneke, I. Efthymiopouls, *et.al*, *Top Quark Physics*, 1999 CERN Workshop on SM physics (and more) at the LHC.
- [22] The ATLAS Pixel Detector Community, *Atlas Pixel Detector Technical Design Report*, Technical Report CERN-LHCC 98-13, 1998.
- [23] The ATLAS Muon Collaboration, *Atlas Muon Spectrometer Technical Design Report*, Technical Report CERN-LHCC 97-22, June 1997.
- [24] *Configuration of the ATLAS trigger system*,  
<http://www.slac.stanford.edu/econf/C0303241/proc/pres/502.PDF>.
- [25] T. Sjostrand *et al.*, *High-Energy-Physics Event Generation with PYTHIA 6.1*, **hep-ph/0010017**, October 2000.
- [26] *ATLAS Offline Computing*,  
<http://atlas.web.cern.ch/GROUPS/SOFTWARE/OO/architecture>.
- [27] *Athena User Guide*, Version/Issue **1.3.0**, February 2001.
- [28] *Athena Developer guide*, Version/Issue **2.0.0**, August 2001.
- [29] M.D. Bonmati, *Discovery potential and mass measurement of MSSM charged Higgs produced in top decays with the ATLAS detector*, Universitat Autònoma de Barcelona, June 2003.
- [30] R.Brun *et al.*, *GEANT3*, CERN/DD/EE/84-1, 1996.
- [31] D. Cavalli and S. Resconi, ATLAS Internal Note **PHYS-No-100**, 1996.
- [32] E. Richter-Was *et al.*, *ATLFAST 2.0 a fast simulation package for ATLAS*, ATLAS Internal Note **ATL-PHYS-98-131**, November 1998.
- [33] *Athena-Atlfast*,  
<http://www.hep.ucl.ac.uk/atlas/atlfast/AtlfastAlgs/>.

- [34] M. Bosman *et al.*, *Jet Finder Library: version 1.0*, ATL-SOFT-98-038, CERN, Sep 1998.
- [35] E. Richter-Was *et al.*, ATLAS Internal Note **PHYS-No-074**, 1996.
- [36] *KtJet - A C++ implementation of the KT clustering algorithm*, <http://jetweb.hep.ucl.ac.uk/ktjet>.
- [37] E. Richter-Was *et al.*, ATLAS Internal Note **PHYS-No-048**, 1995.
- [38] S. Catani *et al.*, *Longitudinally-invariant  $k_T$ -Clustering Algorithms for Hadron-Hadron Collisions*, Nucl. Phys. **B406** 187, 1993.
- [39] J.M. Butterworth *et al.*, *KtJet: A C++ implementation of the Kt clustering algorithm*, Comput. Phys. Comm. vol. **153/1** 85-96, 2003.
- [40] LEP Electroweak Working Group, CERN-EP/2001-021, 2001.
- [41] M.E. Peskin and J.D. Wells, Phys. Rev. **D64** 115002, 2001.
- [42] C.F. Kolda and H. Murayama, *The Higgs Mass and New Physics Scales in the Minimal Standard Model*, hep-ph/0003170, March 2000.
- [43] A. Dobado *et al.*, *LHC sensitivity to the Resonance Spectrum of a Minimal Strongly Interacting Electroweak Symmetry Breaking Sector*, Phys. Rev. **D62** 055011,2000.
- [44] A. Bagger *et al.*, *Precision Observables and Electroweak Theories*, Phys. Rev. Lett. **84** 1385, 2000.
- [45] M. Golden *et al.*, *Strongly Interacting Electroweak Sector: Model Independent Approaches*, hep-ph/9511206, October 1995.
- [46] A.S. Belyaev *et al.*, *Strongly Interacting Vector Bosons at the LHC: Quartic Anomalous Couplings*, Phys. Rev. **D59** 015022,1999.

- [47] S. Zmushko *et al.*, *Study of  $H \rightarrow WW \rightarrow l\nu jj$  and  $H \rightarrow ZZ \rightarrow lljj$  decays for  $M_H = 1$  TeV*, ATLAS Internal Note, **PHYS-No-008**, November 1992.
- [48] M. Vaupel, *Jet Algorithms for Top Analysis*,  
<http://opal.physik.uni-bonn.de/klute/talks/d0ger/mv00.pdf>.